12-2012

Charge, Bonding, and Magneto-Elastic Coupling in Nanomaterials

Qi Sun
qsun@utk.edu

To the Graduate Council:

I am submitting herewith a dissertation written by Qi Sun entitled "Charge, Bonding, and Magneto-Elastic Coupling in Nanomaterials." I have examined the final electronic copy of this dissertation for form and content and recommend that it be accepted in partial fulfillment of the requirements for the degree of Doctor of Philosophy, with a major in Chemistry.

Janice L. Musfeldt, Major Professor

We have read this dissertation and recommend its acceptance:

Robert Harrison, Ziling Xue, Hanno Weitering

Accepted for the Council:

Carolyn R. Hodges

Vice Provost and Dean of the Graduate School

(Original signatures are on file with official student records.)

Charge, Bonding, and Magneto-Elastic Coupling in Nanomaterials

A Dissertation

Presented for the

Doctor of Philosophy Degree

The University of Tennessee, Knoxville

Qi Sun

December 2012

Acknowledgments

I would like to thank my advisor, Professor Janice L. Musfeldt, for her valuable guidance and advice, patience, encouragement, and support through my graduate studies at the University of Tennessee. Thank you for the time that you have given and for being an ideal professional and scholarly role model.

I also thank Professors Robert J. Harrison, Ziling (Ben) Xue , and Hanno H. Weitering for serving on my committee and reviewing my work.

I would like to express my acknowledgment to everybody in our research group during the past five years: Jinbo Cao, Luciana Vergara, Xiaoshan Xu, Tatiana Brinzari, Ozge Gunaydin-Sen, Peng Chen, Brain S. Holinsworth, Ken R. O'Neal, and Mazumdar Dipanjan for their collaboration, encouragement, discussions, and assistance. I would also like to thank Rita Rosentsveig, Reshef Tenne, Sheila N. Baker, Andrew D. Christianson, Christina S. Birkel, Ram Seshadri, Wolfgang Tremel, Mazumdar Dipanjan, Hunter Sims, William H. Butler, Arunava Gupta, Nara Lee, and Sang-Wook Cheong for excellent collaboration and hard work on many projects.

Finally, I thank God for the life He has given me, the greatest gift. I also would like to express my special thanks to my parents and sisters for their love, care, and support.

Abstract

Phonons are exquisitely sensitive to finite length scale effects in a wide variety of materials because they are intimately connected to charge, structure, and magnetism, and a quantitative analysis of their behavior can reveal microscopic aspects of chemical bonding and spin-phonon coupling. To investigate these effects, we measured infrared vibrational properties of bulk and nanoscale MoS_2 [molybdenum disulfide], MnO [manganese(II) oxide], and $CoFe_2O_4$ [cobalt iron oxide]. From an analysis of frequencies, oscillator strengths, and high-frequency dielectric constants, we extracted Born and local effective charges, and polarizability for MoS_2 and MnO. For MoS_2 nanoparticles, in the intralayer direction, Born effective charge of the nanoparticles decreases significantly compared to the layered bulk, a difference that we attribute to the structural strain and resulting change in polarizability in nanoparticles. For MnO nanoparticles, our analysis reveals that Born effective charge decreases by $\sim$20%, compared to the bulk material. Moreover, this change impacts both ionicity and polarizability. Specifically, MnO nanoparticles are $\sim$12% less ionic than the corresponding bulk. We also studied magnetoelastic coupling driven by the spin-ordered phase in MnO. Effective plasma frequency, Born and local effective charge, and force constant split through the 118 K Néel transition. The spin-lattice coupling drops from $\sim$5 N/m in the single crystal to $\sim$0.5 N/m in the nanoparticles. We attribute this result to a shorter phonon lifetime and reduced antiferromagnetic proportion. For $CoFe_2O_4$, the spectroscopic response is sensitive to the size-induced crossover

ferrimagnetic $\rightarrow$ superparamagnetic state, which occurs between 7 and 10 nm. A spin-phonon coupling analysis supports the core-shell model. Moreover, it provides an estimate of the magnetically disordered shell thickness, which increases from 0.4 nm in the 14 nm particles to 0.8 nm in the 5 nm particles, demonstrating that associated local lattice distortions take place on the length scale of the unit cell. Taken together, these findings demonstrate that the properties of nanomaterials, such as ionicity and polarizability, are quite different than the corresponding bulk. These ideas and concepts are important for understanding finite length scale effects in nanoscale materials and may benefit on-going work on nanodevices.

Contents

List of Tables

List of Figures

Chapter 1

Introduction

This dissertation describes charge and bonding analysis in MoS_2 and MnO nanoparticles, [1–3] and magneto-elastic coupling in two model nanoscale materials, MnO and $CoFe_2O_4$, [4, 5] with a focus on how finite length scale effects change properties in comparison to the corresponding bulk compounds. The analysis concentrates on Born and local effective charges, the relation between charge, strain, and bonding, and quantitative determination of spin-phonon coupling in nanoscale materials. The overarching goal is to investigate the fundamental properties of nanomaterials.

1.1 Chemical Bonding in Molecules and Solids

Chemical bonds hold atoms together and give rise to different physical and chemical properties in materials. Freshman chemistry teaches us that there are three general types of chemical bonds: ionic, covalent, and metallic. [6] Figure 1.1 shows the calculated electron density distributions in covalent F_2 to ionic LiF molecules. In F_2 the electrons are shared equally between atoms, and the covalent bond is nonpolar. If the electronegativities of the bonded atoms are not equal, the bond is polar because the sharing of electrons between atoms is unequal. In the HF molecule, the fluorine

center has a greater electronegativity than the hydrogen center, thus it is a polar molecule which has partial positive and negative charges. When the electronegativity difference between atoms is very large, the resultant bond is usually described as ionic (Fig. 1.1). [6] But even in highly ionic LiF, there is still some electron density on Li atom. That means LiF is not a fully ionic molecule, despite what we teach in freshman chemistry.

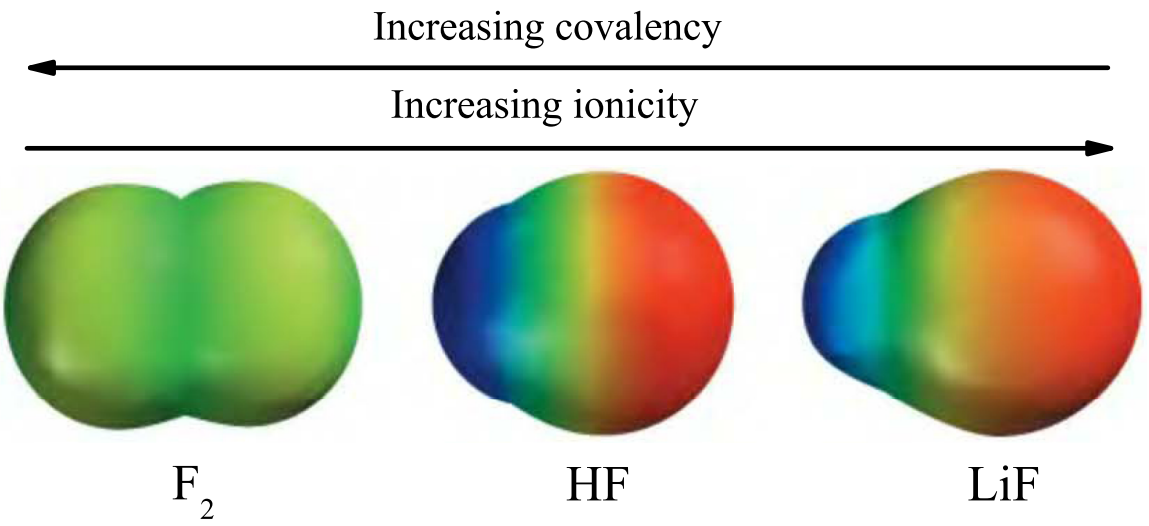

Figure 1.1: Calculated electron density distribution on the surface of the F_2, HF, and LiF molecules. The regions of relatively low electron density appear blue, those of relatively high electron density appear red, and regions that close to electrically neutral appear green. [6]

In nature, there are three classical states of matter: gas, liquid, and solid. While a gas is made up of individual atoms or molecules in which the chemical bonds behave as mentioned above, a solid has a fixed shape in which the atoms are tightly bound

to each other, either in a regular geometric lattice or an amorphous state. There are four typical solids: molecular, covalent, metal, and ionic solid. We can find all kinds of chemical bonds in solids, but atoms in them form a three dimensional network which have different physical and chemical properties compared to molecules. The chemical bonding is also described differently.

In an ideal ionic solid, the ionic bonds result from the electrostatic interaction of positive and negative ions. The binding energy of ideal ionic crystals can be expressed as Madelung energy, $U_{i,j}$, where, $U_{i,j}$ is the interaction energy between ions i and j. Madelung energy includes the sum of a central field repulsive potential, $\lambda exp(-r_{ij}/\rho)$ and a Coulomb potential, $\pm(Z^*)^2/r_{ij}$. Thus $U_{ij} = \lambda exp(-r_{ij}/\rho) \pm (Z^*)^2/r_{ij}$. Where Z^* is the local (or ionic) effective charges, r is the distance between positive and negative ions, λ and ρ are empirical parameters. [7] But even in a highly ionic material, most systems are far from the Madelung limit. For instance, the local effective charge is 0.8 e in NaCl. [7, 8] Real materials always include covalent interactions which refer to the forces between atoms when they share electrons. Figure 1.2 shows an example of a system that is normally considered to be highly ionic, MnO. The local effective charge is far from the ideal ionic limit because of the existence of covalent interactions. It turns out that vibrational spectroscopy is well suited to probing chemical bonding in a solid, as described below. In this work, we extend this traditional analysis to include nanomaterials.

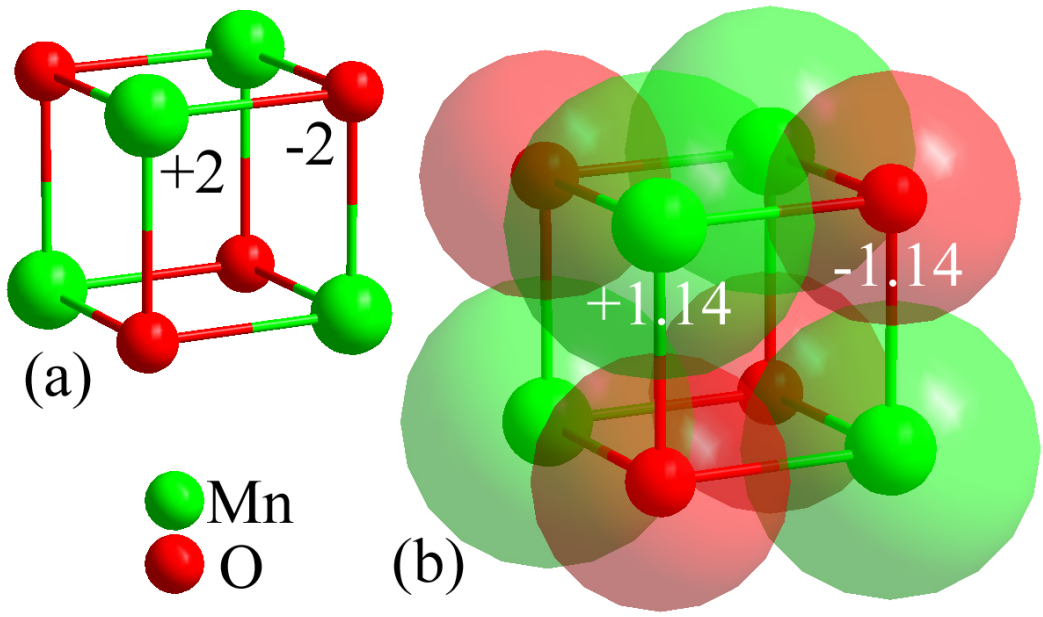

Figure 1.2: (a) Schematic view of an ideal ionic crystal of MnO made up of +2 and -2 ions. (b) Schematic view of a more realistic MnO crystal. Here, local effective charge (ionicity) is given by +1.14 and -1.14 ions. The transparent regimes schematically indicate electron clouds (total polarizability) that are shared by the involved atoms, with electron density concentrated in the regions between atomic centers. [3]

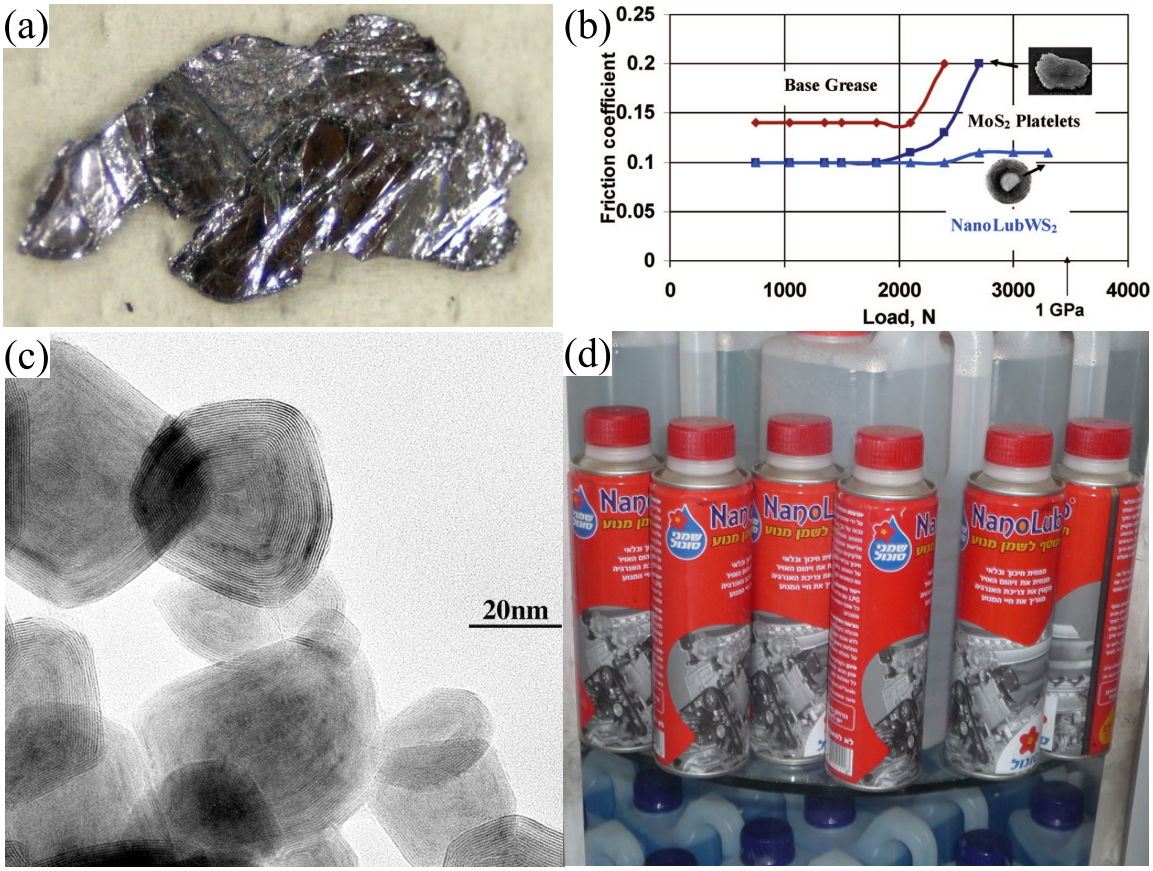

Figure 1.3: (a) Photo of 2H-MoS_2 from Wikipedia. (b) Friction coefficient as function of load. [9] (c) TEM images of IF-MoS_2 nanoparticles. [1] (d) Commercial nanolubricant. Figure courtesy of Prof. Reshef Tenne.

1.2 Using Vibrational Spectroscopy to Understand Charge and Bonding in Solids and Nanomaterials

Infrared vibrational spectroscopy is a powerful and microscopic technique for studying charge and bonding based on the analysis of optical phonons in ionic solids. This is because it is sensitive to the vibrational modes associated with dipole moment changes. [10–19] Using the relationship between the longitudinal and transverse optic phonon frequencies (often called the LO-TO splitting) and high frequency dielectric constant ($\varepsilon_1(\infty)$), it is relatively straightforward to quantify chemical bonding from optical measurements of high-quality single-crystal samples. [10–19] The Born effective charges, which describes the static and dynamic polarizations, can be estimated using the q→0 limit technique and the Lyddane-Sachs-Teller relation ($\varepsilon_1(\infty)((\omega_{LO})^2 - (\omega_{TO})^2) \sim (Z_B^*)^2$). From first principle calculations such as density functional theory, we can also quantify the chemical bonding in a solid. [19–24] In that case, theoretical calculations provide a good check of our experimental work. Figure 1.4 shows two typical examples of vibrational spectra in single crystalline MoS_2 and MnO from the literature. [13, 18] Using a Kramers-Kronig or an oscillator fit analysis of the reflectance, the authors estimated effective charge and chemical bonding.

Charge and bonding analysis was well established in many bulk materials, such as transition metal dichalcogenides and oxides. [12–19, 23–26] The physical and structural properties of MoS_2 (Fig. 1.3(a)) provide an interesting basis for studies of lattice dynamics. [12–15] In 1970's, researchers already calculated Born effective charges, [27] ($Z_B^* \approx$ 1.1 - 1.2 e (e is the electric charge) in the intralayer direction of bulk MoS_2), [13, 14] making it one of the more covalent systems of transition

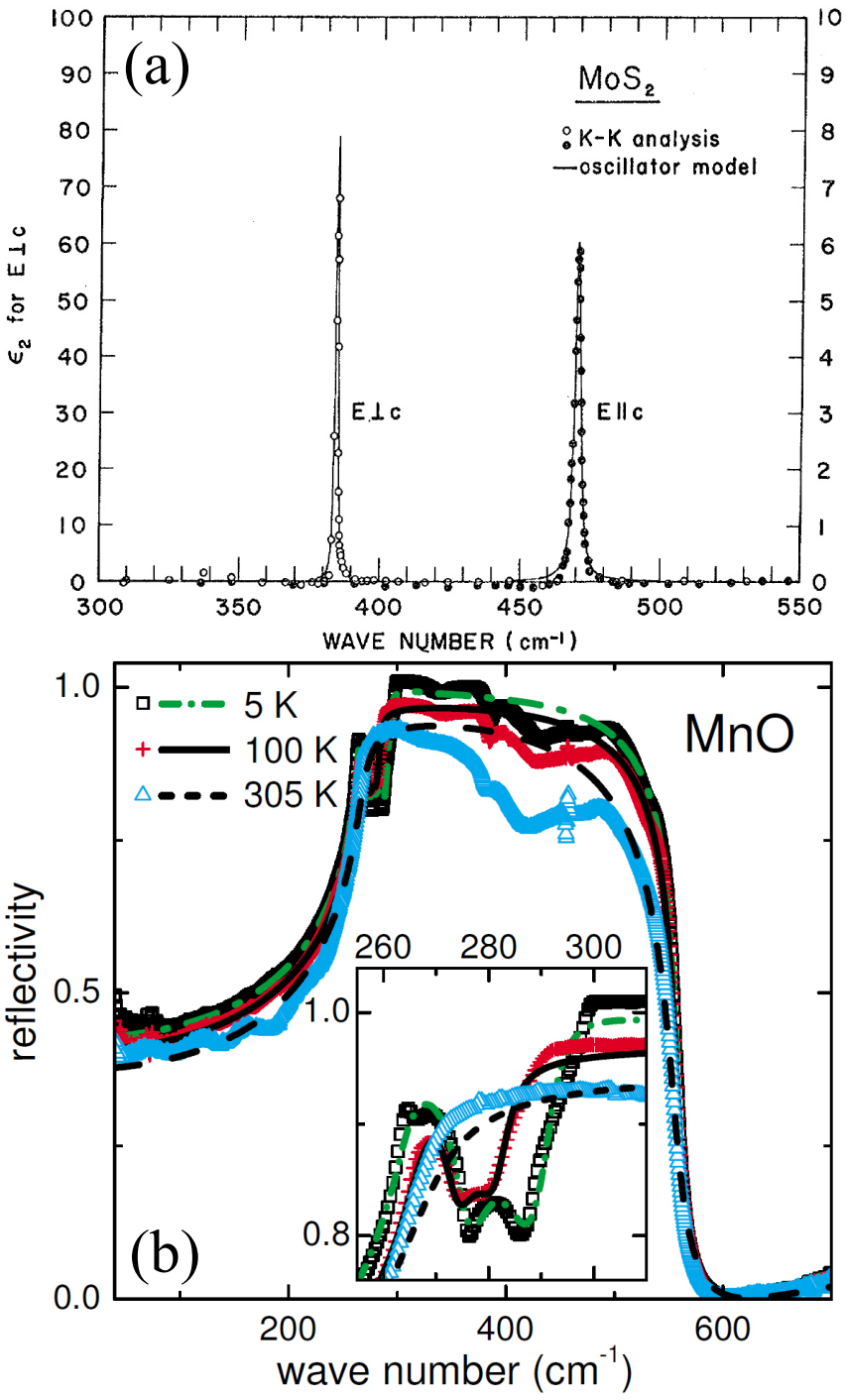

Figure 1.4: (a) Imaginary part of the dielectric function for 2H-MoS_2. The data points come from a Kramers-Kronig anaylysis of the reflectivity, and the solid curve is a damped classical oscillator fit. [13] (b) Reflectivity spectra of MnO at 5 K, 100 K, and 305 K. The lines are results of fits based on a generalized oscillator model. The inset shows the splitting of the phonon mode below T_N. [18]

metal dichalcogenides. MnO is a typical transition metal oxide which is the parent compound for many functional materials such as colossal magnetoresistant manganites. [26] Because of its simple rock salt structure and basic $3d$ electronic characterization, MnO attracted a lot of attention from the charge and bonding point of view. [16–19, 23, 24, 28] Previous infrared investigations of MnO focused on analysis of the Restrahlen band, and evaluation of Born and local effective charges ($Z_B^* = 2.2$ - 2.6 e, $Z^* = 1.08$ e for the Mn center). [16–19, 23, 24]

The discovery of nanoscale MoS_2 and MnO opened up new opportunities for the synthesis and study of new kinds of nanostructures with properties that differ significantly from the corresponding bulk materials based upon these enhanced properties. [29–48] Figure 1.3(c) and Fig. 1.5(a) display representative TEM images of IF-MoS_2 and 8 nm MnO nanoparticles. Various applications have been proposed for nanomaterials. [9, 49–55] For example, Figures 1.3(d) and (b) show an application of IF-MoS_2 as a lubricant, and the nanoscale lubricant has reduced friction coefficient at a high load. Finite length scale effects play very important roles on these applications. One challenge is understanding exactly how the microscopic aspects of charge and chemical bonding should be quantified in nanomaterials. MoS_2 and MnO attracted our attention as rich systems with which to explore this development because (i) charge and bonding analysis is well established in these systems in single crystal form, [12–19] (ii) high quality nanoscale materials are available for our research. [29–36] Our findings motivated us to develop a new model on investigating phonon confinements which offer the opportunity to probe fundamentally new aspects of structure and chemical bonding in nanomaterials.

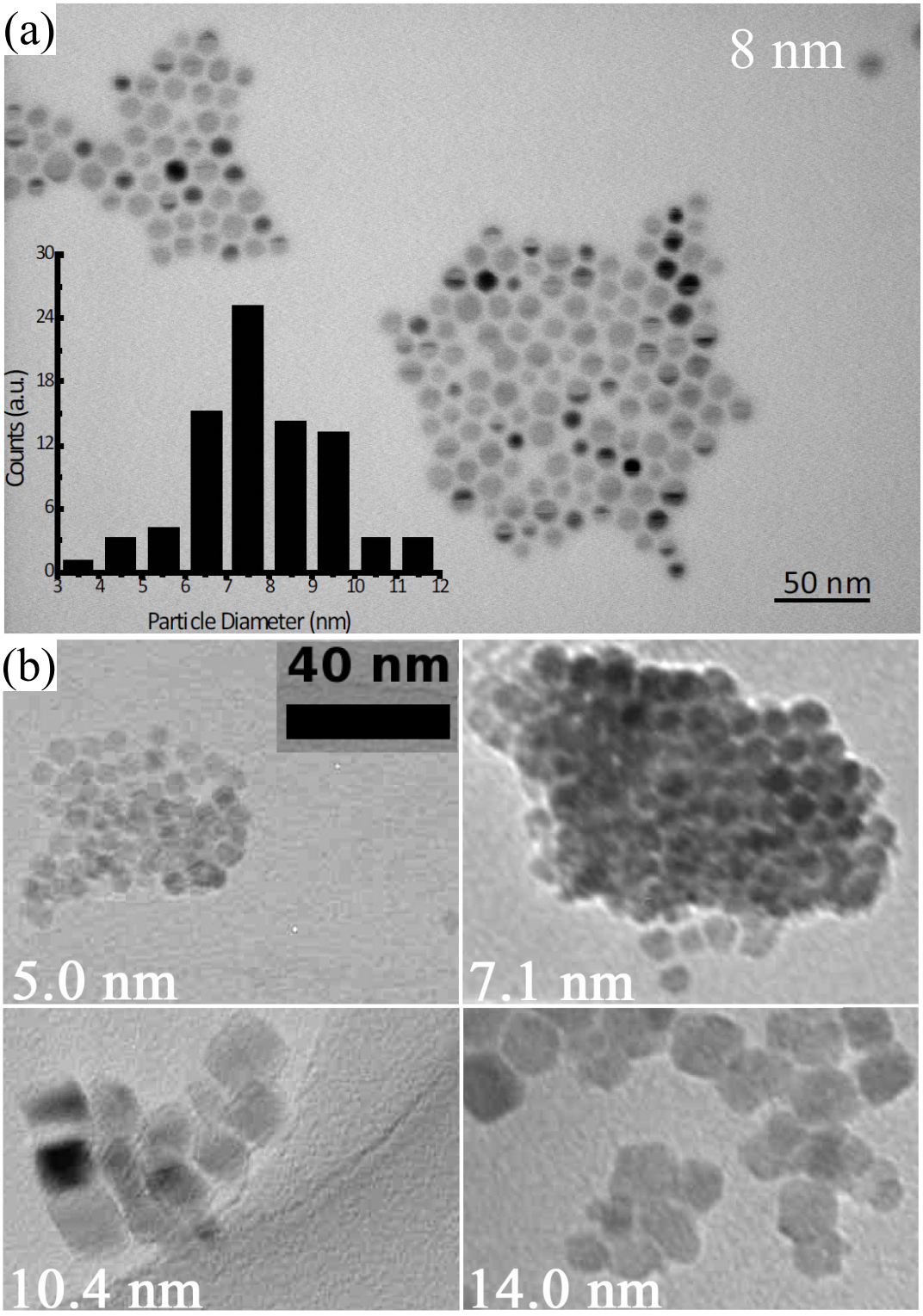

Figure 1.5: (a) TEM images of 8 nm MnO nanoparticles. [3] (b) TEM images of the four different sizes of $CoFe_2O_4$ nanoparticles. [5]

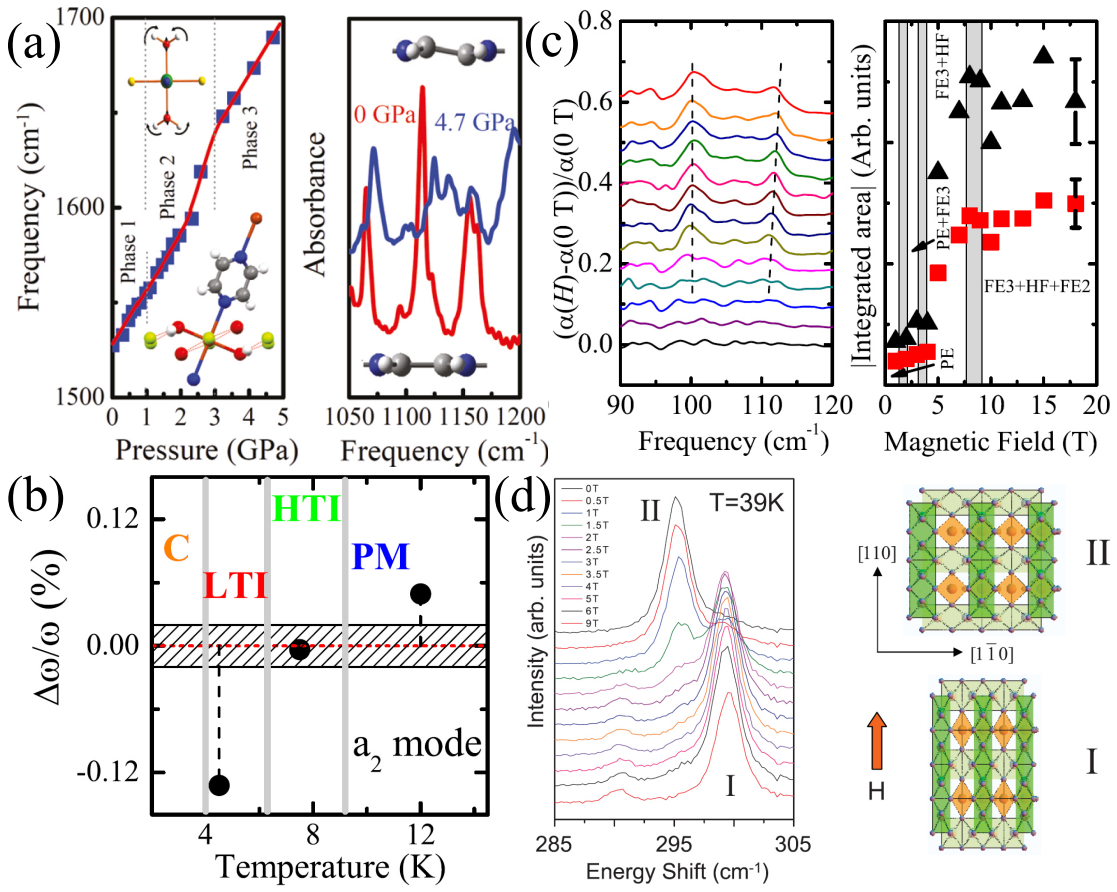

Figure 1.6: (a) Pressure-induced local structure distortions in $Cu(pyz)F_2(H_2O)_2$ which reinforce magnetic dimensionality crossover. [69] (b) Relative frequency change for a_2 mode, which indicates a temperature-induced spin-phonon coupling in $Ni_3V_2O_8$. [70] (c) Close-up view of the absorption difference spectra near 100 cm^{-1} and a magnetic-field-induced spin-phonon coupling in $DyMn_2O_5$. [71] (d) Magnetic-field-induced lattice distortion (tetragonal $\rightarrow$ monoclinic phase) in Mn_3O_4 measured by Raman scattering at T = 39 K for H ||k [110]. [72]

1.3 Spin-Phonon Coupling in Solids

In the magnetic state, the interplay between spin and lattice becomes important in materials because it gives rise to a lot of interesting mechanisms, such as the spin-Teller and the magnetoelectric effects. [26, 56–59] The major challenge on understanding spin and lattice interaction is to estimate the influence of magnetic order on phonons. [60–68] Spectroscopies are essential tools to investigate lattice vibrations. Figure 1.6 summarizes a wide variety of different spectroscopic results for several typical magnetic materials. [69–72] There are several well-known external stimuli that can drive magnetic phase transitions, including temperature, magnetic field, pressure, and electric field.

These results show a fundamental and general mechanism of spin-phonon coupling which can be understood by examining the equations of motion of the ions. When the atomic centers in a unit cell vibrate, the exchange interactions become a function of the displacement, and spin-spin interaction changes the effective phonon potential. This generic mechanism couples spin to the lattice as $\omega^2 = \omega_0^2 + \lambda\langle S_i \cdot S_j \rangle$, [67, 68, 73, 74] where ω is the perturbed mode frequency (in the presence of spin-spin interactions), ω_0 is the bare phonon frequency without spin-spin interactions, λ is the macroscopic spin-phonon coupling constant, and $\langle S_i \cdot S_j \rangle$ is the nearest-neighbor spin-spin correlation function. The core of the spin-phonon coupling analysis is to estimate the macroscopic spin-phonon coupling constant. Because $\lambda = \frac{1}{\mu} \cdot J''(u_0)$, a large coupling constant indicates a strong anharmonic effect of the magnetic exchange J as a function of displacement, u, where μ is the reduced mass. For example, $ZnCr_2O_4$ has $\lambda = 6.2$ cm^{-1}, [75] but MnF_2 has $\lambda = 0.3$ cm^{-1}. [73] The magnetic material with high symmetry usually has a large spin-phonon coupling constant. [73, 75] Within the framework of this mechanism, spin-phonon coupling analysis provides a deep understanding of spectroscopic results and brings a new opportunity

to investigate magnetic properties of materials. [60–68] It can be tailored for a wide variety of applications such as spintronics. [26, 76, 77] Because spin-phonon coupling is a relatively new topic in magnetic materials, most investigations focus on the bulk. [60–72]

1.4 Extending Spin-Phonon Coupling Models to Nanomaterials: MnO and $CoFe_2O_4$

Infrared vibrational spectroscopy plays an important role in understanding magneto-elastic coupling in a solid, which governs the properties of many complex materials including superconductors, thermoelectrics, and multiferroics. [10–12,26,56,57,78–83] Studies of the optical phonons through the phase transition of magnetic oxides, reveal local lattice distortions, elucidate coupling mechanisms, and reveal microscopic spin arrangements provide particular insight. [60–68, 70, 72, 73, 75, 84–88] A description of spin-phonon coupling in oxides has, however, been one of the major challenges of the past several decades. [18, 67, 68, 74, 75, 89] The opportunities to explore spin-phonon coupling in nanomaterials is important on understanding finite length scale effects. [31–36, 90–100]

Transition metal oxides exhibit a plethora of fascinating phase transitions and unusual magnetic properties due to the strong electron correlation and the strong interplay between charge, spin, and magnetism. [101] When the materials are in the magnetic state, the interplay between spin and lattice becomes important because the ordered spin-spin interactions change the potential energy between the ions in a solid. [26, 56–59] MnO and $CoFe_2O_4$ attracted our attention as classic magnetic oxides with well-known magnetic structures. Others have also investigated spin-phonon coupling of these systems. [18, 74, 102–104] At 118 K, MnO undergoes a transition

from a strongly correlated paramagnetic insulator (PMI) to a type-II antiferromagnet (AFMII). [74,102,105] The Néel transition is accompanied by a rhombohedral distortion (Fig. 3.4(b)), evidenced in the lattice constants by exchange striction [106] and the infrared spectrum as magnetic ordering-induced phonon splitting. [18] Below the 860 K Curie temperature (T_C), $CoFe_2O_4$ presents long range collinear ferrimagnetic order (with antiferromagnetic inter-sublattice exchange interactions). [103] The large magnetic exchanges make the magneto-elastic coupling important at room temperature. Both MnO and $CoFe_2O_4$ are available in nanoscale form, which makes our work possible. Figures 1.5(a) and (b) displays representative TEM images of MnO and $CoFe_2O_4$ nanoparticles. We investigate spin-phonon coupling in these systems because (i) coupling in a magnetic oxide is anticipated to be large [68, 75, 86] and (ii) confinement effects [31–35, 107–109] can be explored.

1.5 Science Summary

The scientific challenges addressed in this dissertation are summarized in Table 1.1. The remainder of the document is organized as follows. The second chapter discusses theoretical and experimental technique, and materials. Chapter 3 gives a literature survey of selected interesting properties of MoS_2, MnO and $CoFe_2O_4$. Chapter 4 presents the charge and bonding analysis of bulk and nanoscale MoS_2. Chapter 5 is devoted to infrared vibrational properties of bulk and nanoscale MnO, focusing on the ionicity and the spin-phonon coupling. Chapter 6 details the spin-phonon coupling analysis in $CoFe_2O_4$ nanoparticles, with the goal of understanding the superparamagnetic transition and surface spin disorder. Chapter 7 summarizes my findings.

Table 1.1: Scientific problems addressed in this dissertation

Scientific problems	Model compounds used to investigate scientific problems	Scientific findings
Charge and bonding analysis	IF-MoS_2 MnO nanoparticles. Refs. [1–3]	• Intralayer Born effective charge decreases strongly in IF-MoS_2 due to the phonon confinement. • Structure strain modifies the polarizability of IF-MoS_2 in the intralayer direction. • Born effective charge decreases 20% for 8 nm MnO nanoparticles. • Local effective charge (ionicity) decreases 12% for 8 nm MnO nanoparticles.
Spin-phonon coupling	MnO and $CoFe_2O_4$ nanoparticles. Refs. [4,5]	• Effective charges are sensitive to T_N for MnO. • Weak spin-phonon coupling constant for MnO nanoparticles compared with bulk. • Magnetic properties and spectroscopic signature of the superparamagnetic transition in $CoFe_2O_4$. • Surface spin disorder in $CoFe_2O_4$ nanoparticles. • Spin disorder take places on the length scale of the unit cell in $CoFe_2O_4$ nanoparticles.

Chapter 2

Materials and Methods

Light interacts with a solid in many different ways, such as absorption ($\alpha(\omega)$), reflectance ($R(\omega)$), transmittance ($T(\omega)$), and scattering. Infrared and optical spectroscopy analyze the reflectance or the transmittance of the sample, which can be described by the dielectric constants, as a function photon energy. The dielectric constants are directly related to the lattice dynamics and electronic structure of a solid. If the reflectance is done over a wide frequency range, a Kramers-Kronig analysis can correlate the measured data to the complex dielectric function, $\tilde{\varepsilon}(\omega)$. [110, 111] We can extract the optical constants including optical conductivity ($\sigma_1(\omega)$), plasma frequency (ω_p), oscillator strength (S), and relaxation time ($\tau(\omega)$) *etc.* These parameters often provide insight on the intrinsic properties of solids. Experimentally, the reflectance and transmittance are often carried out with combination of several light sources, spectrometers, and detectors. This chapter will describe the experimental and theoretical methods used in our spectroscopic work. It will also cover the use of physical tuning parameter, such as temperature.

2.1 Optical Properties of Solids

2.1.1 Maxwell's Equation and Optical Constants

The response of a solid to an external electric field is characterized by three macroscopic vectors: the electric field, E, the polarization, P, and the electric displacement, D. The electric displacement of the medium is related to the electric field and polarization by

$$D = \epsilon_0 E + P = \epsilon_0 \varepsilon E, \tag{2.1}$$

where, ϵ_0 is the electric permittivity (8.854×10^{-12} Fm^{-1} in SI units), and ε is the dielectric constant of the medium. It is an extremely important parameter in the understanding of the propagation of light in a solid.

The response of a materials to external magnetic field is treated in a similar way to the response of a solid in the electric field. The magnetic flux density, B, is related to the magnetic field, H, and magnetization, M, by

$$B = \mu_0 (H + M) = \mu_0 \mu H, \tag{2.2}$$

where, μ_0 is the magnetic permeability of the vacuum ($4\pi \times 10^{-7}$ Hm^{-1} in SI units), and μ is the magnetic permeability.

The theoretical description of the interaction of radiation with matter and the analysis of the experimental results are based on Maxwell's equations and on their solution for time-varying electric and magnetic fields. In the long wavelength limit, the propagation of electromagnetic wave can be described by the macroscopic Maxwell's

equations [110, 111]

$$\nabla \cdot D = \rho \tag{2.3}$$

$$\nabla \cdot B = 0 \tag{2.4}$$

$$\nabla \times E = -\frac{\partial B}{\partial t} \tag{2.5}$$

$$\nabla \times H = j + \frac{\partial D}{\partial t}. \tag{2.6}$$

where ρ is the free charge density, and j is the current density, which is related to the conductivity, σ, and the electric field by

$$j = \sigma E. \tag{2.7}$$

The direction of the electric field in an electromagnetic wave is called the polarization. Solving Maxwell's equation 2.3-2.6, the x-polarized wave propagating along the z direction as a plane wave. The components of the complex fields are of the form

$$E_x(z,t) = E_{x0} e^{i(k \cdot z - \omega t)} \tag{2.8}$$

$$E_y(z,t) = 0 \tag{2.9}$$

$$H_x(z,t) = 0 \tag{2.10}$$

$$H_y(z,t) = H_{y0} e^{i(k \cdot z - \omega t)}. \tag{2.11}$$

where k is the magnitude of the wave vector defined by $k = \frac{2\pi}{\lambda}$, where λ is the wavelength in the medium. ω is the angular frequency. On substituting Eqs.2.8 and 2.11 into Eq. 2.4 according to Eq. 2.2, we find

$$kE_{x0} = \mu_0\mu\omega H_{y0} \tag{2.12}$$

$$H_{y0} = \frac{E_{x0}}{Q}. \tag{2.13}$$

where $Q = \frac{k}{\mu_0\mu\omega} = \sqrt{\frac{\mu_0\mu}{\epsilon_0\varepsilon}} = \frac{1}{c\epsilon_0 n}$. Here, n is the refractive index of medium, and c is the speed of light in free space.

The boundary conditions at the interface between two dielectrics gives

$$E_x^i + E_x^r = E_x^t \tag{2.14}$$

$$H_y^i - H_y^r = H_y^t, \tag{2.15}$$

where the superscript labels i, r, and t refer to the incident, reflected, and transmitted beams respectively. By using Eqs. 2.12 and 2.13, we can rewrite Eq. 2.15 as

$$E_x^i - E_x^r = \tilde{n}E_x^t, \tag{2.16}$$

Equations 2.14 and 2.16 can be solved together to obtain

$$\frac{E_x^r}{E_x^i} = \frac{\tilde{n}-1}{\tilde{n}+1}, \tag{2.17}$$

This can be rearranged to obtain the reflectance, R

$$R = |\frac{E_x^r}{E_x^i}|^2 = |\frac{\tilde{n}-1}{\tilde{n}+1}|^2. \tag{2.18}$$

The complex refraction index [110, 111]

$$\tilde{n}(\omega) = n(\omega) + i\kappa(\omega), \tag{2.19}$$

and the complex dielectric constant

$$\tilde{\varepsilon}(\omega) = \varepsilon_1(\omega) + i\varepsilon_2(\omega).$$

where κ is the extinction coefficient, and $\tilde{n}(\omega)$ and $\tilde{\varepsilon}(\omega)$ are related by the following equation

$$\tilde{n}(\omega) = \sqrt{\tilde{\varepsilon}}. \tag{2.20}$$

We can work out explicit relationships between the real and imaginary parts of $\tilde{n}$ and $\tilde{\varepsilon}$

$$\varepsilon_1 = n^2 - \kappa^2 \tag{2.21}$$

$$\varepsilon_2 = 2n\kappa. \tag{2.22}$$

One can introduce a complex conductivity, [110, 111]

$$\tilde{\sigma}(\omega) = \sigma_1(\omega) + i\sigma_2(\omega).$$

We can also obtain the following relation

$$\tilde{\varepsilon}(\omega) = 1 + \frac{i\tilde{\sigma}(\omega)}{\omega\epsilon_0}, \tag{2.23}$$

or

$$\tilde{\varepsilon}(\omega) = \varepsilon_1(\omega) + i\varepsilon_2(\omega) = \varepsilon_1(\omega) + \frac{4\pi i\sigma_1(\omega)}{\omega}. \tag{2.24}$$

where $\sigma_1(\omega)$ is the frequency dependent (optical) conductivity. In the case of weak absorption, $\varepsilon_1 = n^2 - k^2 \approx n^2$, and $v \approx c/n$ (v is the velocity in the medium), the absorption coefficient α can be written as

$$\alpha = \frac{4\pi\sigma}{\varepsilon_1 v} = \frac{4\pi\sigma}{nc}. \tag{2.25}$$

2.1.2 Kramers-Kronig Analysis and Sum Rules

The dielectric function can be derived by Kramers-Kronig transformation of the reflectance spectrum.

On substituting Eq. 2.19 into Eq. 2.18, we find that the power reflectance is given by,

$$R(\omega) = rr^* = \frac{(n-1)^2 + \kappa^2}{(n+1)^2 + \kappa^2}. \tag{2.26}$$

The power reflectance and phase-dispersion shift $\phi(\omega)$ are related by Kramers-Kronig transformation: [110]

$$\phi(\omega) = \frac{\omega}{\pi}\int_0^\infty \frac{lnR(\omega) - lnR(\omega')}{\omega'^2 - \omega^2} d\omega'. \tag{2.27}$$

Since reflectivity

$$r = \sqrt{R}e^{i\phi}, \tag{2.28}$$

and combining Eqs. 2.26, 2.27, and 2.28, n and k can be determined by $R(\omega)$ and $\phi(\omega)$. Then from Eqs. 2.20 and 2.24, the real part of optical conductivity can be determined:

$$\sigma_1 = \frac{\omega\varepsilon_2}{4\pi} = \frac{\omega nk}{2\pi}. \tag{2.29}$$

In Eq. 2.27, the integration is from zero to ∞. Since our optical measurements usually cover the frequency range from far-infrared to ultraviolet, a proper extrapolation should be used. In this dissertation, in the low-frequency range, Hagen-Rubens relation, $R(\omega) = 1 - (2\omega/\pi\sigma_0)^{1/2}$, is used for metallic material; the low-frequency reflectance was extrapolated as a constant for semiconductor; in the high frequency, the optical response is mimicked by $R \sim \omega^{-e}$, where e varies from 0-4 and can be determined by comparing the absorption and calculated optical conductivity.

Together with physical arguments about the behavior of the response in certain limits, the Kramers-Kronig relation can also be used to derive sum rules. That is

$$\int_0^\infty \omega\varepsilon_2(\omega)d\omega = 1/2\pi\omega_p^2. \tag{2.30}$$

Where ω_p is the plasma frequency.

2.1.3 Lorentz Model for the Behavior of Model Oscillators

Starting with the Lorentz model [27, 110], one has

$$m\ddot{x} + m\gamma\dot{x} + m\omega_0^2 x = qE, \tag{2.31}$$

where x is the relative displacement of positive and negative ions, q is the effective ionic charge, m is the reduced mass E is the electric field, γ is the damping parameter and ω_0 is the spring constant frequency. This model applies to a certain vibrational mode of isolated oscillators such as gas phase molecules.

In a solid, due to the influence of neighboring oscillators, so called depolarization effect has to be considered. In this case E has to be replaced by the microscopic field [112]

$$E \to E_{mic} = E + \eta \frac{P}{\epsilon_0}, \tag{2.32}$$

where E_{mic} is the microscopic field that is really acting on the oscillator, E is the macroscopic field that should be used to calculate the dielectric constant, P is the polarization and η is the depolarization factor which depends on the topological arrangement of the oscillators.

Then Eq. (2.31) becomes

$$m\ddot{x} + m\gamma\dot{x} + m\omega_0^2 x = q(E + \eta \frac{P}{\epsilon_0}). \tag{2.33}$$

Our goal is to find the dielectric constant, in other words, the relation between E and P. However, in Eq. (2.33), there are 3 unknown variables, x, E and P. One needs to have one more equation in order to find the E and P relation, which will come from basically the definition of P. Assuming the polarization P is a linear combination of $P_i = \frac{xq}{V}$, which comes from relative displacements of ions, and $P_e = \frac{\epsilon_0 \alpha}{V} E_{mic}$ which is due to the distortion of electron clouds, one has

$$P = P_i + P_e = \frac{xq}{V} + \frac{\epsilon_0 \alpha}{V} E_{mic}, \tag{2.34}$$

where V is the volume for the oscillator, α is the polarizability of the oscillator. Invoking Eq. (2.32), one has the second important equation

$$P = \frac{1}{1 - \eta\alpha/V} (\frac{xq}{V} + \frac{\epsilon_0 \alpha}{V} E). \tag{2.35}$$

Bringing together Eq. (2.33) and Eq. (2.35), we can get the dielectric constant

$$\varepsilon = 1 + \frac{P}{\epsilon_0 E} = 1 + \frac{\alpha/V}{1-\eta\alpha/V} + \frac{q^2}{\epsilon_0 m V (1-\eta\alpha/V)^2} \frac{1}{\omega_0^2 - \omega_1^2 - \omega^2 - i\gamma\omega}. \quad (2.36)$$

We immediately recognize this expression as a modification of the Lorentz model in a solid (compared with that of isolated oscillator) because of the depolarization effect and the polarizability. (When $\alpha = 0$ and $\eta = 0$, Eq. (2.36) reduces to the case of isolated oscillator. [110])

2.1.4 Charge Bonding Models in Nanomaterials

The rigid ion model [10, 113] gives a precise relationship between the longitudinal and transverse optic phonon frequencies (often called the LO-TO splitting) and Born effective charge:

$$4\pi^2 c^2 \sum_j (\omega_{LO,j}^2 - \omega_{TO,j}^2) = \frac{N e^2}{\epsilon_0 \varepsilon_1(\infty) V} \sum_k \frac{(Z_B^*)_k^2}{m_k}. \quad (2.37)$$

Here, $\omega_{LO,j}$ is the longitudinal optic phonon frequency for the j-th oscillator, Z_{Bk}^* is Born effective charge on the k-th ion, N is the number of formula units in the unit cell, V is the volume of the MoS_2 formula unit, m_k is the atomic mass of the k-th atom, ϵ_0 is the permittivity of free space, e is the electronic charge, and c is the speed of light. The sum rule, $\sum Z_{B,k}^* = 0$, guarantees that the charge neutrality condition is fulfilled. In other words, the sum of Born effective charges for all atoms in the unit cell must vanish, element by element. [114] Unfortunately, Eq. (2.37) is valid only when the LO-TO splitting of a single crystal sample is known. Thus, it is not well-suited for assessing charge and bonding in nanomaterials as the latter are often in powder form. We can finesse this problem by employing oscillator strength changes (S) rather than LO-TO splitting, as described below.

Equation (2.36) and the generalized Lyddane-Sachs-Teller relationship [8] provide a way forward by articulating the relationship between dielectric constant, oscillator strength and the LO-TO splitting: $\varepsilon_1(\infty) \cdot (\omega_{LO,j}^2 - \omega_{TO,j}^2) = \omega_{TO,j}^2 \cdot S_j$. [2] Substituting this result into Eq. (2.37), we see that Born effective charge can also be calculated mode by mode from the knowledge of oscillator strength or effective plasma frequency:

$$4\pi^2 c^2 \sum_j (\omega_{p,j})^2 = 4\pi^2 c^2 \sum_j \omega_{TO,j}^2 S_j = \frac{N e^2}{\epsilon_0 V} \sum_k \frac{(Z_B^*)_k^2}{m_k}. \tag{2.38}$$

Where $\omega_{p,j}$ is the effective plasma frequency for the j-th oscillator. Note that, $(\omega_{p,j})^2 = \omega_{TO,j}^2 S_j$. This rendering is well-suited to the analysis of nanomaterials.

In an ionic solid, we need to consider the so-called depolarization field, which originates from the influence of neighboring ions. The polarization, $P = \frac{N}{V}(Z^* x + \alpha E_{eff})$, has two parts. The first contribution is due to the relative displacements of ions. The second results from electron cloud distortion around the polarizable ionic centers due to the macroscopic electric field E. Here, Z^* is the local effective charge (or dynamic ionic charge), α is the polarizability in one direction of the unit cell, E_{eff} is the microscopic electric field ($E_{eff} = E + \frac{\eta}{\epsilon_0} P$), n is the depolarization factor, and P is the polarization. [27, 112] Using these relationships, we can evaluate local effective charge and polarizability of the material as: [2]

$$Z_B^* = \frac{Z^*}{1 - \eta \frac{N\alpha}{V}} \tag{2.39a}$$

$$\varepsilon_1(\infty) = 1 + \frac{\frac{N\alpha}{V}}{1 - \eta \frac{N\alpha}{V}}. \tag{2.39b}$$

To employ these expressions in real materials, we found that several technical corrections had to be employed. They include density, orientation, surface scattering,

and capping ligand effects. These issues will be discussed in the text.

The charge and bonding analysis is based on a point charge model in an ionic solid. Using the infrared or Raman spectrum, we can estimate the Born and local effective charge as the translational symmetry, the depolarization field and the electron cloud distortion are considered in the system. The results are in good agreement with density functional theory (DFT) calculations, which indicates that a point charge model is capturing chemical bonding away from the Madelung limit. For example, the evaluation of Born effective charges for the Mn center is about 2.6 e using the charge and bonding analysis [3] compared to the value of 2.2-2.6 e using DFT calculations. [19]

2.2 Spectrometers

2.2.1 Bruker IFS 113v Fourier Transform Infrared Spectrometer

The majority of the far-infrared (30-600 cm^{-1}) and middle infrared (500-5000 cm^{-1}) reflectance and transmittance spectra in this work were obtained by using Bruker IFS 113v Fourier Transform Infrared (FTIR) spectrometer. The schematic of the optical components of the Bruker IFS 113v FTIR spectrometer is illustrated in Fig. 2.1. The spectrometer is divided into four chambers – source, interferometer, sample, and detector. Light from the source chamber is focused on the beamsplitter at a small angle of incidence, and is split into two beams, i.e., one reflected and one transmitted. Both reflected and transmitted beams go to a moving two-side mirror, which gives a path length difference. Then the two beams are recombined at the beamsplitter and directed through the sample chamber to the detector. The entire system is operated under vacuum.

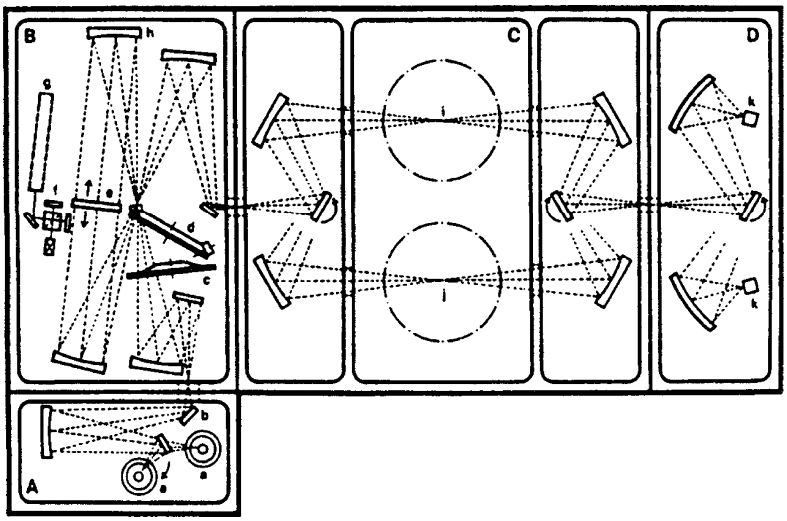

Figure 2.1: Optical layout of the Bruker 113V FTIR spectrometer.
A. Source Chamber; a- Tungsten lamp, Hg arc lamp, glowbar; b- automated aperture. B. Interferometer Chamber; c- optical filter; d- automatic beamsplitter changer; e- two-sided moving mirror; f- control interferometer; g- reference laser; h- remote control alignment mirror. C. Sample Chamber; i- sample focus; j- reference focus. D. Detector Chamber; k- far- and middle infrared deuterated triglycerine sulfate (DTGS) detector, far-infrared Si bolometer detector.

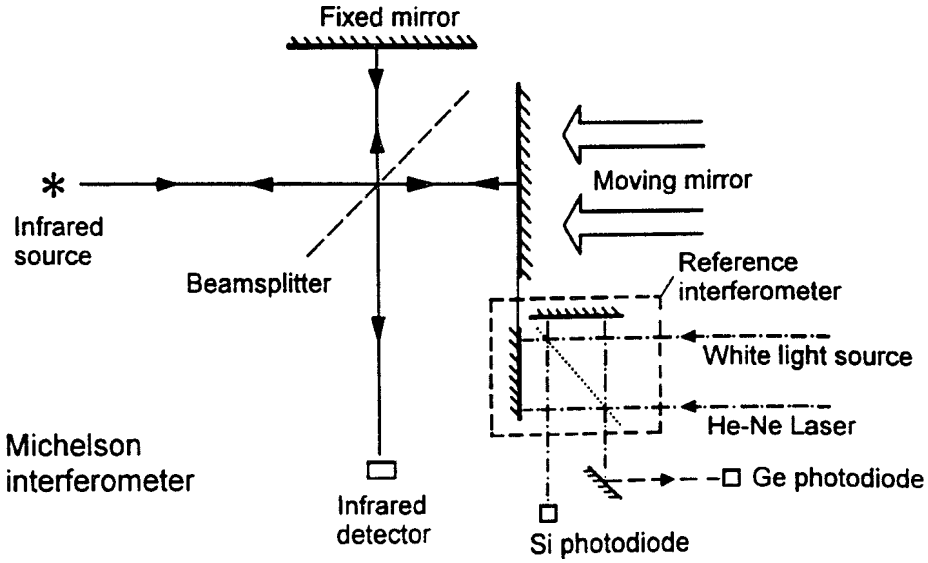

Figure 2.2: Schematic diagram of the Michelson interferometer

a) *Interferometer and beamsplitters*

The Bruker IFS 113v uses Genzel-type interferometer, which is similar to a Michelson interferometer. A Michelson interferometer is illustrated in Fig. 2.2. Here, the incident beam is split into two parts by a beamsplitter. Half of the radiation transmitted by beamsplitter is reflected from the movable mirror M_2. The other half is reflected onto the fixed mirror M_1. Both beams are recombined again at the beamsplitter, and recorded by detector D. The intensity of the recombined beams $I(x)$ (interferogram function) depends on the path difference between the fixed mirror M_1 and the moving mirror M_2. The plot of $I(x)$ as a function of path difference x is known as an interferogram. If M_2 travels at a constant velocity, the relation between interferogram function $I(x)$ and the source intensity $B(\omega)$ is given by

$$I(x) = 1/2 \int_0^\infty B(\omega) cos 2\pi\omega dx,$$

where ω is the frequency in wavenumbers. $I(x)$ is the cosine Fourier transform of $B(\omega)$, and contains complete information about the spectrum. Thus, the Fourier transform of the interferogram gives the single beam infrared spectrum. The typical transmittance or reflectance spectrum is the ratio spectrum of sample to reference.

In the Bruker IFS 113v, a secondary laser/white light interferometer physically attached to the main Genzel-type interferometer (as shown in Fig. 2.1) provides an "optical marker" to initiate the start of spectrum data acquisition and also to precisely determine the optical path difference and speed of the main moving mirror. The design is essential for accurate Fourier transformation.

b) *Source, beamsplitter, detector, and accessories*

In order to obtain the best far- and middle-infrared spectrum, we have to choose the appropriate combination of sources, beamsplitters, detectors, and polarizers. Table 2.1 lists the typical operating parameters.

Table 2.1: Bruker IFS 113v operating parameters

Range (cm^{-1})	Beam splitter	Opt. Filter	Source	Polarizer	Detector
10-50	Mylar 50 μ	Black PE	Hg arc	1	bolometer, DTGS
30-120	Mylar 23μ	Black PE	Hg arc	1	bolometer, DTGS
50-240	Mylar 12μ	Black PE	Hg arc	1	bolometer, DTGS
100-600	Mylar 3.5μ	Black PE	Hg arc	1	bolometer, DTGS
450-4000	KBr	open	Globar	2	DTGS

PE = polyethylene. Polarizer 1 = wire grid on oriented PE, Polarizer 2 = wire grid on AgBr

Typically, an external He-cooled Si bolometer detector made by Infrared Laboratory Inc. is used for far-infrared measurements. The intensity of a blackbody source becomes very weak in the far-infrared region, and the room-temperature DTGS detector does not have sensitivity to provide sufficiently high signal-to-noise ratio. The INFRARED Laboratory Inc. bolometer provides a much higher sensitivity (>100 times better than DTGS) and lower noise level (less than 1% at liquid helium temperature).

The spectra taken with different beamsplitters are merged together to give the whole spectrum in the far- and middle- infrared. The spectrum can be merged with the data taken with our Perkin-Elmer λ-900 spectrometer, if necessary.

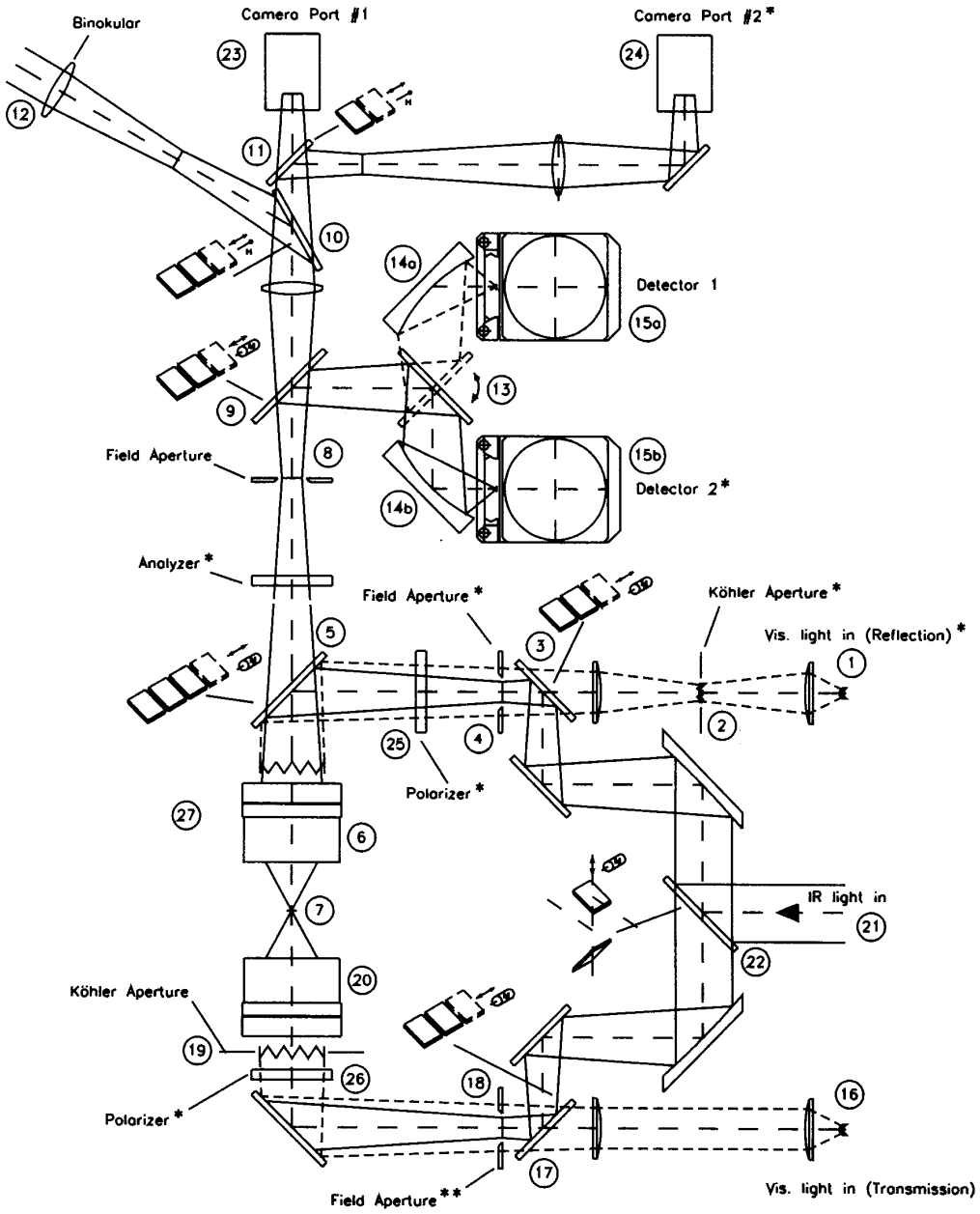

Figure 2.3: Optical path diagram of Bruker IRscope II. 1,16-visible light source; 2,19- visible light aperture; 3,22- motorized switch mirror; 4,18- optional iris or knife edge aperture; 5,9,10,17- beamsplitter changer; 6- Objective lens; 7- Sample; 8- Iris or knife edge aperture which defines the area of sample analyzed; 12- binocular eyepiece; 13- two position detector selection mirror; 14- mirror routing to detector; 15- detector; 20- condenser; 21- IR beam (from spectrometer); 23,24-camera port; 25,26,27- polarizer.

2.2.2 Bruker Equinox 55 Microscope

The Bruker IR Scope II is designed for accurate measurement of micro samples, or small areas on larger samples. In our lab, Bruker IRscope II combined with Bruker Equinox 55 FTIR spectrometer can be used to obtain the spectrum from the middle-infrared to visible range. It is ideal for small crystals, small edges of a crystal, and checking the absolute reflectance level obtained on the other instruments.

Bruker Equinox 55 FTIR spectrometer is equipped with a Globar source, two beamsplitters, and a DTGS detector. It has an external port to transfer the incident light to the IRscope II. IRscope II has three objectives (4×, 15×, and 30×), and several detectors (MCT, InPb, and Si diode) to cover the energy range from 600-16000 cm^{-1}.

Figure 2.3 shows the optical path of Bruker IRscope II. The IRscope II can measure reflectance or transmission of the sample by changing the orientation of mirror 22. The infrared or visible mode can be chosen depending on the orientation of mirror 3 (reflectance mode) or 17 (transmission mode). The detector can be changed by flipping mirror 13. Table 2.3 lists the operating parameters of Bruker Equinox 55 FTIR spectrometer combined with IRscope II. The spectrometer is operated under N_2 purge.

2.2.3 Perkin-Elmer λ-900 Spectrometer

The near-infrared (NIR)/Visible (Vis)/Ultraviolet (UV) spectra in this dissertation were measured on the Perkin-Elmer λ-900 Spectrometer. The Perkin-Elmer λ-900 Spectrometer features an all-reflecting, double-monochromator, double-beam optical system. The energy range covered by the λ-900 Spectrometer is 3300-190 nm ($\approx$ 3000-52000 cm^{-1}). The spectrometer is operated under nitrogen purging. The optical system is depicted schematically in Fig. 2.4.

Table 2.2: Bruker IRscope II operating parameters

Range (cm^{-1})	Source	Beam splitter	Detector
600-8000	Globar	KBr	MCT
7500-12500 with near-infrared polarizer	Tungsten	Quazi	InPb
12300 -16000 with visible polarizer	Tungsten	Quazi	Si diode

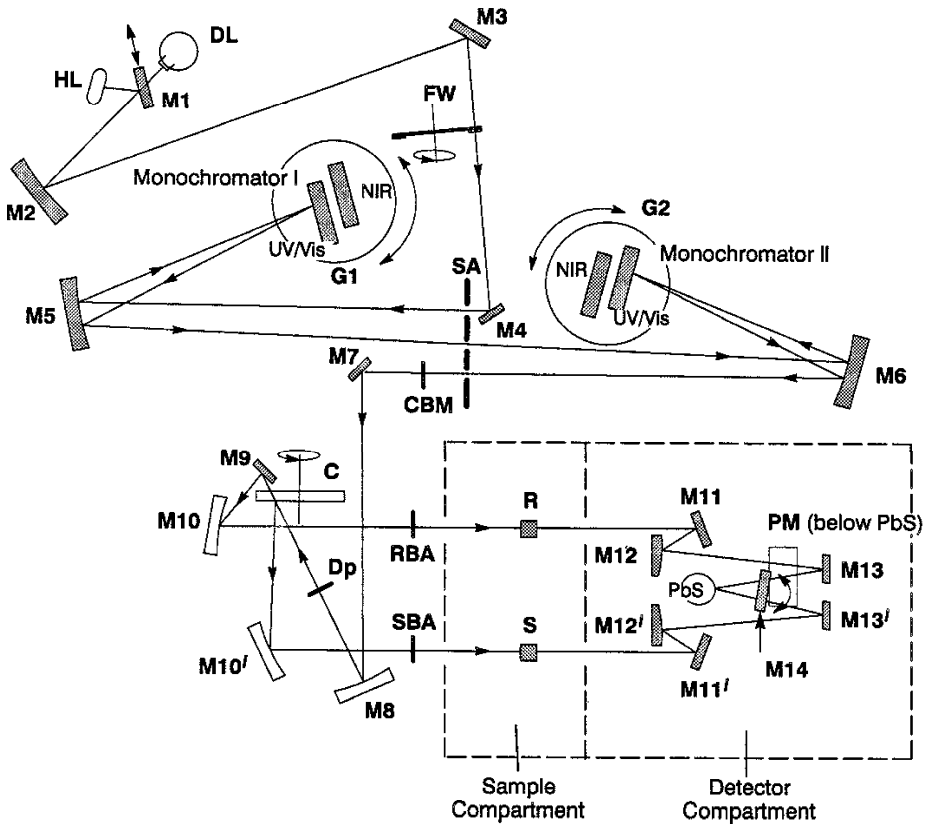

Figure 2.4: Optical layout of Perkin-Elmer λ-900

Table 2.3: λ-900 operating parameters

Range (cm^{-1})	Source	Gratings	Detector
3100-14250	Halogen Lamp	1200 lines/mm	PbS
11240-31330	Halogen Lamp	1200 lines/mm	Photomultiplier
31330-52000	Deuterium Lamp	2400 lines/mm	Photomultiplier

There are two radiation sources, a deuterium lamp (DL) and a halogen lamp (HL). Halogen lamp is used for NIR and Vis range, and deuterium lamp is used for UV range. Source change is controlled by flipping mirror M1. The radiation of source is reflected by mirror M2, M3, and passes optical filter FW. Then, the beam is brought in monochromator I through M4, slit SA, and M5. Depending on the desired wavelength range, the collimated radiation beam strikes either the 2400 lines/mm grating or the 1200 lines/mm grating. The rotation position of the grating effectively selects a segment of the spectrum, reflecting this segment to mirror M5, to go through the exit slit, and enter Monochromator II. The advantage of the double-monochrometer is to maintain high spectral purity with an extremely low stray radiation content. The automatic grating change during monochromator slewing avoids the time-consuming re-alignment of the optics pathway due to themonochromator change.

The double beam is achieved via the chopper assembly C. As the chopper rotates, a mirror segment, a window segment and two dark segments are brought alternately into the radiation beam. When a window segment enters the beam, radiation passes through to mirror M9 and is then reflected via mirror M10 to create the reference beam (R). When a mirror segment enters the beam, the radiation is reflected via

mirror M10′ to form the sample beam (S). When a dark segment is in the beam path, no radiation reaches the detector, permitting the detector to create the dark signal (D). Then, the measured spectrum is expressed as

$$spectrum = (S - D)/(R - D).$$

Two detectors are used in the Perkin-Elmer λ-900 spectrometer. A photomultiplier is used in the UV/Vis range while a lead sulfide (PbS) detector is used in the NIR range. Detector change is automatic by rotating mirror M14 during scans.

2.2.4 Reflectance Stage and Polarizers

To measure the absolute reflectance spectrum, a reflectance stage (as shown in Fig. 2.5) is used to bring the near normal incident (<6°) light to a solid sample or reference mirror. An aluminum mirror is usually used as a reference material to obtain a baseline scan, then the reflectance spectrum of the sample is measured relative to the baseline. The absolute reflectance spectrum ($R_{Abs.}$) of the sample is obtained by renormalizing the measured spectrum ($R_{Meas.}$) with absolute Al mirror reflectance (R_{Al}) using $R_{Abs.} = \frac{R_{Meas.}}{R_{Al}}$.

The optical theory outlined in Section 2.1 is based on Maxwell's equations (2.3–2.6) and Eqs. 2.1, 2.2, and 2.7. These equations are the material equations for an isotropic medium. In an anisotropic crystal, $\vec{D}$ and $\vec{E}$ are related by the following form:

$$D_x = \varepsilon_{xx}E_x + \varepsilon_{xy}E_y + \varepsilon_{xz}E_z, \tag{2.40}$$

$$D_y = \varepsilon_{xy}E_x + \varepsilon_{yy}E_y + \varepsilon_{yz}E_z, \tag{2.41}$$

$$D_z = \varepsilon_{zx}E_x + \varepsilon_{zy}E_y + \varepsilon_{zz}E_z. \tag{2.42}$$

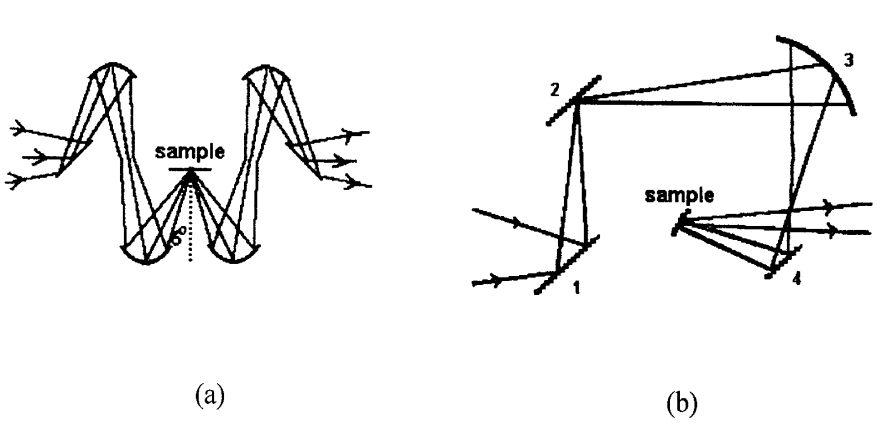

Figure 2.5: Reflectance set-up for (a) Bruker IFS 113v FTIR and (b) Perkin-Elmer λ-900

The nine qualities ε_{xx}, ε_{xy}, ...are constants of the medium, and constitute the dielectric tensor. It is always possible to find a set of axes, *the principle dielectric axes*, such that the complex dielectric tensor can be put into diagonal form, i.e.,

$$\varepsilon(q,\omega) = \begin{vmatrix} \varepsilon_{xx} & 0 & 0 \\ 0 & \varepsilon_{yy} & 0 \\ 0 & 0 & \varepsilon_{zz} \end{vmatrix}. \tag{2.43}$$

Along the principle axes, $\vec{D}$ and $\vec{E}$ have the same directions. Since the dielectric tensor varies with frequency, the directions of the principal axes may also vary with frequency. This dispersion of the axes can arise only in crystals with monoclinic and triclinic symmetry. In the reflectance experiment on single crystals, the principal axes can be determined by considering the crystal shape and measuring the polarization dependence of the reflectance response in order to find the dielectric tensor along the principle axes of the single crystals.

For nanoscale materials and powders, the orientations of the crystallographic axes will be random in the pellet due to different pressures and other conditions. For a triclinic sample, the total $\varepsilon_{tot}(\omega)$ along the direction of electric field E is

$$\varepsilon_{tot}(\omega) = \sum_{i=1}^{N} \frac{v\omega_{p,i}^2 sin^2\beta}{\omega_i^2 - \omega^2 - i\omega\gamma_i} + \sum_{j=1}^{N} \frac{v\omega_{p,j}^2 sin^2\beta sin^2\varphi}{\omega_j^2 - \omega^2 - j\omega\gamma_j} + \sum_{k=1}^{N} \frac{v\omega_{p,k}^2 sin^2\beta cos^2\varphi}{\omega_k^2 - \omega^2 - k\omega\gamma_k} + \varepsilon_{1,tot}(\infty). \tag{2.44}$$

where ω_i is the TO frequency of the ith oscillator, and $\omega_{p,i}$ is the effective plasma frequency (or oscillator strength), γ_i is the damping factor of corresponding mode, $\varepsilon_{1,tot}(\infty)$ is the total high-frequency dielectric constant, β is the polar angle between E and z axis, and φ is the the azimuth angle, N is the number of formula units in the unit cell, v is the relative density of a powdered vs. single crystalline sample.

Using Eq. 2.44, a fitting analysis can be carried out based on the measured infrared vibrational spectra of a nanoscale material or a bulk. A Kramers-Kronig analysis of the reflectance can also obtain all the optical constants of the material. As we figure out β, the intrinsic values of ω_p and $\varepsilon_1(\infty)$ can be obtained by the application of appropriate corrections for density and orientational effects. Using Eqs. 2.38, 2.39a, and 2.39b, we can evaluate charge and bonding in the sample. The results are important for understanding finite length scale effects in the nanoscale material.

2.2.5 Low-Temperature Techniques

The low-temperature measurements were carried out with an open-flow cryostat. For the low-temperature experiments with the Bruker IFS 113v and Perkin-Elmer λ-900, an APD LT-3-110 Heli-Tran Liquid Transfer Refrigeration system with dual temperature sensors together with a Lakeshore Model 330 temperature controller were adapted. The principles of operation are illustrated in Fig. 2.6. Cooling is accomplished by a controlled liquid He transfer through a high efficient transfer line to a heat exchanger adjacent to the sample interface. A needle valve at the end of the

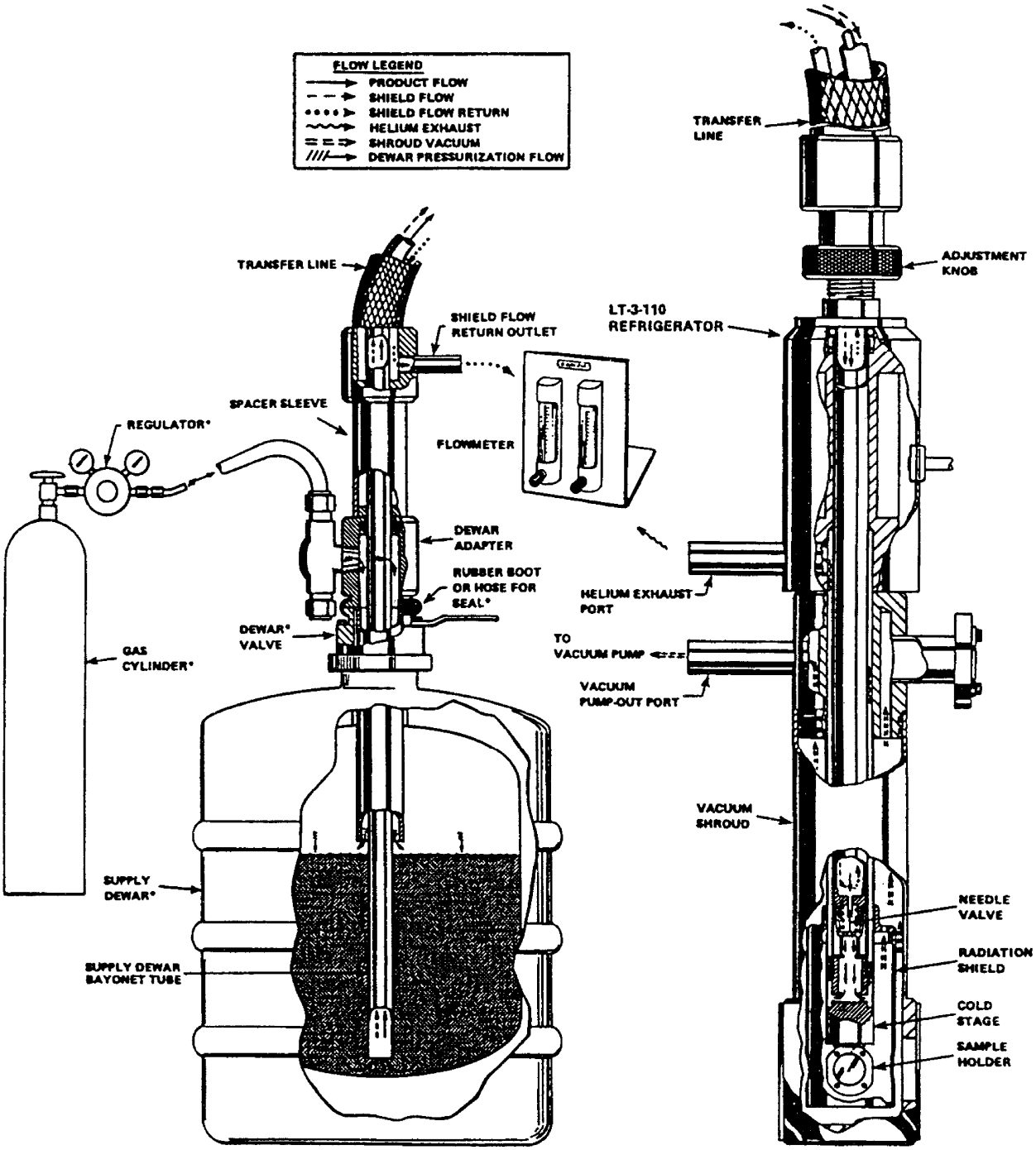

Figure 2.6: Set-up of LT-3-110 Heli-Tran liquid transfer line and cryostat.

Heli-Tran transfer line permits precise control of the flow rate. The cooling rate can be regulated by changing the pressure of the supply dewar, adjusting the flowmeter and optimizing the position of the needle valve. It often takes about 25 minutes to precool the system, and the lowest stable temperature obtained is $\sim$ 5 K.

To improve the thermal contact, crycon grease is placed between the cold stage of the cryostat and the sample holder, and the sample is mounted on the sample holder with GE Varnish and silver paste. There are two thermal sensors inside the cryostat, one is embedded in the tip of the cold stage, the other one is mounted on the sample holder. In this configuration, the temperatures provided by the two sensors allow us to estimate the real sample temperature.

2.3 Materials of Interest and Measurement Details

2.3.1 Inorganic Fullerene-Like MoS_2 Nanoparticles

IF-MoS_2 was synthesized by a gas phase reaction from MoO_3 powder by a three-step procedure in a vertical bed reactor. [37] The resulting nanoparticles ranged in size from $\sim$30-70 nm in diameter (Fig. 2.7). 2H-MoS_2 was purchased directly from Alfa Aesar (99%). Pressed pellets were prepared for investigating their dynamical properties. Note that the theoretical calculated density of 2H-MoS_2 single crystal is 4.996 g/cm^3, and the actual densities of bulk and nanoparticle pellets are $\sim$3.5 g/cm^3. Pellets were prepared using a 5 mm die with very modest pressure, so we do not anticipate that density will approach that of a single crystal as it would if high pressures were employed. Once we measure the weight (m) and pellet thicknesses (h), we can straightly estimate the density (ρ) as $\rho = \frac{m}{\pi \cdot 5^2 \cdot 10^{-2} h}$. We find that pellet densities are $\sim$70% of the single crystal density, a difference that we correct for in

our analysis. [115]

Near normal infrared reflectance was measured over a wide frequency range using a series of spectrometers including a Bruker 113V Fourier transform infrared spectrometer, an Equinox 55 Fourier transform instrument (equipped with a microscope attachment), and a Perkin Elmer Lambda 900 grating spectrometer, covering the frequency range from 25 - 52000 cm^{-1}. A helium-cooled bolometer detector was employed in the far-infrared for added sensitivity. 0.5 cm^{-1} resolution was used in the infrared, whereas 3 nm resolution was employed in the optical regime. A 2000 Å aluminum overcoat was used to correct for the associated scattering effects. A Lorenzian oscillator analysis was used to (i) fit the measured reflectance and (ii) cal-

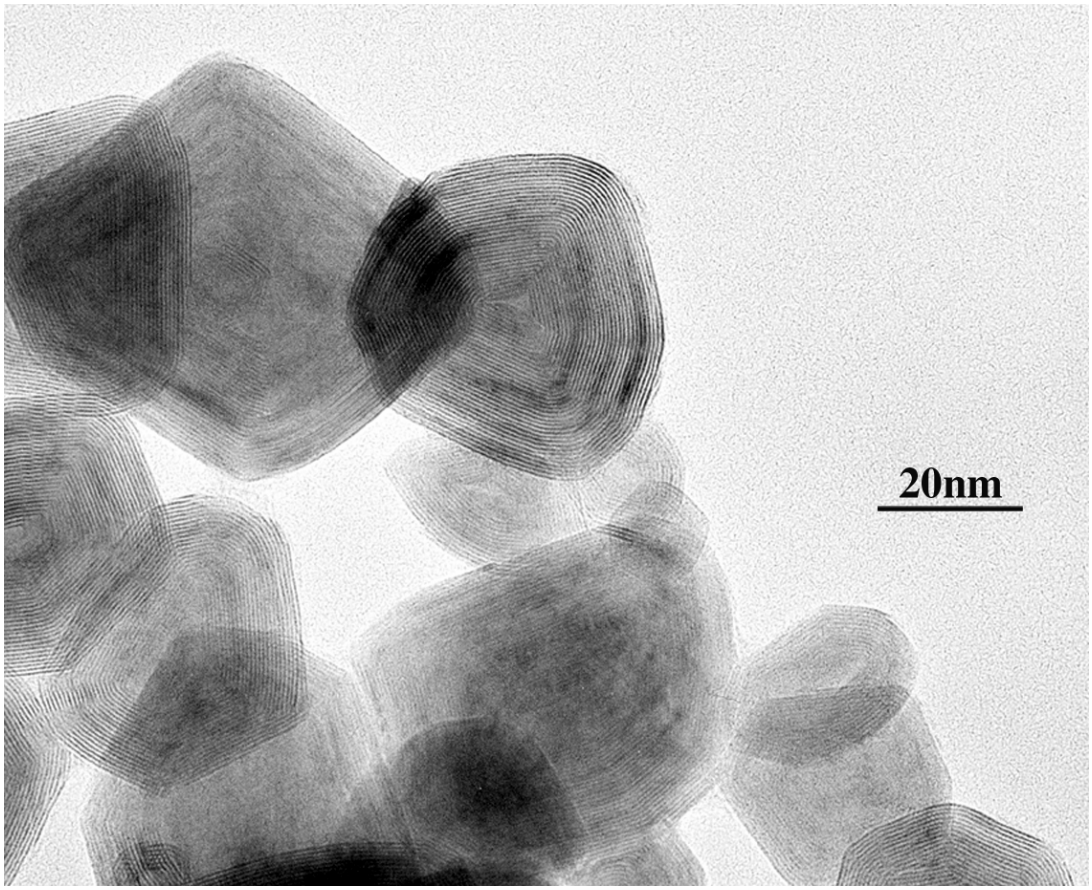

Figure 2.7: TEM image of MoS_2 Nanoparticles. [1]

culate the optical constants from the extracted parameters, yielding information on the dispersive and lossy response of each material. [15] A Kramers-Kronig analysis can also be used to obtain the optical constants. [110]

2.3.2 Bulk and Nanoscale MnO and Spectral Corrections

MnO Nanoparticle Synthesis

MnO nanoparticles were synthesized using a manganese-fatty acid salt combined with an additional activating/directing agent in 1-octadecene. [116, 117] Manganese (II) chloride tetrahydrate, myristic acid (HMy; $CH_3(CH_2)_{12}CO_2H$), tetramethylam-

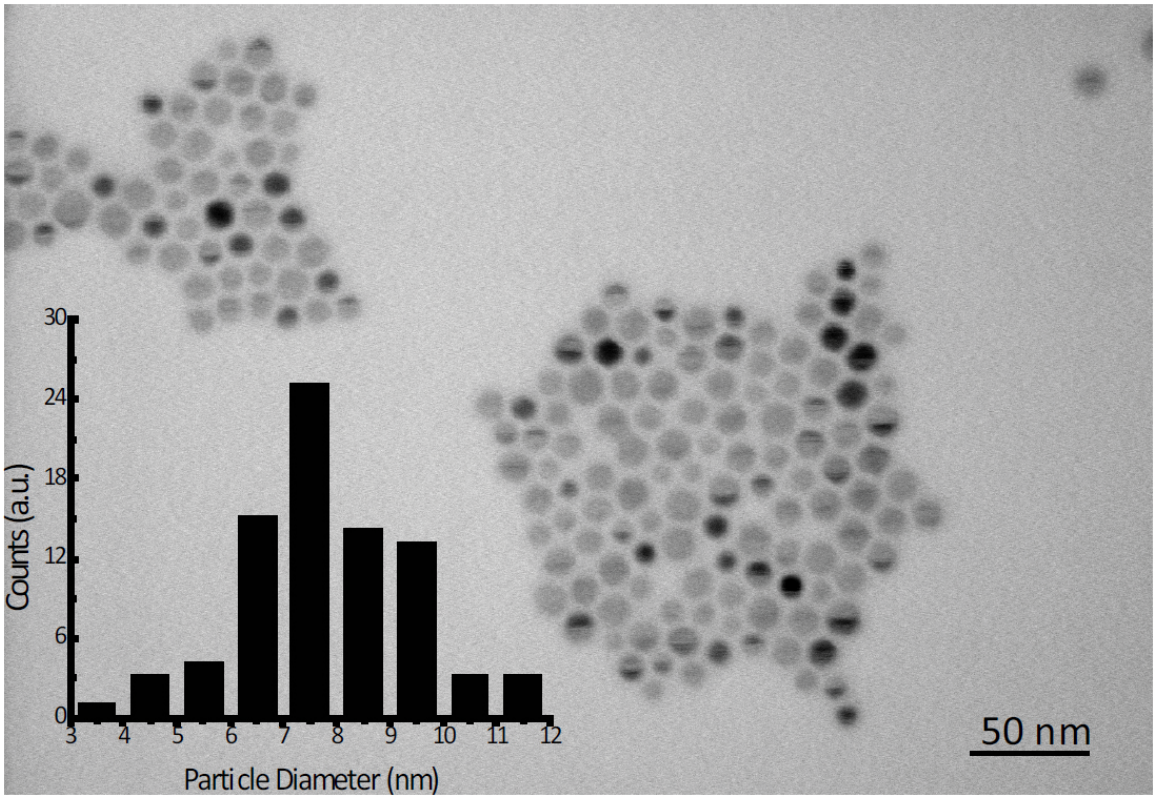

Figure 2.8: STEM image of 8 nm MnO nanoparticles. The inset contains a histogram indicating the average size distribution. This method reproducibly yields 8 nm particles. Our growth process was not able to produce a variety of sizes. [3]

monium hydroxide pentahydrate, 1-octadecene (ODE), 1-octadecanol, methanol, toluene, and acetone were purchased from Fisher Scientific and used as received.

Step 1: $Mn(My)_2$ synthesis. Formation of MnO nanoparticles was based upon modification of non-injection synthetic schemes reported recently by Peng and coworkers. [116,117] In a typical synthesis, 10 g HMy was dissolved in 100 mL methanol and neutralized by adding dropwise exactly one equivalent (7.1 g) of tetramethylammonium hydroxide pentahydrate in 30 mL anhydrous methanol while stirring. To this solution, half an equivalent (3.9 g) of $MnCl_2{\cdot}5H_2O$ dissolved in methanol was slowly added while stirring. Immediately, a white precipitate of $Mn(My)_2$ formed, and the reaction was stirred for 1 hour to ensure completion. The $Mn(My)_2$ precipitate was filtered and washed no less than five times with methanol and dried under vacuum overnight to remove any remaining methanol.

Step 2: MnO synthesis. $Mn(My)_2$ (2g), HMy (0.45g), and ODE (30 mL) were combined in a 100 mL 3-necked flask and heated to 305 °C while stirring under Ar for 5 min (for 8 nm particles) during which the solution developed a deep brownish black color signifying the formation of MnO nanoparticles. The resulting MnO nanoparticles were precipitated with acetone and centrifuged at 8000 rpm for 10 min followed by removal of the supernatant liquid. The particles were then re-suspended in toluene and precipitated again using either acetone or methanol as anti-solvent. This precipitation/re-suspension procedure, which represents one cleanup cycle, was repeated no less than three times to achieve uncontaminated MnO nanoparticles. Our growth process was not able to produce a variety of sizes.

MnO Nanoparticle Characterization

Scanning transmission electron microscopy images were taken on a Hitachi HD2000 STEM. The nanoparticles were first dispersed in toluene or hexane, and then a

copper grid covered in a carbon type A thin film with Formvar backing (Pella) was dipped into the solution and allowed to dry in air. The size and distribution of the nanoparticles for a given sample were determined using Scion Image software. Representative STEM images of 8 nm MnO nanoparticles are displayed in Fig. 2.8 (size distribution histogram inset) providing evidence the samples are composed of well-defined nanoparticles with a low degree of agglomeration. The average particle diameter estimated from transmission electron microscopy is 8 ± 1.8 nm (Fig. 2.8), consistent with that obtained from x-ray diffraction.

Figure 2.9 shows the X-ray diffraction (XRD) pattern of 8 nm MnO. The XRD experiments were carried out on a Philips X'Pert Pro diffractometer with Cu Kα ($\lambda = 1.54060$ Å) radiation. By analyzing the line widths from the Rietveld fits, an

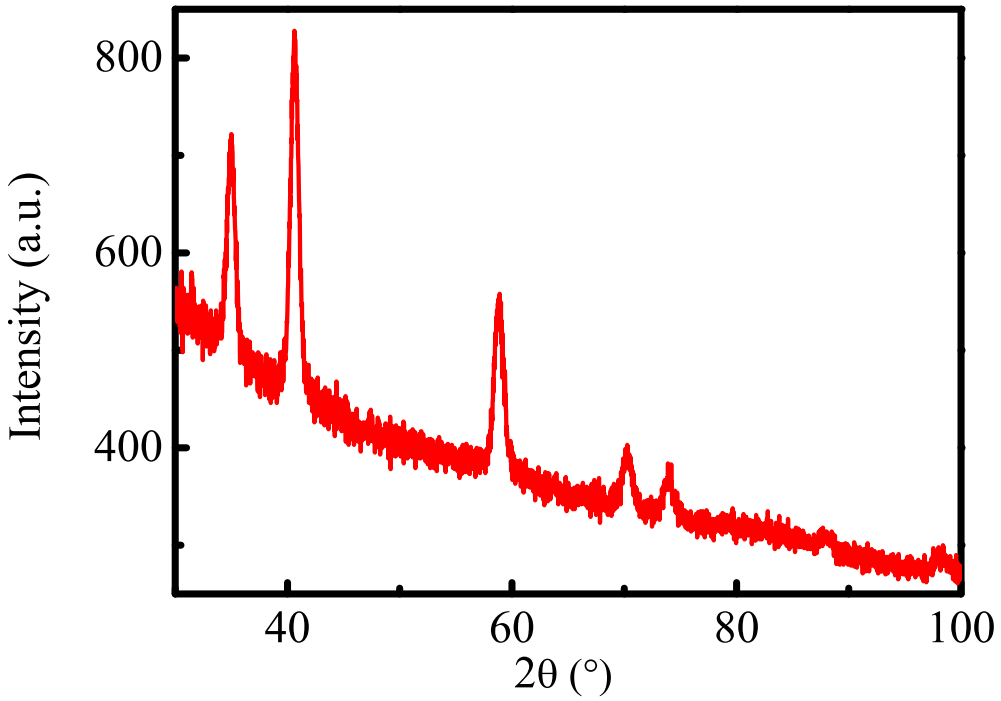

Figure 2.9: 300 K x-ray diffraction pattern of 8 nm MnO nanoparticles. [3]

average particle size of 9.8 nm was extracted using the Scherrer formula. The average size of the nanoparticles as determined by STEM correlates well with the diameter calculated from XRD data indicating that the particles are single crystalline. Further, no peaks from other Mn-O phases or other byproducts originating from the synthesis procedure were detected, indicating a high purity of the MnO nanoparticles obtained by our synthetic route. The recovered lattice parameter value of $a_0 = 4.439$ Å agrees well with the reported data for the bulk crystals, $a_0 = 4.445$ Å (ICDD PDF no. 7-230). [118] The nanoparticles are isostructural with the bulk within our sensitivity. [119]

Thermogravimetric analysis (TGA) was carried out using a TA Instrument Q-50 TGA. Figure 2.10 shows the presence of organic capping ligands evidenced from

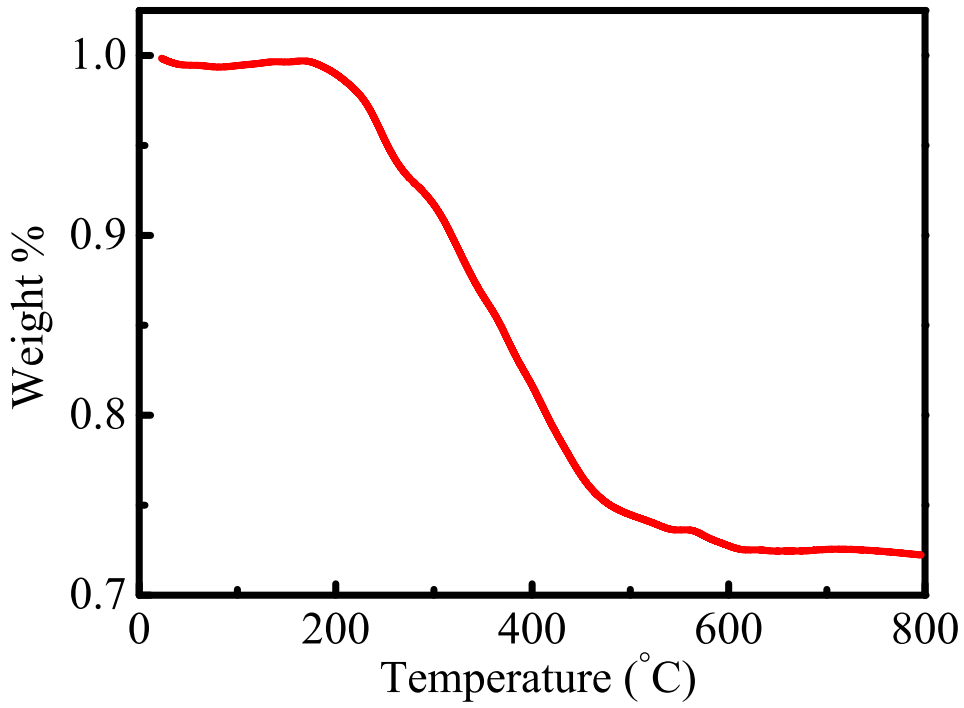

Figure 2.10: TGA curve for the 8 nm MnO nanoparticles. The experiment was carried out in a nitrogen atmosphere at a heating rate of 10 °C min^{-1}. [3]

the TGA curve. For 8 nm particles, the organic capping ligands are fully removed around 470 °C. The mass fraction of organic capping ligands is about 25%. This result establishes $x_{Cap} \approx 0.25$. The presence of organic capping ligands stabilizes the uncompensated surface and helps to avoid the oxidation of the MnO nanoparticles.

MnO Single Crystal, Bulk Powder, and Nanoparticles

For comparison, a well-polished (100) oriented MnO single crystal and MnO bulk powder (99.99+%) were purchased directly from Princeton Scientific and Sigma Aldrich, respectively. The average particle diameter in the bulk powder was 0.25 mm. Pressed pellets of nanoscale and bulk powder MnO were prepared in order to investigate their dynamical properties. Pellet densities are ∼47 and ∼74% of the single crystal density. [120] Figure 2.11 displays photographs of all sample surfaces. As expected, the highly-polished single crystal (Fig. 2.11(a)) is of optical quality, whereas surface roughness effects are evident in the bulk powder (Fig. 2.11(b)) and nanoparticle (left-hand image, Fig. 2.11(c)) pellets. The right-hand side of Fig.2.11(c) shows a transmission electron microscopy image of 8 nm nanoparticles.

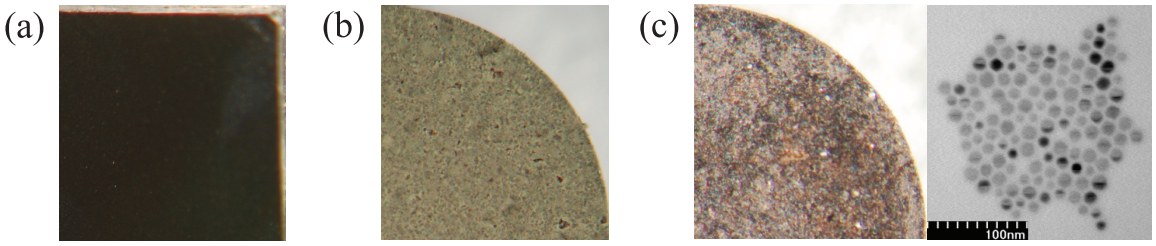

Figure 2.11: (a) Photo of the single crystal surface. (b) Photo of the bulk powder pellet surface. (c) Right: photo of the nanoparticle pellet surface. Left: a TEM image of 8 ± 1.8 nm nanoparticles. The scale bar is 100 nm. [3]

Vibrational Spectra and Spectral Corrections

Near normal infrared reflectance was measured using a series of spectrometers including a Bruker 113V Fourier transform infrared spectrometer, an Equinox 55 Fourier transform instrument (equipped with a microscope attachment), and a Perkin Elmer Lambda 900 grating spectrometer, covering the frequency range from 25 - 52000 cm^{-1}. A helium-cooled bolometer detector was employed in the far infrared for added sensitivity. 2 cm^{-1} resolution was used in the infrared, whereas 3 nm resolution was employed in the optical regime. As mentioned above, surface roughness effects are important for both the bulk powder and nanoparticle pellets. A 2000 Å aluminum overcoat was used to correct for the associated scattering effects. [121] We also sought to account for the spectral contribution of the capping ligand in the nanoparticle response. [122] This was done with a traditional two-layer multiple reflectance model, [123] shown schematically in the upper left inset of Fig. 5.1(a). [124] Combining the various reflectance and transmittance processes, we can express the reflectance of nanoscale MnO as $R_{MnO} = \frac{R_{Meas} - R_{Cap}}{1 - 2R_{Cap} + R_{cap}R_{Meas}}$. Here, R_{MnO} is the corrected reflectance of nanoscale MnO, R_{Cap} is the reflectance of capping ligands in isolation (assumed to be constant at 0.022, a reasonable value for an organic), and R_{Meas} is the measured reflectance. The upper right inset of Fig. 5.1(a) shows a comparison of the measured and corrected reflectance of the nanoparticles. The net effect is to shift the reflectance to give a better defined plasma edge. The various capping ligand, density, and scattering modifications are summarized in Table 2.4.

Table 2.4: Summary of the sample and spectral corrections used in the MnO project.

Correction	Single crystal	Bulk powder	Nanoparticles
Surface scattering	-	Aluminum overcoat	Aluminum overcoat
Capping ligand reflectance	-	-	Two layer model
Pellet densitys effects	-	0.74 density[a] scaling factor	0.47 density scaling factor[a]
Quantity of capping ligand	-	-	Thermogravimetric analysis $x_{Cap} = \sim 0.25$, $x_{MnO} = \sim 0.75$ [b]

[a] This is the density relative to that of the single crystal.
[b] The mass fractions x_{Cap} and x_{MnO} account for the relative quantity of mysteric acid ligand and MnO, respectively, in the sample.

2.3.3 $CoFe_2O_4$ Nanoparticles

Nanoparticle Synthesis

Our $CoFe_2O_4$ nanoparticles were prepared by high-temperature decomposition of the metal precursors following the method presented by Sun et al. [100,125] All chemicals were used as received from Sigma-Aldrich and handled in a N_2 filled glovebox except for the capping agents. The cobalt and iron acetylacetonates (acac) were refluxed in benzyl ether at relatively high temperatures (260 °C) in the presence of oleylamine and oleic acid. Nanoparticles with sizes between approximately 5 and 14 nm were obtained by varying the reaction time or the amount of surfactants. For the synthesis of about 5 nm particles $Co(acac)_2$ (1 mmol), $Fe(acac)_3$ (2 mmol), oleic acid (6 mmol)

and oleylamine (6 mmol) were mixed in 20 ml benzyl ether under N_2. The mixture was first heated at 200 °C for 30 min and then at reflux for another 30 min. After cooling down the particles were collected by adding 50-70 ml ethanol (and a small amount of toluene to remove the particles from the magnetic stir bar) and subjected to centrifugation (15 min). The product was dissolved in about 10 ml toluene and re-precipitated with 50-70 ml ethanol to remove the surfactants. To obtain 7 nm particles the same mixture was heated at 200 °C for 60 min and at reflux for 120

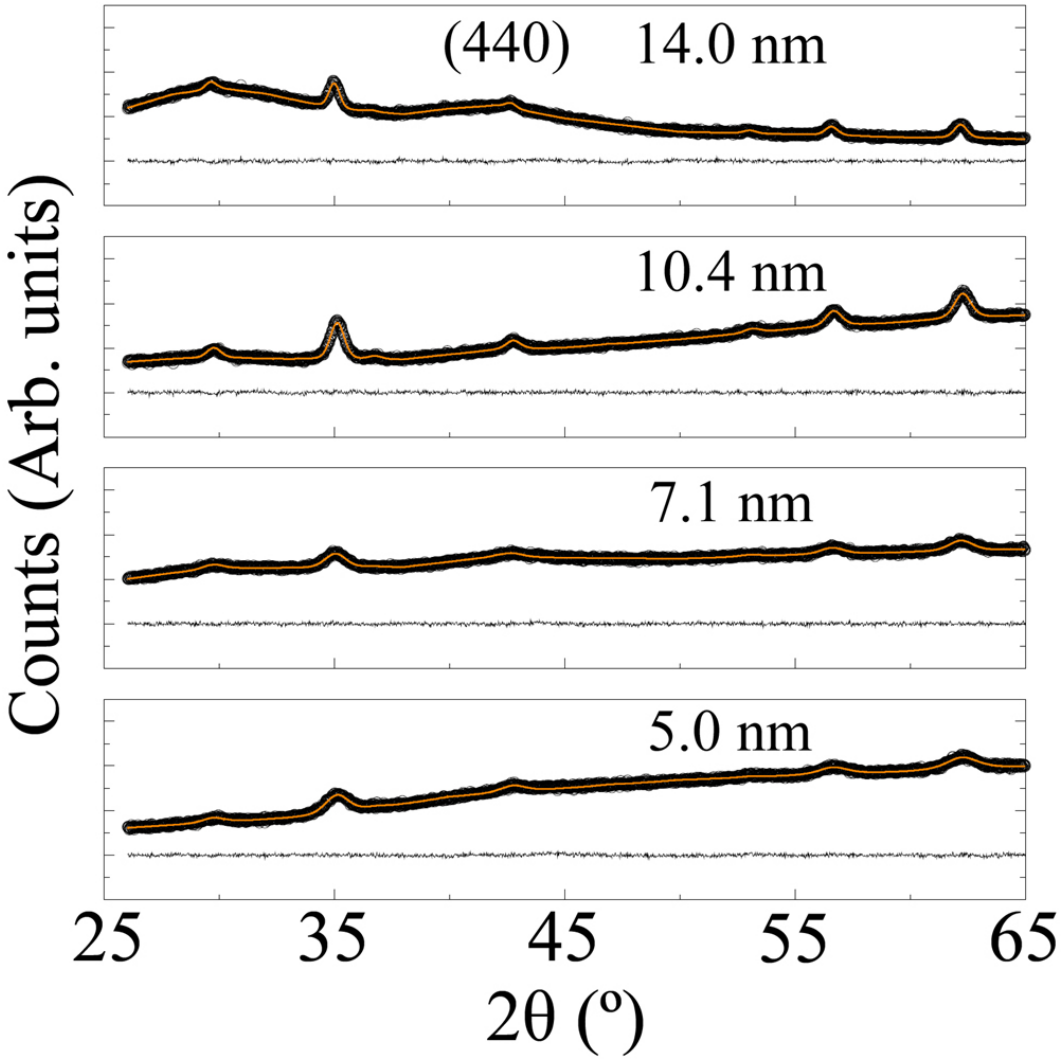

Figure 2.12: X-ray diffraction data (black open circles) and Rietveld profile fits (orange solid line) of the $CoFe_2O_4$ nanoparticles. The sizes were calculated by Scherrer-broadening using the (440) spinel reflection. [5]

min. The 10 nm particles were prepared as above with 4.5 mmol oleylamine and oleic acid and the 14 nm particles were prepared with 1.5 mmol oleylamine and oleic acid. Spinel nanoparticles are also accessible by a number of other synthetic methods, [126–129] although as indicated above, we followed the procedure discussed in Sun's paper. [100, 125].

Structure and Size Determination

Figure 2.12 shows the x-ray diffraction patterns of the different sized nanoparticles. These were collected on powder samples using a Philips MRD diffractometer with Cu-Kα radiation ($\lambda = 1.5418$ Å) and a graphite monochromator. Data were acquired over the angular range 25-65° (2θ) with a step size of 0.1° (2θ). The x-ray data were subject to Rietveld refinement and the Scherrer-broadening formula using the (440) spinel reflection. The recovered lattice parameter values are 8.4179(3), 8.4160(2), 8.4119(1), and 8.4143(1) Å for 5.0, 7.1, 10.4, and 14.0 nm particles, respectively. They are almost identical within our sensitivity. X-ray analysis indicates that the nanoparticles are essentially isostructural with the bulk. The preparation of pure $CoFe_2O_4$ nanoparticles is also confirmed by energy dispersive x-ray spectroscopy. As discussed below, the particle sizes determined by x-ray diffraction and TEM are fairly consistent. We feel, however, that analysis of x-ray peak Scherrer broadening is the superior method for providing particle size in this case because it samples a large number of particles and provides a robust average size. This is in contrast to TEM, which advantageously furnishes a size distribution but samples a relatively small number of particles on the grid.

Transmission electron microscopy images of the four different sizes of $CoFe_2O_4$ nanoparticles were obtained in order to verify particle size and determine the size distribution in the samples. Figure 2.13 shows that the particles are fairly monodisperse.

The average size of the nanoparticles (5.8±0.7, 7.8±0.9, 15.6±2.7, 15.6±2.6 nm respectively), which correlates well with the diameter calculated from x-ray diffraction

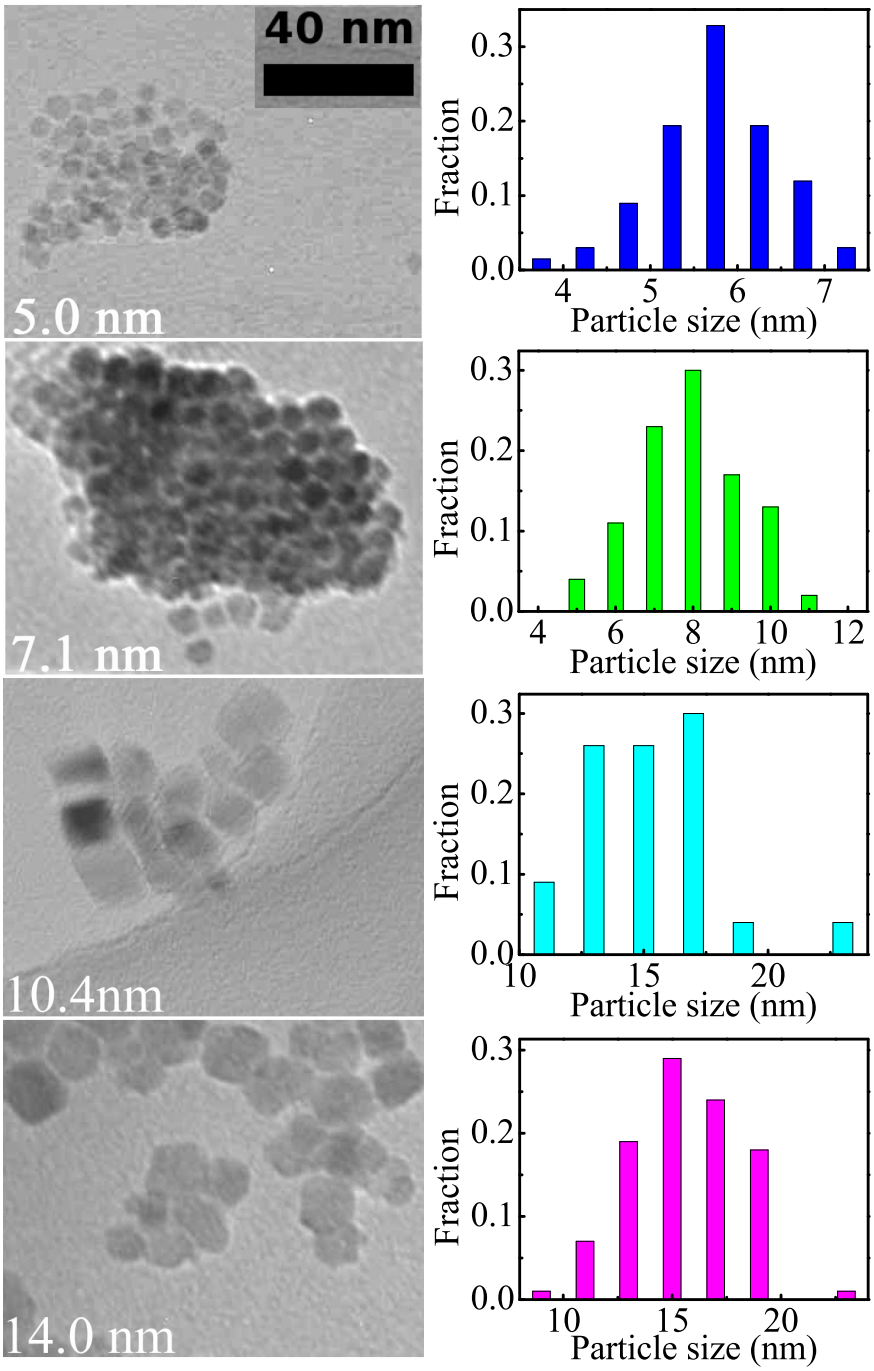

Figure 2.13: Transmission electron microscopy images and histograms of the four different sizes of $CoFe_2O_4$ nanoparticles. The sampling number is ~70 in each case. [5]

data, indicating that the particles are single crystalline. The transmission electron microscopy sizes are larger than those determined from x-ray diffraction. This is a common finding, but it's especially true for the 10 nm $CoFe_2O_4$ sample, which has the broadest size distribution. This finding illustrates the challenge of particle size distribution by TEM (which provides only local area information). We therefore elect to refer to our particle sizes by the average values as determined from a Scherrer broadening analysis. We summarize this data in Table 2.5.

Table 2.5: Size estimates from Scherrer-broadening and TEM and effects on the coercivity trends for pressed powders. Note that TEM provides a particle size distribution (and error bars on the average particle size), whereas x-ray diffraction measures an average particle size and does not yield error bars.

d_{XRD} (nm)	d_{TEM} (nm)	H_C (300 K) (Oe)	H_C (5 K) (Oe)	M_R/M_S (300 K)	M_R/M_S (5 K)	T_B (K)
5.0	5.8 ±0.7	0	17320	0	0.79	245
7.1	7.8 ±0.9	0	17290	0	0.81	257
10.4	15.6 ±2.7	210	16600	0.13	0.80	>300 K
14.0	15.6 ±2.6	300	13800	0.19	0.82	>300 K

Magnetic Properties

The magnetic hysteresis loops for pressed powder samples were measured by a superconducting quantum interference device, and coercivity was extracted from the loop width. The 300 K hysteresis loops for pressed powder samples of the 5 and 7

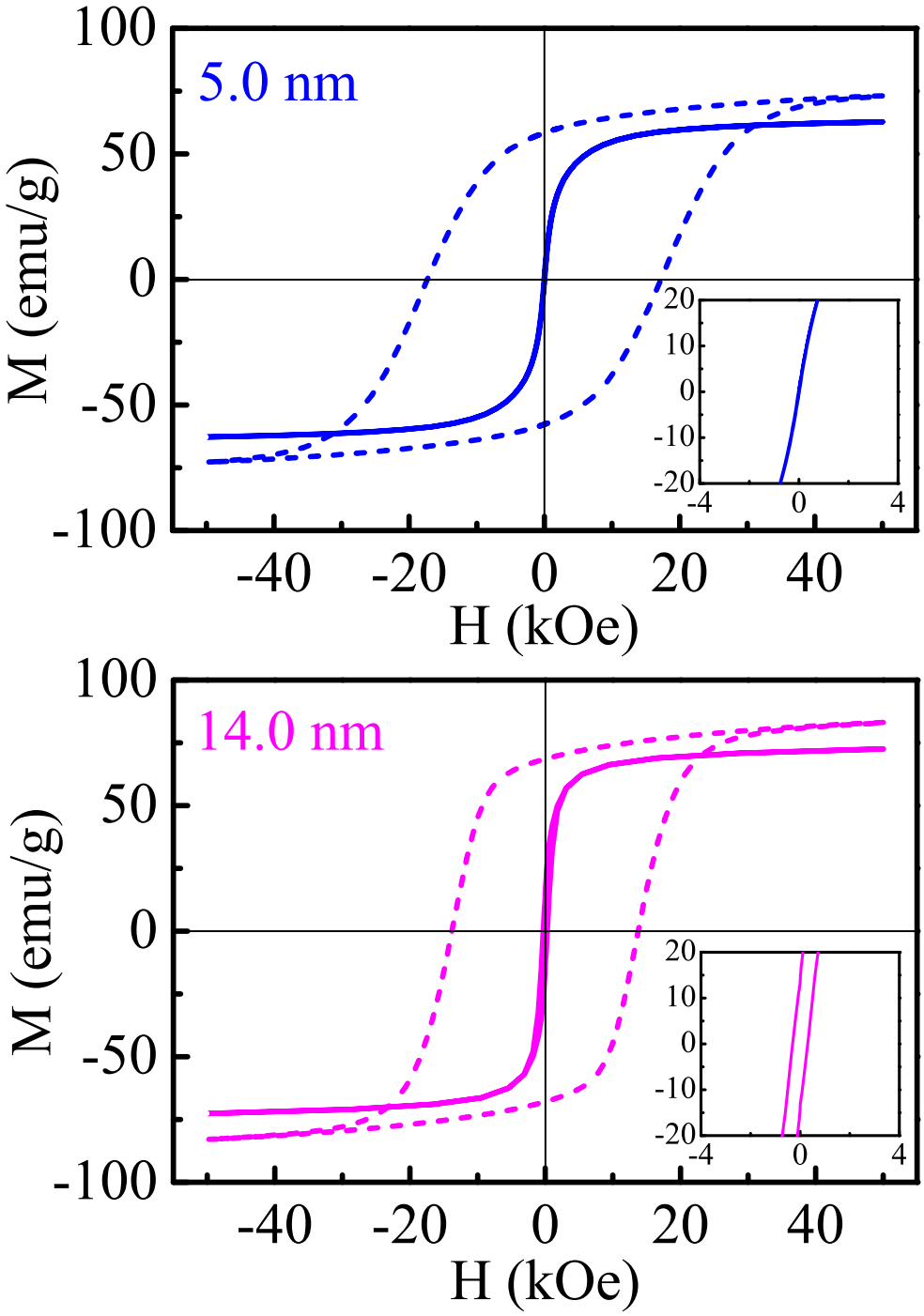

Figure 2.14: 5 K (dashed line) and 300 K (solid line) hysteresis loops for 5 and 14 nm $CoFe_2O_4$ nanoparticles. [5]

nm $CoFe_2O_4$ nanoparticles are shown in Figure 2.14 and the associated insets. The nanoparticles show a lower coercivity at 300 K compared to bulk $CoFe_2O_4$, which is about 980 Oe. [130] Table 2.5 shows the coercivities are 0, 0, 210, and 300 Oe for 5.0, 7.1, 10.4, and 14.0 nm particles, respectively, which indicates the superparamagnetic state of 5 and 7 nm particles. The reduced remanence M_R/M_S, obtained from saturation magnetization M_S and remanence M_R, usually depends on the symmetry of the easy axis and the orientation of the easy axis with respect to the applied field. The reduced remanence M_R/M_S (Table 2.5) also confirms the superparamagnetic state for these two small sizes of nanoparticles.

Figure 2.14 also shows a comparison of the 5 K hysteresis loops for pressed powder samples of the two end members. As indicated in Table 2.5, coercivities are far from zero, and even the smallest particles have a very high coercivity. With increasing particle size, H_C has a step and then decreases. The obtained values of M_R/M_S are close to the theoretical value of 0.83 for particles with cubic anisotropy and a randomly oriented cubic easy axis. [131–133]

Zero-field cooled (dashed line) and field-cooled (solid line) magnetization of the 5 and 14 nm $CoFe_2O_4$ nanoparticles are shown in Fig. 2.15. The blocking temperature, T_B, is 245 K for the 5 nm particles, but it is larger than 300 K for the 14 nm particles. Table 2.5 summarizes the magnetic parameters for the four different sizes of $CoFe_2O_4$ nanoparticles. These findings are in line with previous studies of the blocking temperature. [132]

Sample Preparation and Vibrational Spectroscopy

Nanoparticles were synthesized as discussed in the previous section. Nanoparticles with sizes between approximately 5 and 14 nm were shown in Fig. 2.13. All of the $CoFe_2O_4$ nanoparticles of interest here are single-domain. [134] For comparison, bulk

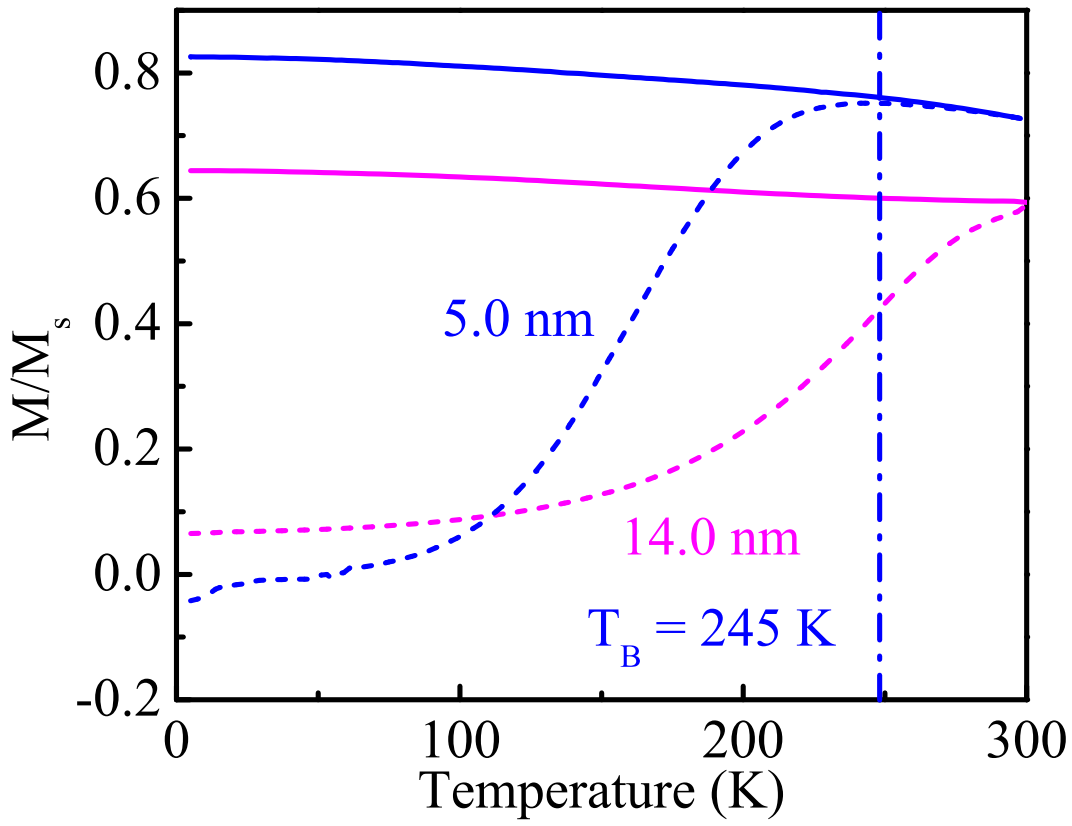

Figure 2.15: Zero-field cooled (dashed line) and field-cooled (solid line) magnetization curves for 5 and 14 nm $CoFe_2O_4$ nanoparticles, with a field of 1000 Oe. $T_B = 245$ K for the 5 nm particles and is above 300 K for the 14 nm sample. [5]

$CoFe_2O_4$ powder (99.31%) was purchased directly from Alfa Aesar. [135, 136] Here, the crystallites are 0.1 mm diameter on average.

For our spectroscopic work, the bulk powder and nanoparticles were mixed with paraffin ($\sim$3 mass percent) to form isotropic composites. Transmittance was measured using a Bruker 113V Fourier transform infrared spectrometer (20 - 5000 cm^{-1}; 0.5 cm^{-1} resolution) at room temperature. A helium-cooled bolometer detector was employed for added sensitivity. The absorption coefficient was obtained as $\alpha(\omega) = -\frac{1}{hd} lnT(\omega)$, where h is the loading, d is the thickness, and $T(\omega)$ is the measured transmittance. Low temperature experiments were carried out with an open flow cryostat. Traditional peak fitting techniques were employed as appropriate.

Chapter 3

Literature Survey

As the extent of a solid is reduced to nanoscale dimensions, the physical, magnetic, electrical, and optical properties can be dramatically altered. Many groups have a strong interest in size-shape control of properties and reactivities that depend on an intimate coupling with the lattice. One challenge is to understand exactly how the microscopic aspects of chemical bonding should be quantified in nanomaterials. Another challenge is to understand the signatures of the spin-phonon coupling in nanoscale materials. Model compounds, such as layered MoS_2, antiferromagnetic MnO, and ferrimagnetic $CoFe_2O_4$, bring the opportunities to investigate these interesting phenomenons in nanoscale materials. In this chapter, I will review some of the most interesting problems in these three materials. I will also review the current approaches of the charge and bonding analysis, and the magneto-elastic coupling analysis.

3.1 MoS_2

MoS_2 is a well-known transition metal dichalcogenide because of its two-dimensional physical and electronic structure, and its excellent modern tribological properties.

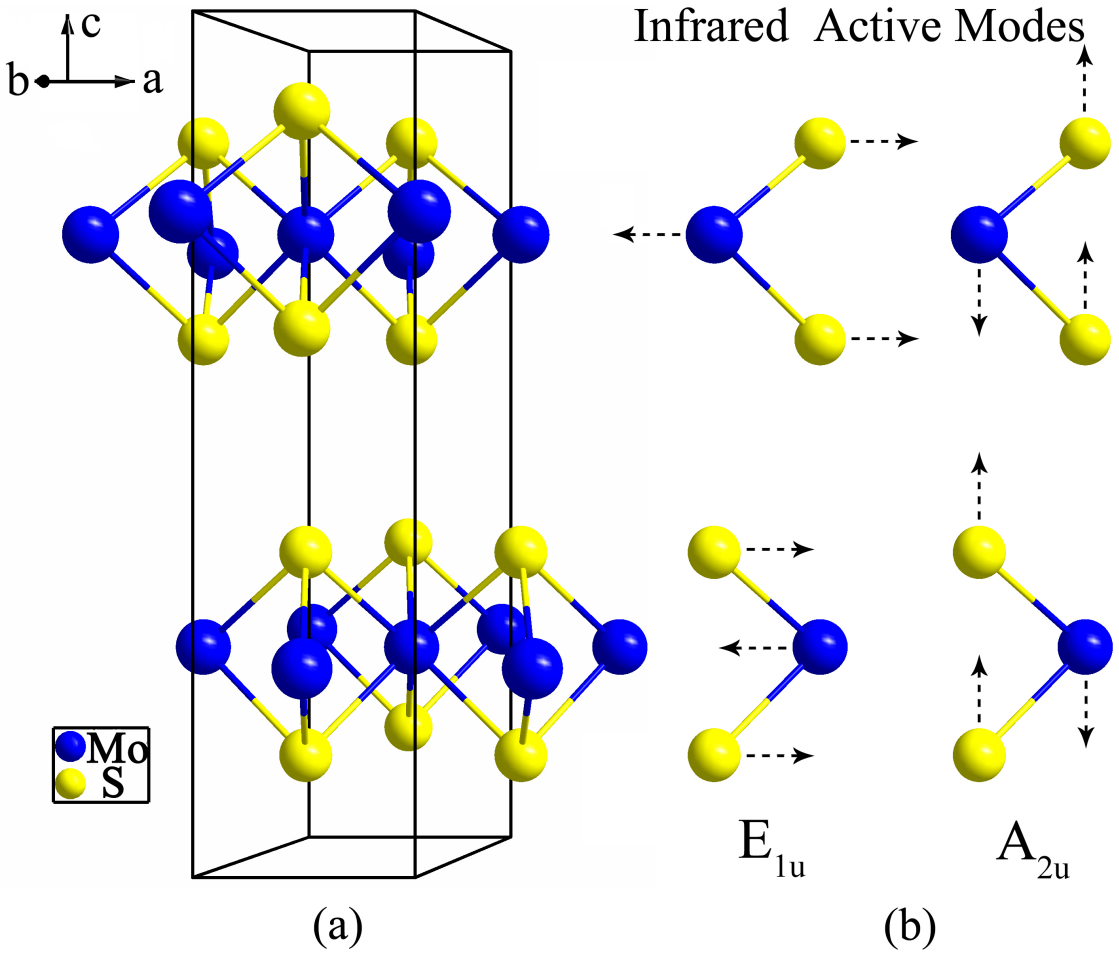

Figure 3.1: Crystal structure [137] and displacement patterns of infrared active E_{1u} and A_{2u} vibrational modes [138] in 2H-MoS_2. [1]

[42, 43, 45] The structure of 2H-MoS_2 belongs to the $P6_3/mmc$ space group. [137] The atomic centers (six per primitive cell) are arranged in sheets parallel to the base of the hexagonal unit cell (Fig. 3.1(a)). One consequence of this architecture is the low-dimensional electronic structure which consists of strong bonding in the *ab* plane and weak van der Waals interactions between layers. [138] Each MoS_2 slab contains a layer of metal centers, sandwiched between two chalcogen layers, with each metal atom bonded to six chalcogen atoms in a trigonal prismatic arrangement (D_{3h} local symmetry). MoS_2 is a semiconductor with indirect and direct band gaps of 1.23 and 1.74 eV. [139] Since the optical band gaps are well-matched to the solar spectrum, these materials are used for electrodes in high efficiency photoelectrochemical cells and phototransistors. [140, 141]

Group theory predicts 18 vibrational modes: $2A_{2u} + 2E_{1u} + A_{1g} + E_{1g} + 2E_{2g} + 2B_{1g} + B_{2u} + E_{2u}$. [138, 142] Displacement vectors of the two infrared active E_{1u} and A_{2u} modes are shown in Fig. 3.1(b). Lattice vibrations in MoS_2 have been studied by measuring the infrared reflectance and Raman scattering from single crystals. [13–15] Layered MoS_2 had been studied as a prototype for foundational studies of charge and bonding in the late 1970's. [13–15] Figure 3.2 displays two infrared active E_{1u} and A_{2u} modes that are sensitive to charge and bonding in the intralayer and interlayer directions, respectively. Using the classical oscillator fitting technique, Wieting *et al.* found optical-phonon frequencies and optical constants for single crystal (Table 3.1) which have been used to assess Born effective charges (Z_B^*) in molybdenum dichalcogenides. [14] For 2H-MoS_2 single crystals, $Z_B^* \approx$ 1.1 - 1.2 e in the intralayer direction (e is the electronic charge), making it one of the more covalent systems. [13, 14]

The discovery of inorganic fullerene-like (IF) nanostructure establishes a new paradigm in the chemistry of nanomaterials and leads to the birth of a new field

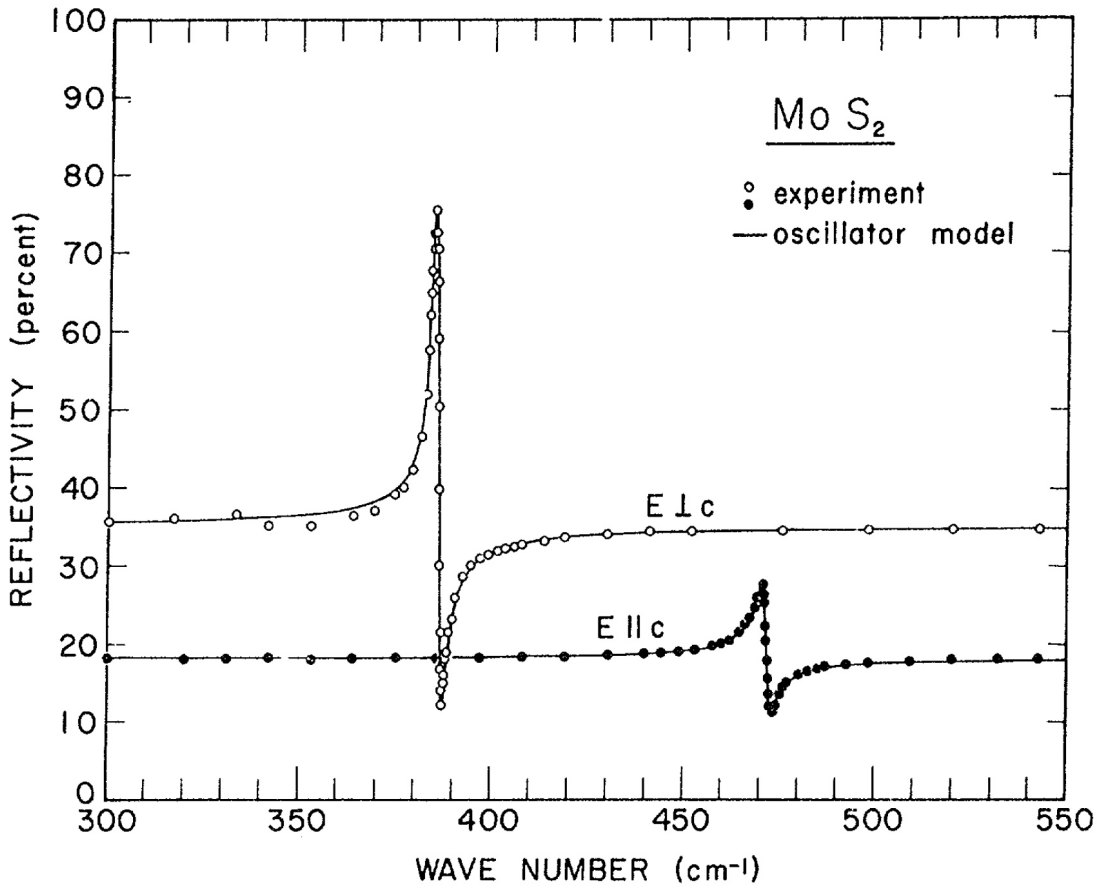

Figure 3.2: Reflectance of 2H-MoS_2 at room temperature for $E \perp c$, and $E \parallel c$. The solid curves are generated by means of the parameters of Table 3.1 and represent best fits to the reflectivity data. [13]

Table 3.1: Classical-oscillator parameters and optical-phonon frequencies (ω) for the infrared-active modes in 2H-MoS_2. [13] S is the oscillator strength, γ is the damping constant, $\varepsilon_1(\infty)$ is the high frequency dielectric constant, ω_{TO} is the transverse optical phonon frequency, ω_{LO} is the longitudinal optic phonon frequency, Z_B^* is the Born effective charge, and Z^* is the local effective charge.

Polarization direction	S	γ	$\varepsilon_1(\infty)$	ω_{TO} (cm^{-1})	ω_{LO} (cm^{-1})	Z_B^* (e)	Z^* (e)
$E \perp c$	0.016±0.001	0.0025±0.0002	15.2±0.2	384±1	387±1	1.11	0.15
$E \parallel c$	0.0024±0.0002	0.005±0.0005	6.2±0.1	470±1	472±1	0.52	0.37

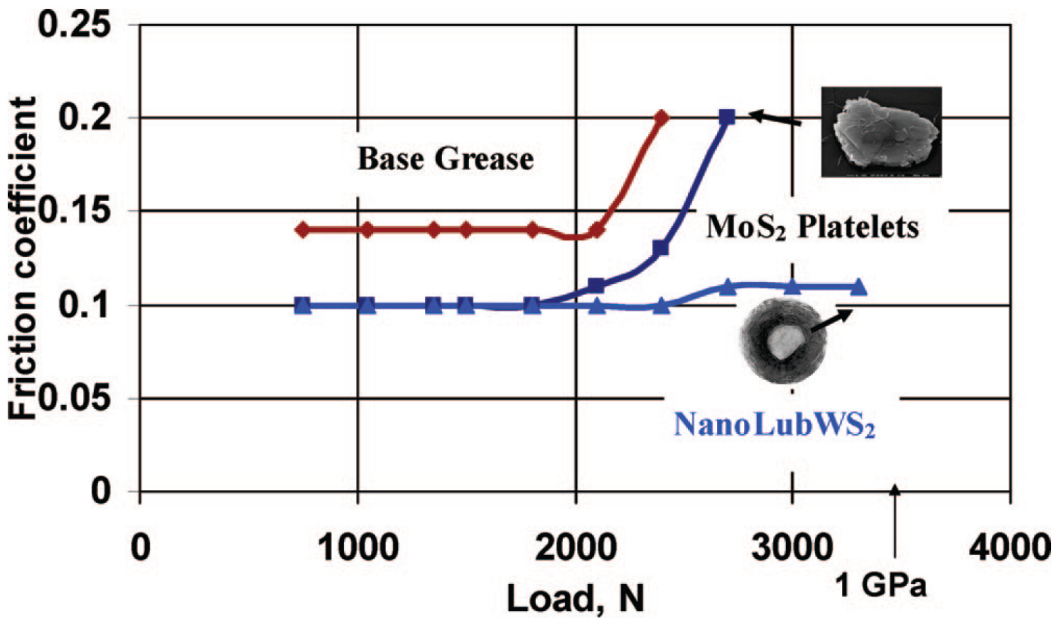

Figure 3.3: Friction coefficient as function of load. [9]

of inorganic chemistry, which opened up vast opportunities for the synthesis and study of new kinds of nanostructures. [29, 30] The properties of IF nanomaterials differ significantly from the corresponding bulk material. This idea motivated our detailed analysis of lattice dynamics of IF-MoS_2 nanoparticles compared to its parent compound. The structure of IF-MoS_2 nanoparticles is similar to that of the nested fullerenes (Fig. 2.7). X-ray diffraction demonstrates that the bulk 2H- structure is locally preserved within the nanoparticle, albeit with a $\sim$2% c-axis expansion. [143–145] We therefore anticipate that the vibrational properties of IF- and 2H-MoS_2 will display similarities befitting their common chemistry, symmetry, and structure and, at the same time, display important differences that derive from confinement, broken translational symmetry, strain, and subtle curvature. [142,147] The connection between charge, structure, and mechanical and tribological properties is still an open question in the IF-materials. Recent theoretical work indicates that the substantially reduced friction coefficient from 0.3 to 0.1 under high load conditions (Fig. 3.3) has its origins in the local coating processes that take place during particle (or tube) breakup. [9, 148–153] These breakup processes seem to begin in the inner, most highly strained layer of the nanomaterial. [9, 148–153] Rhenium-doped inorganic fullerene-like MoS_2 nanoparticles exhibit super tribological behavior because the doped nanoparticles are negatively charged at their surface eliciting mutual repulsion. Extensive tribological measurements with these poly-alpha-olefin oils formulated with 1 wt % of the doped IF-nanoparticles showed friction coefficients as low as 0.01 in mixed lubrication conditions and negligible wear. [149, 150]

3.2 MnO

MnO is a prototype for foundational studies of structure, correlated electron behavior, chemical bonding, and magnetism. [26, 74, 102, 105, 106, 154] Bulk MnO displays

a $Fm\bar{3}m$ rocksalt structure with a 4.4448 Å lattice constant at 300 K (left-hand image, Fig. 3.4(a)). [154] Group theory predicts only one triply-degenerate infrared

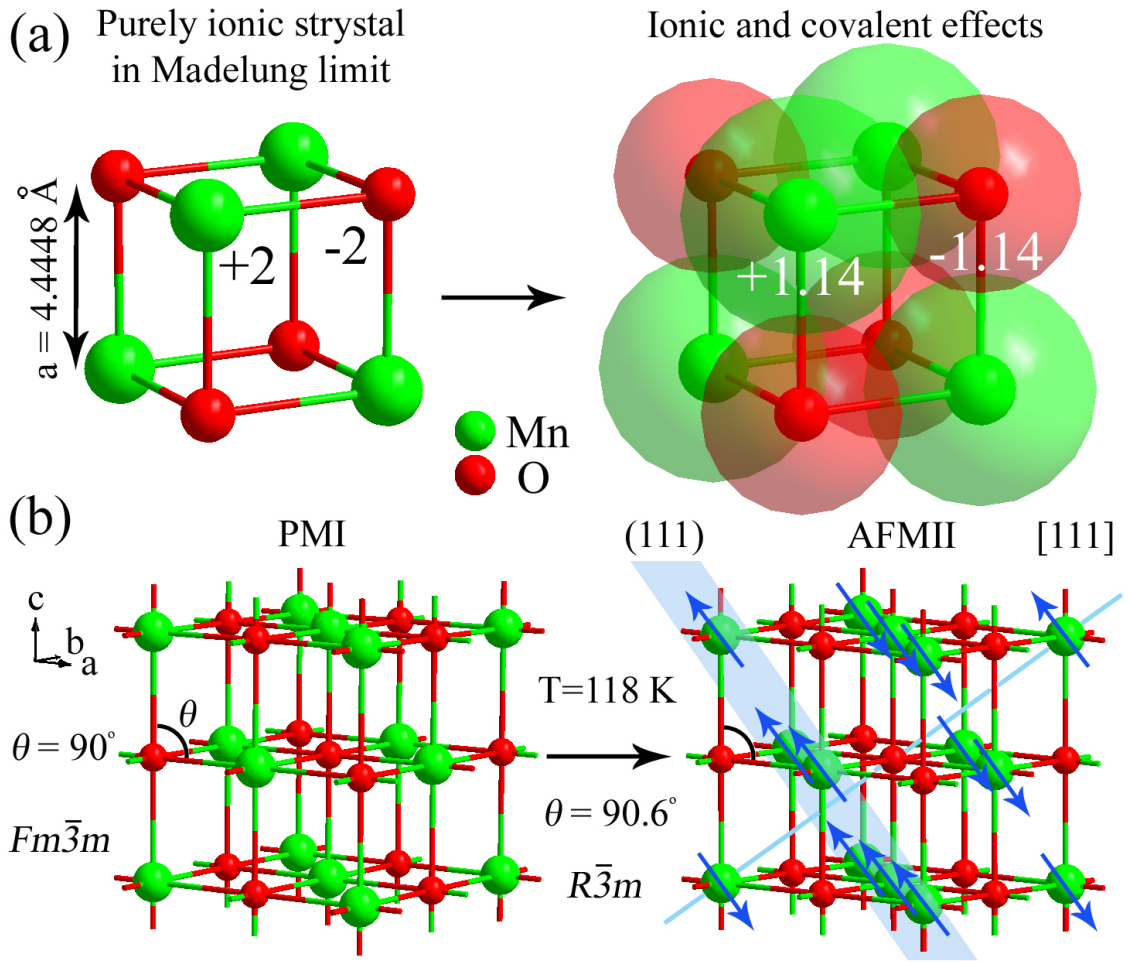

Figure 3.4: (a) Left: Schematic view of an ideal ionic crystal of MnO made up of +2 and -2 ions. Right: Schematic view of a more realistic MnO crystal. Here, local effective charge (ionicity) is given by +1.14 and -1.14 ions. [3] The transparent regimes schematically indicate electron clouds (total polarizability) that are shared by the involved atoms, with electron density concentrated in the regions between atomic centers. Born effective charge includes the combined effects of the local effective charge and total polarizability. (b) Left: 300 K cubic crystal structure. Right: Low temperature rhombohedral crystal structure with AFMII magnetic arrangement. Spins are aligned in the (111) plane, and the planes are stacked antiferromagnetically in the [111] direction. [4]

active vibration mode. [28] Previous infrared investigations focused on analysis of the Restrahlen band (Fig. 3.6), its anharmonic character, and evaluation of Born and local (Szigeti) effective charges for the Mn center (Z_B^* = 2.2 - 2.6 e, Z^* = 1.08 e). [16–19, 23, 24, 156] Here, e is the electronic charge. These literature values show that even in a highly ionic material like MnO, the system is far from the Madelung limit. As shown schematically in the right-hand image of Fig. 3.4(a), Born effective charge contains both local and nonlocal contributions that are represented by local effective charge and total polarizability. [3]

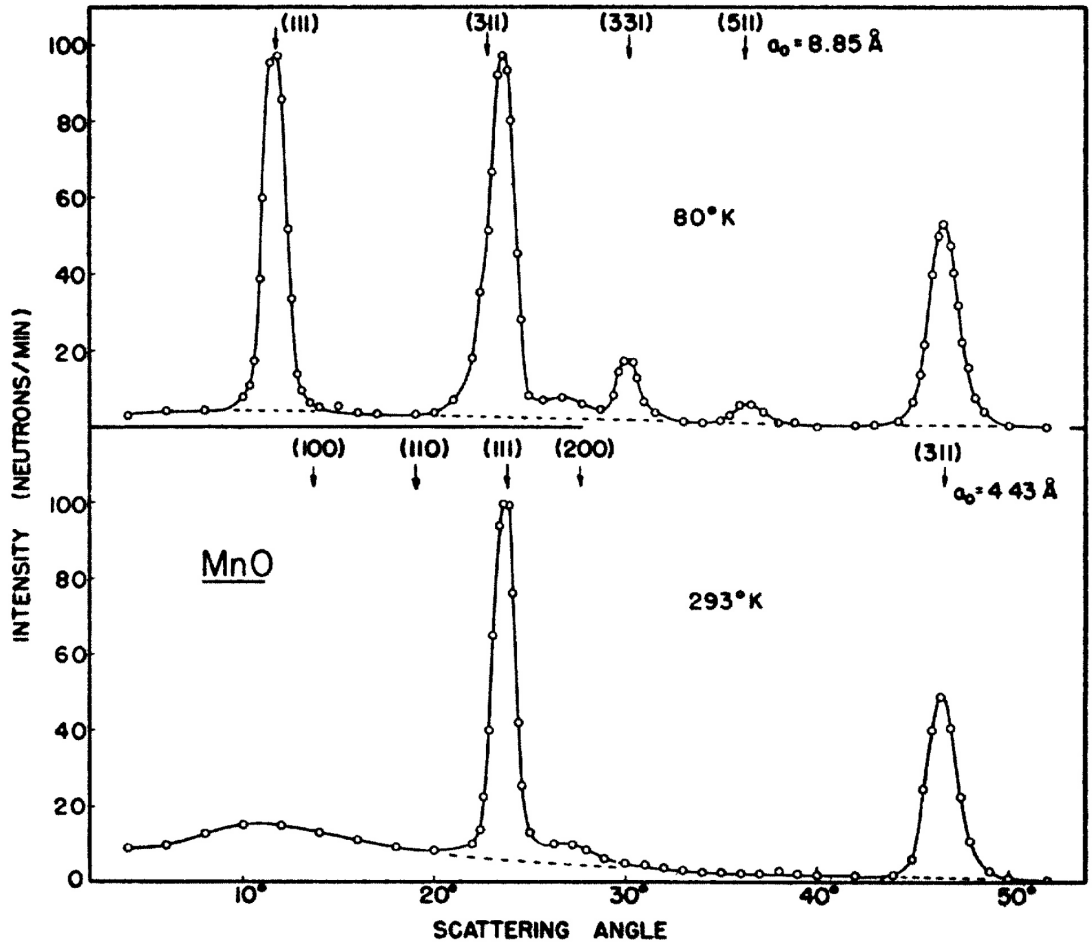

Figure 3.5: Neutron diffraction patterns for MnO taken at liquid nitrogen and room temperatures. Four extra antiferromagnetic rejections are to be noticed in the low temperature pattern. [155]

At 118 K, MnO undergoes a transition from a strongly correlated paramagnetic insulator (PMI) to a type-II antiferromagnet (AFMII). [74,102,105] Figure 3.5 shows a classical magnetic structure determination of MnO by the neutron diffraction. At 80 K there are extra netron reflections not present at 293 K. That means the magnetic moments of the Mn^{2+} ions are ordered in a nonferromagnetic arrangement. Further analysis indicates spins in a single (111) plane are parallel, but the adjacent (111) planes stacked antiferromagnetically in the [111] direction (Fig. 3.4(b)). [74,105,106] The Néel transition is accompanied by a rhombohedral distortion (Fig. 3.4(b)), evidenced in the lattice constants by exchange striction [106] and the infrared spectrum

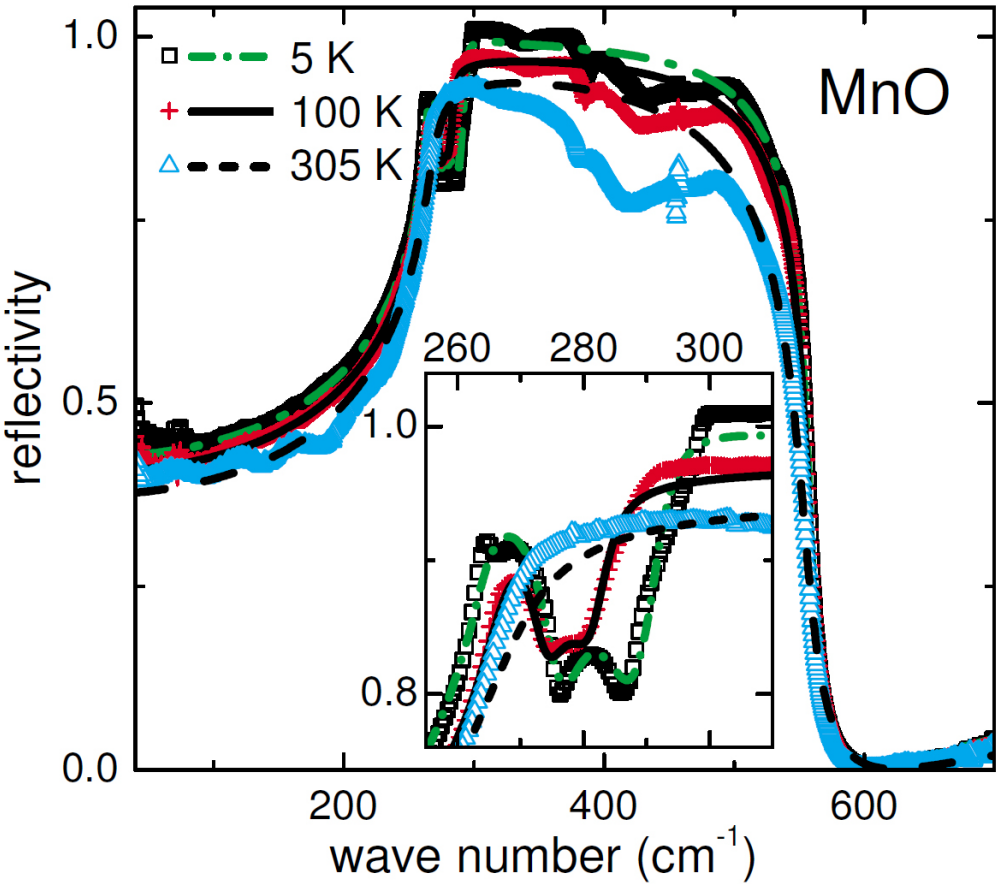

Figure 3.6: Variable temperature reflectance spectra of MnO at 5 K, 100 K, and 305 K. The lines are results of fits based on a generalized oscillator model. The inset shows the splitting of the phonon mode below T_N. [18]

as magnetic ordering-induced phonon splitting. [18] Figure 3.6 displays the variable temperature reflectance of single crystalline MnO. The clear mode splitting below 118 K in the single crystal is easily interpreted as evidence for the rhombohedral distortion in the AFMII phase (Fig. 3.4(b)) . [18, 102, 157]

Magnetic oxide nanoparticles are important systems for the understanding of magnetic properties in a confined size regime [7, 31] and several technical applications, ranging from magnetic resonance imaging, drug delivery, battery materials, catalysts, and nanoelectronic materials. [31–36, 118] Major findings at this time include synthetic techniques that yield excellent size/shape control and the possibility of ferromagnetism (or an uncompensated ferromagnetic surface) at small particle sizes. [31–36, 118] Realizing a significant difference between nanoscale MnO and its parent compound, the recent discovery of analogous nanoscale MnO is driving our research on the microscopic aspects of charge-boding and spin-phonon coupling in combination with finite length scale effects. Figures 3.7(a) and (b) show the temperature evolution of the $(\frac{1}{2}\frac{1}{2}\frac{1}{2})$ magnetic Bragg peak for 13 nm MnO nanoparticles. Wang *et. al.* concluded that nanoparticles have reduced average magnetic moment compared to the bulk and a core-shell structure with a surface layer which does not contribute significantly to the magnetic order. [93] To test charge-boding and spin-phonon coupling analysis, we elected to work with MnO, a chemically and structurally simple salt for which both bulk and nanoscale analogs are available. Our selection of MnO was further motivated by the fact that this binary oxide is the parent compound for many functional materials such as colossal magnetoresistant manganites, [26] making evaluation of size effects highly attractive.

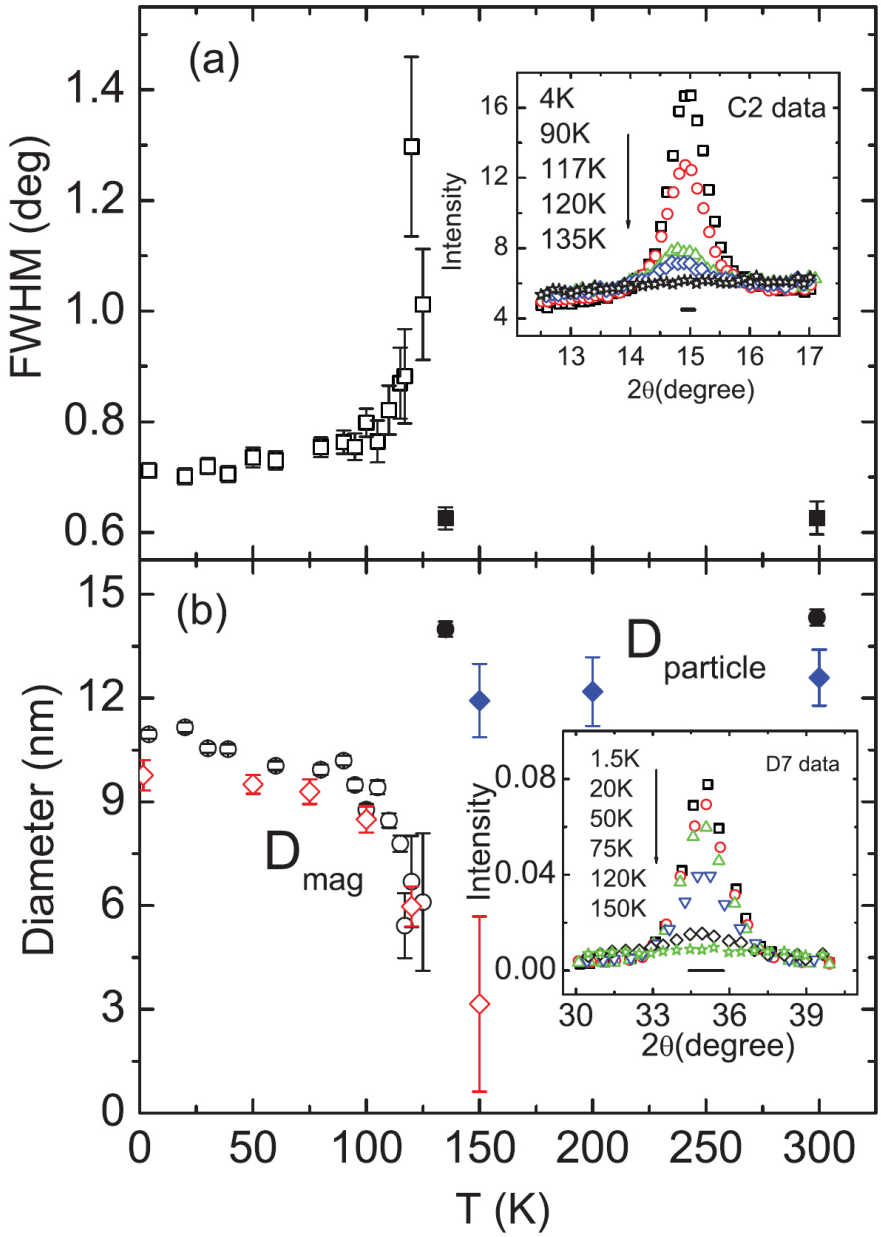

Figure 3.7: (a) $(\frac{1}{2}\frac{1}{2}\frac{1}{2})$ magnetic peak width (open symbols) and the (111) nuclear peak width (solid symbols) for 13 nm MnO nanoparticles. Inset is the $(\frac{1}{2}\frac{1}{2}\frac{1}{2})$ peak at different temperatures. The data were collected on the C2 instrument. (b) The temperature dependent magnetic domain size (open symbols) and particle size (solid symbols) for 13 nm MnO nanoparticles. Circles are unpolarized results from C2 and diamonds are polarized results from D7. Inset is the evolution of the $(\frac{1}{2}\frac{1}{2}\frac{1}{2})$ magnetic peak with temperature from the D7 polarized neutron scattering data. Horizontal bars in the insets represent the instrumental resolution. [93]

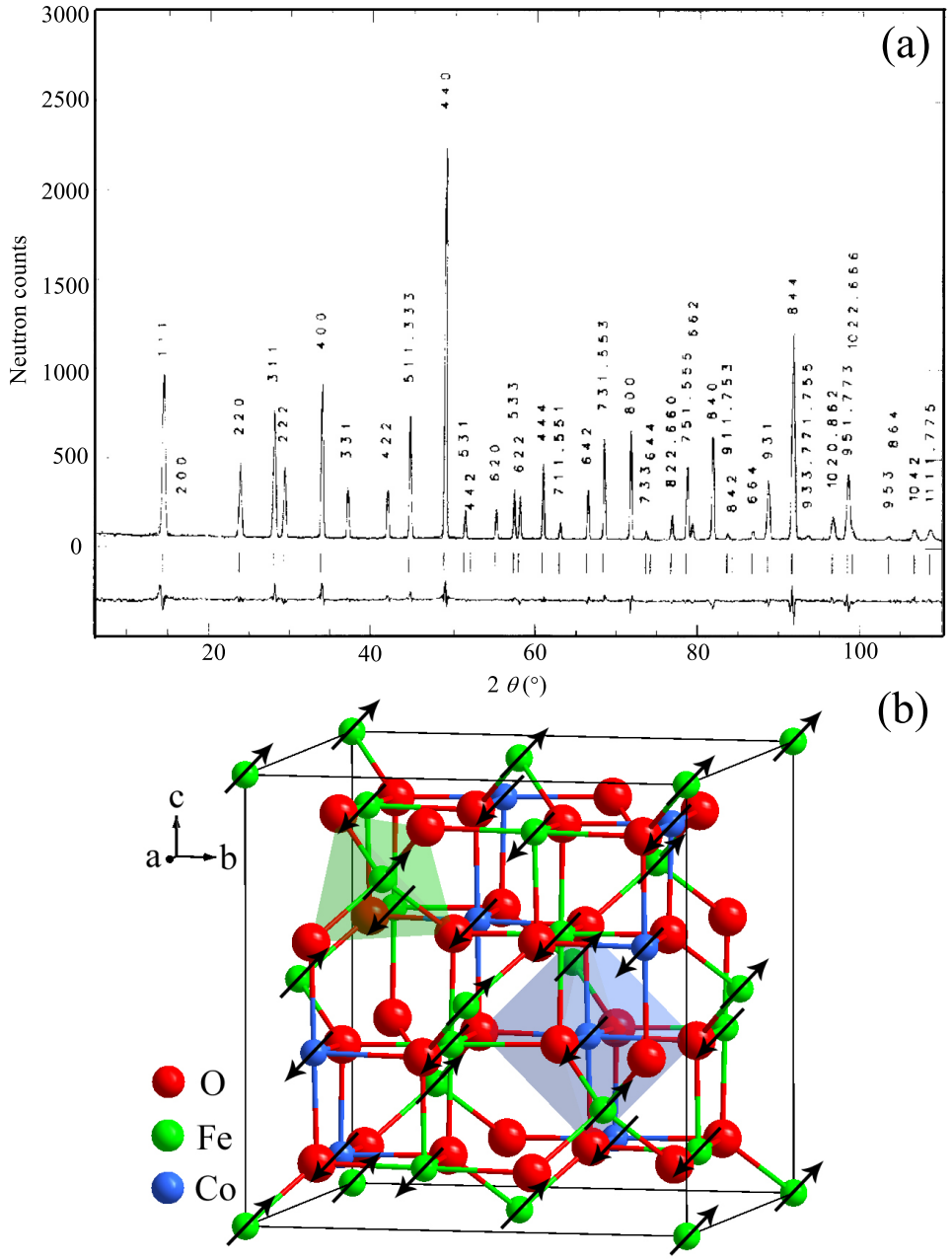

Figure 3.8: (a) $CoFe_2O_4$ neutron diffraction data (λ = 1.2268 Å) at T = 5 K. The dots are the experimental values; the upper line is the calculated diagram; the continuous line below is, at the same scale, the difference between observed and calculated values. Vertical bars indicate $2\theta_{hkl}$ positions (hkl are all either even or odd). [103] (b) 300 K crystal structure of $CoFe_2O_4$ spinel with ferrimagnetic ordering along the [100] direction. [5]

3.3 $CoFe_2O_4$

Spinel ferrites are prototypes for foundational studies of magnetism and structure because of its high Curie temperature and cubic structure. [26, 104, 158] $CoFe_2O_4$ is also a candidate for high-density recording because of its magnetic properties, good mechanical hardness, and chemical stability. [26, 103, 158, 159] $CoFe_2O_4$ crystallizes in an inverse spinel structure with the general formula AB_2O_4 where A and B denote tetrahedral and octahedral cation sites in a close-packed oxygen environment. [103, 159] The unit cell is cubic (a = 0.8391 nm at 300 K) with 8 formula units and a $Fd\bar{3}m$ space group (Fig. 3.8(b)). [103, 104, 159] Group theory predicts four triply-degenerate (T_{1u}) infrared-active vibrational modes. [160] Figure 3.9 shows two strong phonons in the 300 K infrared absorption spectra of $CoFe_2O_4$. Waldron assigned the

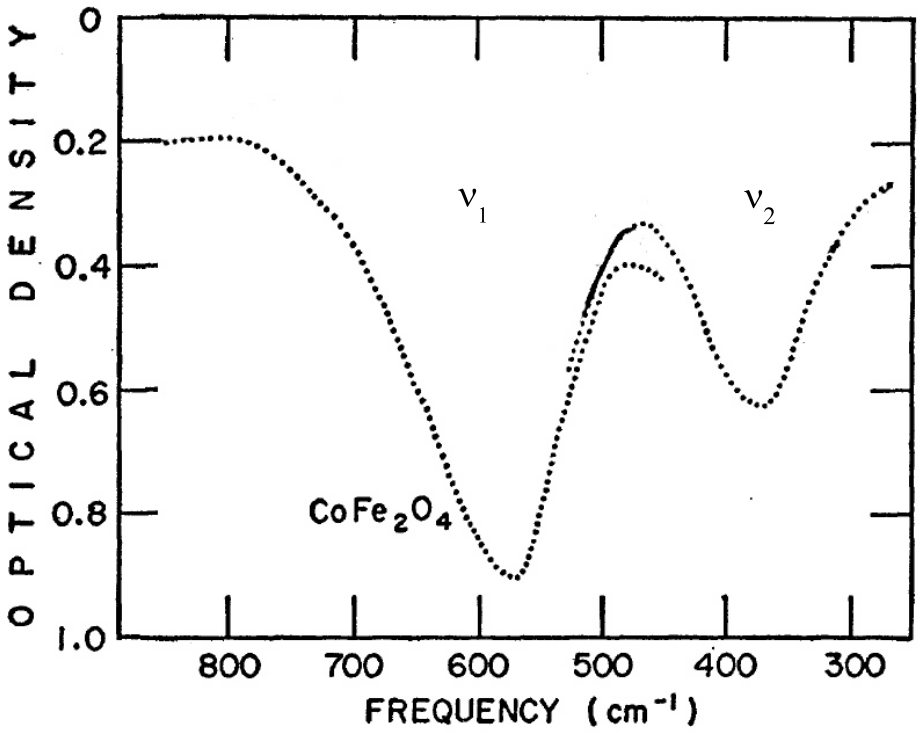

Figure 3.9: 300 K infrared absorption spectra of $CoFe_2O_4$. Optical density measured relative to standard KBr disk. Multiple lines indicate alternate runs or prism changes. [104]

high-frequency phonon to ν_1 and the low-frequency phonon to ν_2. [104] For ν_1, the tetrahedral metal centers vibrate against the oxygen cage, and the octahedral metal centers vibrate against each other and the surrounding oxygen sites. For ν_2, the tetrahedral metal center is fixed and oxygen cage vibration is balanced by octahedral cation + cage motion. Here, the octahedral metal center vibrates against the other B site cation and the surrounding oxygen centers. Several authors have analyzed the lattice dynamics of the AB_2O_4 system and compared their findings with infrared and Raman data. This work revealed mode assignments, displacement patterns, charge and bonding information, and thermodynamics. [104, 160]

Below the 860 K Curie temperature (T_C), neutron diffraction shows that $CoFe_2O_4$ presents long range collinear ferrimagnetic order with antiferromagnetic inter-sublattice

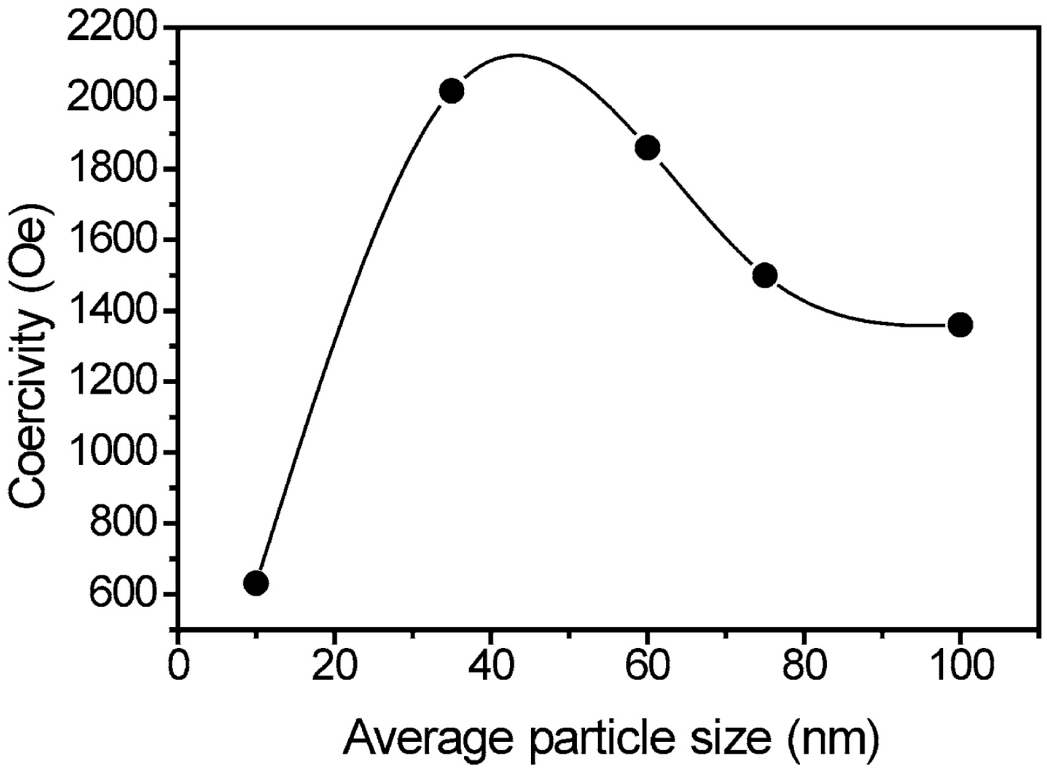

Figure 3.10: The relationship between the average particle size and the coercivity of $CoFe_2O_4$ at 300 K (the continuous line is guide to the eye). [162]

exchange interactions (Fig. 3.8(a)). Local canting and anisotropy reduces the moment to $3.35\mu_B$ at 300 K, and the easy magnetization axis is along [100]. [103] Figure 3.8(b) shows the schematic view of ferrimagnetic ordering in $CoFe_2O_4$. The magnetic moments of the cations in the tetrahedral and octahedral sites are aligned parallel with respect to one another (ferromagnetic coupling). Between the different crystallographic sites the arrangement is antiparallel (antiferromagnetic coupling). As there are twice as many octahedral sites as tetrahedral sites, there is a net moment of spins yielding ferrimagnetic ordering for the crystal.

The discovery of nanoscale $CoFe_2O_4$ enables investigation of finite length scale effects. Major findings at this time include synthetic techniques that yield excellent

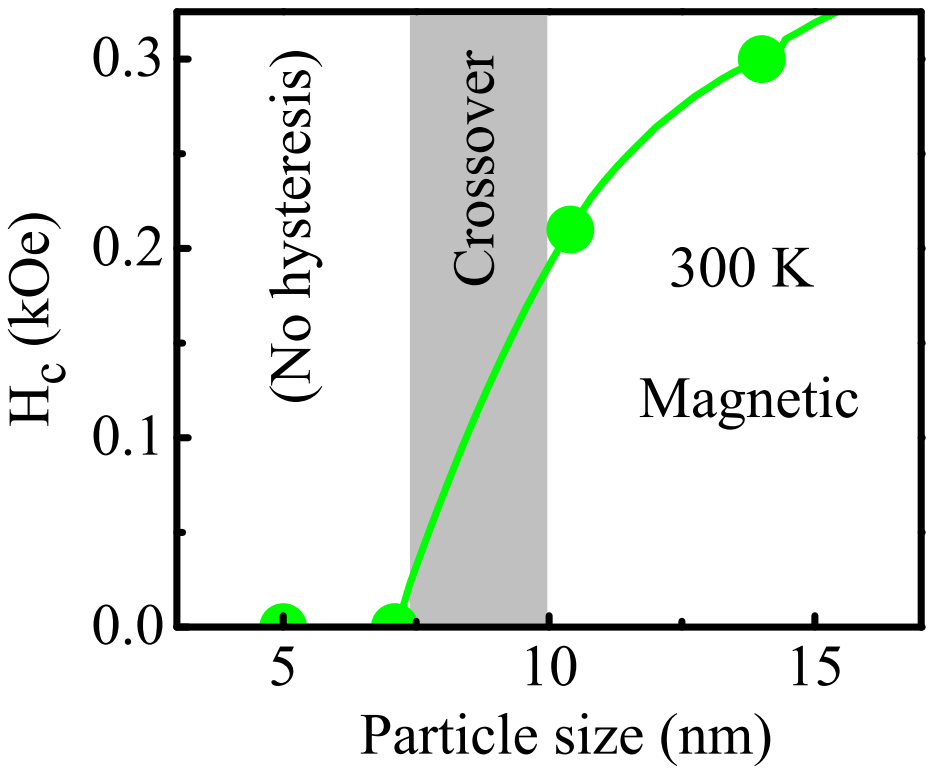

Figure 3.11: Surface-to-volume ratio and coercivity as a function of particle diameter. The magnetic crossover regime (from the hysteretic ferrimagnetic regime at large sizes to the superparamagnetic state at small particle sizes) is denoted by the vertical gray band. The green line connecting coercivity data points guides the eye. [5]

size/shape control, [100, 125, 134, 161] the crossover to single domain behavior at ∼40 nm, [134,162] the cubic anisotropy, [131–133] and superparamagnetism in small particles. [100, 134, 161, 163, 164] As a magnetic insulator, [159] nanoscale $CoFe_2O_4$ is attractive for device applications, such as high-density magnetic storage media. [26,97–99,158] Figure 3.10 displays the relationship between the average particle size and coercivity. The coercivity first increases as the particle size decreases, reaches a maximum value of 2020 Oe at ∼40 nm and then decreases for the decrease in particle size. [134,162] As the particle size further decreases, Birkel *et al.* found that there is clearly a size-driven crossover between the hysteretic and non-hysteretic ($H_c = 0$) regimes in the 7 - 10 nm size range (Fig. 3.11). Below the magnetic crossover, $CoFe_2O_4$ nanoparticles are in the superparamagnetic state. [5] Realizing the interesting magnetic properties of $CoFe_2O_4$ nanoparticles, we therefore anticipate that their vibrational properties will display similarities with MnO [4] through the spin-lattice interaction. $CoFe_2O_4$ attracted our attention as a rich system with which to explore these developments because (i) coupling in a magnetic oxide is anticipated to be large [68, 75, 86] and (ii) confinement effects [4, 107–109] can be explored.

3.4 Charge and Bonding Analysis

Born and local (or ionic) effective charges are well-known quantities with which to assess chemical bonding and polarization in a material. [27,165] A large local effective charge indicates a highly ionic system (for instance, 0.8 e in NaCl), a medium-sized value points toward an intermediate bonding case (0.4 e in GaAs), and a small value is associated with a covalent material (0 e in Si). [7, 8] On the other hand, Born effective charge describes the static and dynamic polarizations. [27] From the optical properties point of view, large longitudinal-optic-transverse-optic (LO-TO) splittings are well-known characteristics of polarizable compounds and associated with substan-

tial Born effective charges. This is because LO-TO splitting is directly proportional to charge within Born's original formalism (Eq. 4.2). [10, 11, 27, 166, 167] Using the LO-TO splitting and high frequency dielectric constant, it is relatively straightforward to quantify chemical bonding from optical measurements of high-quality single-crystal samples and compare the extracted value(s) with first-principles calculations. [113, 167, 168] For example, Born effective charge for the Mn center in MnO (Z_B^* = 2.2 - 2.6 e) [16, 17] agrees well with the theoretical calculations. [19, 23, 24] The key issue for the estimate of Born effective charge is the determination of LO-TO splittings using optical measurements on single crystals. Unfortunately, there are many instances when single crystals of a bulk material are unavailable, either because they cannot be grown or are not of sufficient size or quality for optical measurements. At the same time, nanoparticles, nanotubes, and alloys (or composite mixtures) present scientifically compelling problems, [46, 47, 169–171] where optical measurements on powdered materials are the only option, a drawback that complicates the situation but does not diminish the desirability of obtaining quantitative Born and local effective charge data. Following Born and Szigeti, [27, 165] we developed an application of the Lorentz model in which fits to vibrational spectra or a Kramers Kronig analysis are employed along with several useful formalisms (Eqs. 2.38, 2.39a, and 2.39b) to quantify microscopic charge in unoriented (powdered) materials, assuming that the effects of ionic displacement and atomic polarizability are superimposable. We demonstrate that this technique can be used to assess chemical bonding and local strain under certain conditions, a development that advances the field of nanoscience and, at the same time, retains many attractive features of optical spectroscopy and the traditional Lorentz model in Chapters 4 and 5.

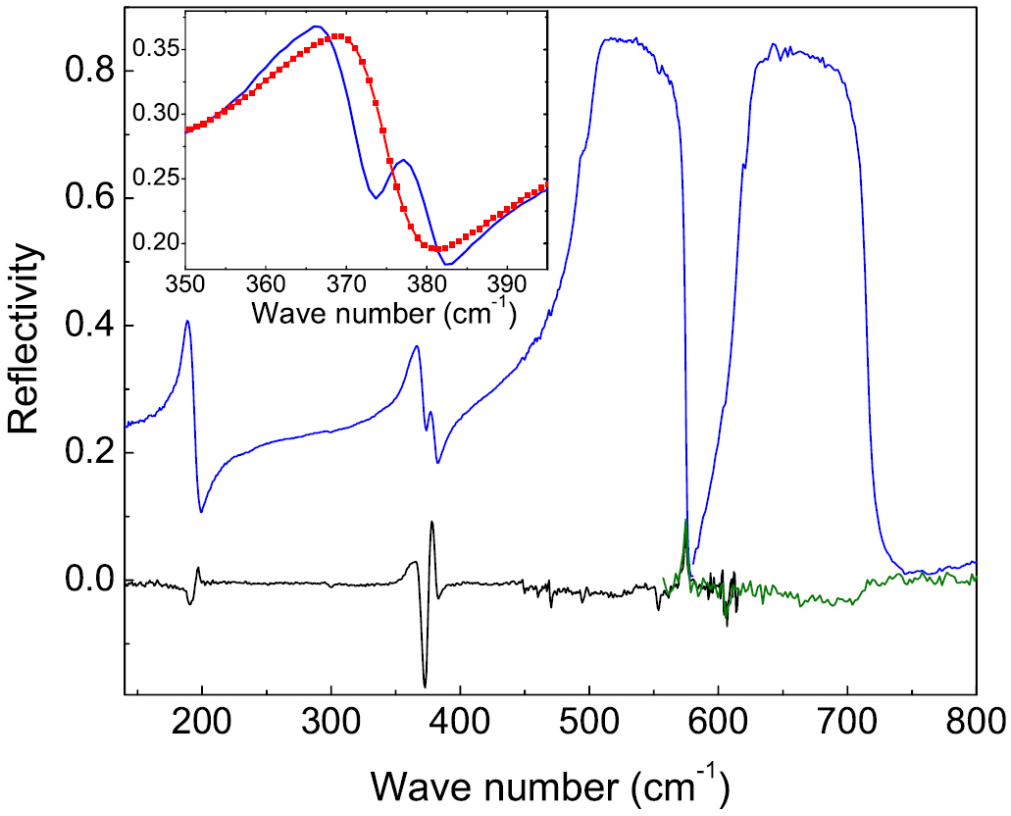

Figure 3.12: Top curve: Reflectance spectrum (R_{LT}) of $ZnCr_2O_4$ single crystal in the low-temperature phase; bottom curve: $2(R_{LT} - R_{HT})$; inset: R_{LT} and R_{HT} (line + symbols) in a narrow range. [75]

3.5 Spin-Phonon Coupling Analysis

The interplay between spin and lattice becomes important as materials are in the magnetic state because it give rise to an amazing variety of phenomena, including the spin-Teller and the magnetoelectric effects. [26, 56–59] The major goal of the spin-phonon coupling analysis is to estimate the influence of magnetic order on phonons. [60–68] A description of spin-phonon coupling in oxides has been one of the major challenges of the past several decades. [18, 67, 68, 74, 75, 89]

The spin-phonon coupling mechanism can be understood by the equations of motion of ions as materials are in the magnetic state. The Hamiltonian for the ion motion is written as $H = p^2/2\mu + V(u)$. Here, $V(u)$ is the effective potential, u

is the displacement, p is the translational momentum, and μ is the reduced mass. When the atomic centers in a unit cell vibrate, the exchange interactions become a function of the displacement, and spin-spin interaction changes the effective phonon potential. This generic mechanism couples spin to the lattice as [67, 68, 73, 74]

$$\omega^2 = \omega_0^2 + \lambda \langle S_i \cdot S_j \rangle, \tag{3.1}$$

where $\omega = \sqrt{k/\mu}$ is the perturbed mode frequency (in the presence of spin-spin interactions, k is the spring constant), ω_0 is the bare phonon frequency without spin-spin interactions, $\lambda = \frac{1}{\mu} \cdot J''$ is the macroscopic spin-phonon coupling constant, J is the magnetic exchange, J'' is second derivative with respect to u, and $\langle S_i \cdot S_j \rangle$ is the nearest-neighbor spin-spin correlation function. Here, we employ a single J Hamiltonian, where the exchange interaction is negative (positive) for antiferromagnetic (ferromagnetic) interactions. In Eq. 3.1, magnetic exchange J is thus a function of ion displacement. We can expand J in a Taylor series as $J = J(u_0) + J'(u_0)(u-u_0) + \frac{J''(u_0)}{2}(u-u_0)^2 + \cdots$. Here, u is the displacement, u_0 is the equilibrium position, $J(u_0) < 0$ for antiferromagnetic, $J(u_0) > 0$ for ferromagnetic, and $J'(u_0) = 0$ at equilibrium. [172] For a system with dominant antiferromagnetic interactions, $\langle S_i \cdot S_j \rangle$ will be negative. Because the frequency ω is related to the spring constant k as $\omega = \sqrt{k/\mu}$ (μ is the reduced mass), the macroscopic spin-phonon coupling constant $\lambda = \frac{1}{\mu} \cdot J''(u_0)$. A strong anharmonic effect of the magnetic exchange J indicates a large spin-phonon coupling constant. For example, $ZnCr_2O_4$ has $\lambda = 6.2$ cm^{-1}, [75] but MnF_2 has $\lambda = 0.3$ cm^{-1}. [73] This model predicts that a triply degenerate vibrational mode in a two-sublattice ferrimagnetic cubic environment (as exists in a system like MnO) will split into two branches below T_C. [4, 74, 211, 212]

Spin-orbit interaction is a well-known phenomenon that manifests itself in lifting the degeneracy of one-electron energy levels in solids. The Hamiltonian of the spin-

orbit coupling is given as: $\Delta H = \beta S \cdot L$, [7] where β is the spin-orbit coupling constant, S is the spin angular momentum, and L is the angular momentum. [7, 8] Spin-orbit coupling is the origin of magneto-elastic coupling because the spin-orbit coupling in general tends to modify the energy balance and in particular the exchange energy. [7,8] Thus, the spin-orbit interaction contribute to the spin-phonon coupling constant, λ, through the exchange interaction.

Spectroscopists often employ a well-known shorthand formula to describe spin-phonon coupling, [68, 73, 75]

$$\omega = \omega_0 + \lambda' \langle S_i \cdot S_j \rangle. \tag{3.2}$$

Here, $\lambda' = 2J''/(\mu\omega_0)$. For example, using spectroscopic results (Fig. 3.12) and the value of the spin-spin correlation function derived from the specific-heat data of Martinho *et al.*, [173] Sushkov *et al.* found $\lambda = 6.2$ cm^{-1} for $ZnCr_2O_4$ single crystal. Fennie *et al.* present an approach to predict the influence of magnetic order on optical phonons from first principles and apply this approach to the strongly geometrically frustrated spinel zinc chromite. [68] They extracted $\lambda = 11$ cm^{-1}, which agrees with experimental result. [75] This value is similar to couplings for many frustrated oxides like Mn_3O_4, $DyMn_2O_5$, $Co_3V_2O_8$, $Ni_3V_2O_8$, and $CuGeO_3$. [70–72, 174, 175]

As discussed above, most of the interesting investigations on spin-phonon coupling are related to single crystals. It has been much less explored in confined systems. [90–93] The discovery of nanomaterials is driving our research on the microscopic aspects of spin-phonon coupling in combination with finite length scale effects. MnO and $CoFe_2O_4$ attracted our attention as a classic magnetic oxide with important displacement effects and because they are available in both single crystalline and nanoscale form. The well-known magnetic structures of these two materials provide a good opportunity to investigate spin-phonon coupling

Chapter 4

Dynamical Charge and Structural Strain in Inorganic Fullerene-Like MoS_2 Nanoparticles

4.1 Vibrational Spectra of 2H- and IF-MoS_2

Figure 4.1 shows a close-up view of the far infrared reflectance spectra of 2H- and IF-MoS_2 at 300 K. Two vibrational modes are observed, in agreement with group theory predictions. [138, 142] We assign the peak at 384 cm^{-1} to the E_{1u} optical mode and the feature near 468 cm^{-1} to the A_{2u} optical mode. These spectral features probe intralayer and interlayer dynamics, respectively. The observed band positions are in reasonable agreement with previous single crystal data [13] and similar pressed pellet results on bulk and nanoscale WS_2 (with appropriate mass correction). [142] The character of the E_{1u} and A_{2u} modes is strikingly different in the two materials. In IF-MoS_2, the E_{1u} mode is damped and suppressed compared to the 2H- analog, whereas the A_{2u} mode is slightly more pronounced in the IF- compound compared

to that in the bulk. These differences can be quantified using classical dielectric oscillator models and fitting techniques. [15, 177]

We employed classical Lorentz models to fit the reflectance spectra of 2H- and IF-MoS_2 with a complex dielectric constant $\varepsilon(\omega) = \varepsilon_1(\omega) + i\varepsilon_2(\omega)$ constructed as a superposition of Lorentzian oscillators as: [15, 177]

$$\varepsilon(\omega) = \sum_j \frac{S_j \omega_{TO,j}^2}{(\omega_{TO,j}^2 - \omega^2) - i\gamma_j \omega} + \varepsilon_1(\infty). \tag{4.1}$$

Here, S is the oscillator strength, ω_{TO} is the transverse optical phonon frequency, γ is the damping constant, $\varepsilon_1(\infty)$ is the high frequency dielectric constant, and j is the mode index. Good quality fits were obtained using a total of two oscillators, as shown in Fig. 4.1. This data is summarized in Table 4.1 as a set of "observed parameters", where the observed oscillator strength and dielectric constant are actually tabulated as $\overline{S}$ and $\overline{\varepsilon}_1(\infty)$ to distinguish these powder averages from the density- and distribution-corrected values discussed later. From these fits, we calculated the optical constants of 2H- and IF-MoS_2. Optical constants can also be calculated with a Kramers-Kronig analysis.

4.2 Born Effective Charges of 2H- and IF-MoS_2

The rigid ion model [10, 113] gives a precise relationship between the longitudinal and transverse optic phonon frequencies (often called the LO-TO splitting) [178] and Born effective charge:

$$4\pi^2 c^2 \sum_j (\omega_{LO,j}^2 - \omega_{TO,j}^2) = \frac{Ne^2}{\epsilon_0 \varepsilon_1(\infty) V} \sum_k \frac{(Z_B^*)_k^2}{m_k}. \tag{4.2}$$

Here, $\omega_{LO,j}$ is the longitudinal optic phonon frequency for the j-th oscillator, Z_{Bk}^* is Born effective charge on the k-th ion, N is the number of formula units in the

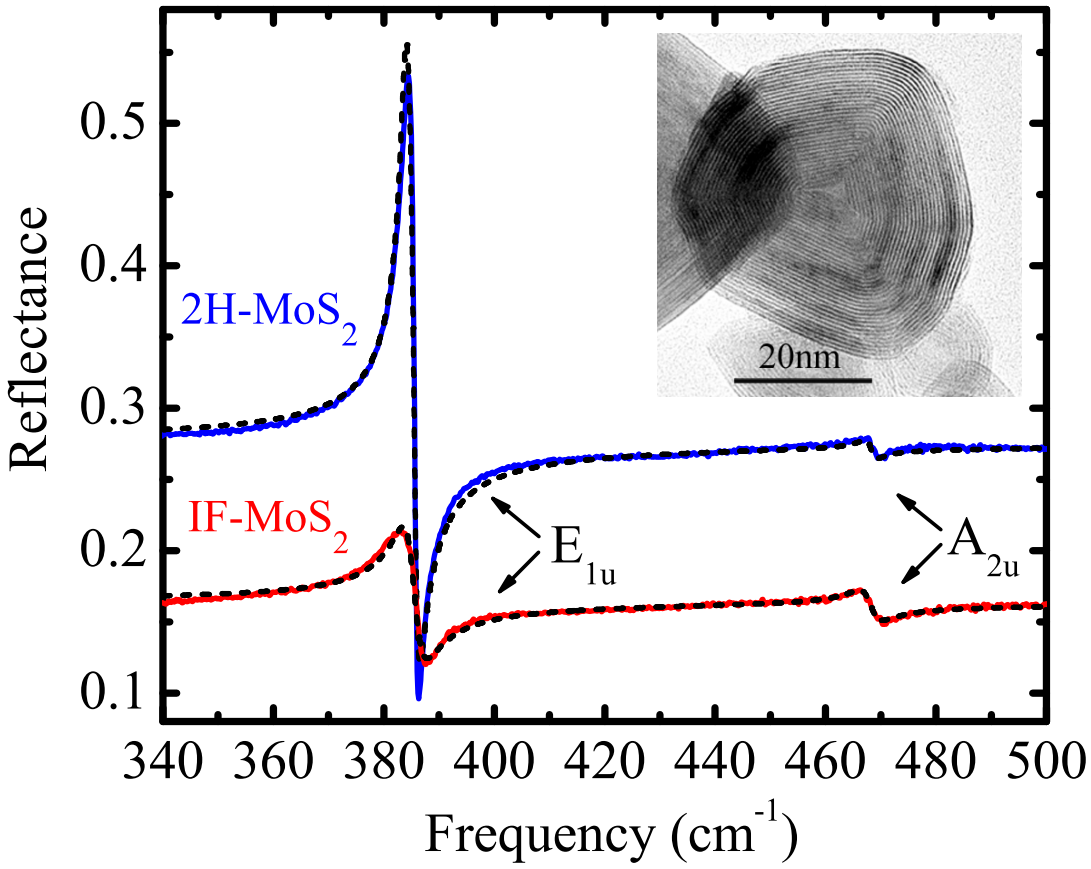

Figure 4.1: Close-up view of the 300 K reflectance spectra of bulk and nanoscale MoS_2. Blue and red curves: experimental data for the 2H- and IF-MoS_2 samples, respectively. Black dashed lines: theoretical fits as described in the text. Inset: high resolution transmission electron microscopy image of IF-MoS_2 showing the lattice fringing and curvature in the nanoparticles. The layer-to-layer distance is 0.62 nm. [1]

unit cell, V is the volume of the MoS_2 formula unit, m_k is the atomic mass of the k-th atom, ϵ_0 is the permittivity of free space, e is the electronic charge, and c is the speed of light. The sum rule, $\sum Z^*_{B,k} = 0$, guarantees that the charge neutrality condition is fulfilled. In other words, the sum of Born effective charges for all atoms in the unit cell must vanish, element by element. [114] Unfortunately, Eqn. (4.2) is valid only when the LO-TO splitting of a single crystal sample is known. Thus, it is not well-suited for assessing charge and bonding in nanomaterials as the latter are often in powder form. We can finesse this problem by employing oscillator strength changes rather than LO-TO splitting, as described below. This procedure allows us to calculate pseudo-Born effective charges for both 2H- and IF-MoS_2. These values can be compared with the known Born effective charge in the 2H-single crystal (Z^*_B $\approx$ 1.1 - 1.2 e in the intralayer direction [13, 14]), providing an effective check for our method.

Equation (4.1) and the generalized Lyddane-Sachs-Teller relationship [8] provide a way forward by articulating the relationship between dielectric constant, oscillator strength and the LO-TO splitting: $\varepsilon_1(\infty)\cdot(\omega^2_{LO,j} - \omega^2_{TO,j}) = \omega^2_{TO,j}\cdot S_j$. [2] Substituting this result into Eqn. (4.2), we see that Born effective charge can also be calculated mode by mode from the knowledge of oscillator strength:

$$4\pi^2 c^2 \sum_j \omega^2_{TO,j} S_j = \frac{N e^2}{\epsilon_0 V} \sum_k \frac{(Z^*_B)^2_k}{m_k}. \tag{4.3}$$

This rendering is well-suited to the analysis of nanomaterials and will be employed in this work to evaluate charge and bonding in IF-MoS_2 nanoparticles.

Before presenting the results of this analysis for the nanoparticles, we briefly point out that the dynamical charge values extracted from our analysis of 2H-MoS_2 pressed pellet sample are in good agreement with single crystal results from the literature. [13,14] This agreement provides confidence that the formulation presented

Table 4.1: Observed and scaled parameters extracted from our oscillator fitting analysis of the measured reflectance spectra of 2H- and IF-MoS_2. [1]

Material	Mode	$\overline{S}_j{}^b$ $\cdot 10^{-3}$	$\overline{\varepsilon}_1(\infty)^b$	S_j $\cdot 10^{-3}$	$\varepsilon_1(\infty)$	$\omega_{TO,j}$ (cm^{-1})
2H-MoS_2 (Crystal)	E_{1u}			200^a	15.2^a	384^a
	A_{2u}			30^a	6.2^a	470^a
2H-MoS_2 (Powder)	E_{1u}	114	10.3	200^c	15.2^c	383.7^b
	A_{2u}	3.6		30^c	6.2^c	468.2^b
IF-MoS_2 (Powder)	E_{1u}	36	5.6	77^c	8.3^c	384.6^b
	A_{2u}	6.7		29^c	6.2^c	467.9^b

[a] Single crystal data from Wieting's resutls. [13].
[b] Observed parameters extracted from our oscillator fitting analysis of the measured reflectance spectra (Fig. 4.1).
[c] Effective oscillator strength and dielectric constant obtained by correcting the observed powder data for density and orientational averaging.

in Eqn. (4.3) can be extended in a powerful way to include nanomaterials. That the sample is in powder form presents two main challenges: (i) the pressed pellet density is less than that of the corresponding single crystal thus underestimating the intrinsic oscillator strength of each infrared active vibrational mode, and (ii) the spatial distribution of the dipole moment operator in a powder sample is not that of a single crystal, an effect that also works to misrepresent oscillator strength. The density correction merely scales the observed oscillator strength toward its intrinsic value. The spatial distribution correction is more complex. This is because, in some samples, there may be a random orientation (like the nanoparticles in this work). In other samples, for instance 2H-MoS_2, the orientation correction must account for the preferential surface orientation of the platelets in a pressed pellet sample. Here's

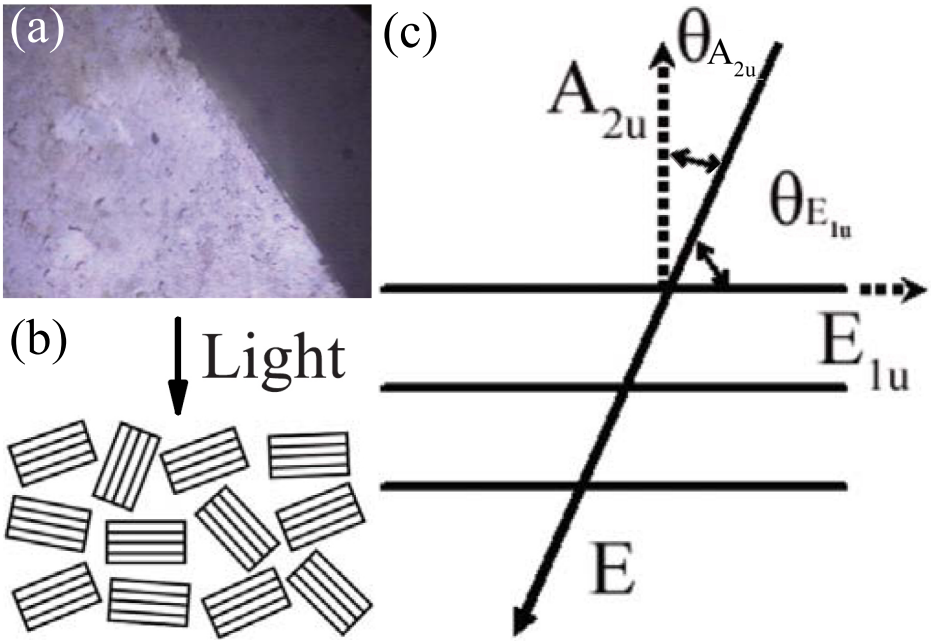

Figure 4.2: (a) Photo of a typical pressed pellet sample. (b) Schematic view of the 2H-MoS2 platelets in a pressed pellet sample. (c) Diagram for tilted oscillators. Note that, $\theta_{A_{2u}} = \frac{\pi}{2} - \theta_{E_{1u}}$. [2]

how it works. When an oscillator has an angle θ with respect to the macroscopic field E, the observed oscillator strength ($\overline{S}$) will be reduced compared to its intrinsic value (S). Employing both Eqn. (4.1) and the definition of electric displacement ($D = \epsilon_0 E + P = \varepsilon(\omega)\epsilon_0 E$), three useful expressions can be obtained which capture and compensate for the inherent orientational aspects in MoS_2 or any similar two-dimensional material in powder form: [2]

$$\overline{S}_{E_{1u}} = S_{E_{1u}}\langle\cos^2(\theta_{E_{1u}})\rangle v \tag{4.4a}$$

$$\overline{S}_{A_{2u}} = S_{A_{2u}}\langle\cos^2(\theta_{A_{2u}})\rangle v \tag{4.4b}$$

$$\begin{aligned}\overline{\varepsilon}_1(\infty) &= 1 + [\varepsilon_{1,E_{1u}}(\infty) - 1]\langle\cos^2(\theta_{E_{1u}})\rangle v \\ &+ [\varepsilon_{1,A_{2u}}(\infty) - 1]\langle\cos^2(\theta_{A_{2u}}\rangle v.\end{aligned} \tag{4.4c}$$

Here, v is the relative density of a powdered vs. single crystalline sample. In this work, $v = 0.70$. [115] Figure 4.2(a) shows a photo of a typical pressed pellet sample. We can imagine a schematic view of the 2H-MoS2 platelet (Fig. 4.2(b)) because the small crystals in the the pellet are unoriented. Each small crystal will have a polarization angle, θ, with the electric field, E (Fig. 4.2(c)). From Eqns. (4.4a) and (4.4b), it may appear that both $\langle\cos^2(\theta_{E_{1u}})\rangle$ and $\langle\cos^2(\theta_{A_{2u}})\rangle$ are unknown. However, in the 2H- material, the two modes in question are orthogonal. Thus, $\theta_{E_{1u}} + \theta_{A_{2u}} = \frac{\pi}{2}$ and $\langle\cos^2(\theta_{E_{1u}})\rangle + \langle\cos^2(\theta_{A_{2u}})\rangle = 1$. Thus, there is really only one unknown. We can find the value of $\langle\cos^2(\theta_{E_{1u}})\rangle$ by comparison with Wieting's 2H-MoS_2 single crystal data. [13] As shown in Table 4.1, $S_{E_{1u}} = 0.20$, $S_{A_{2u}} = 0.03$, $\varepsilon_{1,E_{1u}}(\infty) = 15.2$, and $\varepsilon_{1,A_{2u}}(\infty) = 6.2$. These parameters ought to be applicable to a powder sample as long as surface effects are not too important. As discussed previously, fits to our powder data yielded $\overline{S}_{E_{1u}} = 0.114$, $\overline{S}_{A_{2u}} = 0.0036$, and $\overline{\varepsilon}_1(\infty) = 10.3$ (Table 4.1). Working backwards with Eqns. (4.4a) and (4.4b), we extract independent estimates of $\langle\cos^2(\theta_{E_{1u}})\rangle$ from analysis of the E_{1u} and A_{2u} modes as 0.81 and 0.83, respectively. [179,180] Using Eqn. (4.4c) and an average value of $\langle\cos^2(\theta_{E_{1u}})\rangle = 0.82$, we extract $\overline{\varepsilon}_1(\infty) = 9.8$, consistent with that obtained by direct fitting techniques ($\overline{\varepsilon}_1(\infty) = 10.3$). Finally, we employ Eqn. (4.3) and the aforementioned effective parameters to calculate the Born effective charges. We find $Z_B^* = 1.11$ and 0.52 e,

in the intralayer and interlayer directions, respectively. This analysis shows that the optical constants of 2H- powder and single crystalline [13,14] samples are identical, as they should be, once density and orientational effects are taken into account. It also demonstrates that the approach outlined here can be reliably extended to analyze nanomaterials.

We can carry out the same analysis for the nanoparticles. Table 4.1 displays the results of our fit to the powder spectra for IF-MoS_2. Using this data ($\overline{S}_{E_{1u}} = 0.036$, $\overline{S}_{A_{2u}} = 0.0067$, and $\overline{\varepsilon}_1(\infty) = 5.6$), we evaluate the important quantities as discussed above. Assuming spherical nanoparticles [181] we obtain $\langle \cos^2(\theta_{E_{1u}}) \rangle = \int (\sin^3\theta) \mathrm{d}\theta = \frac{2}{3}$ and $\langle \cos^2(\theta_{A_{2u}}) \rangle = \int (\cos^2\theta) \sin\theta \mathrm{d}\theta = \frac{1}{3}$. Inserting these values into Eqns. (4.4a) and (4.4b), we find $S_{E_{1u}} = 0.077$ and $S_{A_{2u}} = 0.029$. As before, a density factor of 0.70 has been applied to account for the reduced density of the pressed pellet sample. Using Eqn. (4.3) and these effective parameters, we calculate the Born effective charges for the infrared active phonon modes of IF-MoS_2. We find $Z_B^* = 0.69\ e$ in the intralayer direction, significantly less than that obtained for the 2H- material. In the interlayer direction, we extract $Z_B^* = 0.52\ e$, identical to that obtained for the layered bulk.

These results are summarized in Table 4.2. In the intralayer direction, the Born effective charge of the Mo center decreases from 1.11 in the bulk material to 0.69 in the nanoparticles. In the interlayer direction, Z_B^* is unchanged ($\sim$0.52 e) within our sensitivity. The origin of these trends is discussed below.

Table 4.2: Effective charges and other parameters of 2H- and IF-MoS_2 in the two principle directions. [1]

Mode	Material	Z_B^* (e)	$\varepsilon_1(\infty)$	n	α (Å^3)	Z^* (e)	k (N/m)
E_{1u}	2H	**1.11**	15.2	0.461	**100**	**0.15**	338
	IF	**0.69**	8.3	0.462	**91**	**0.16**	338
A_{2u}	2H	**0.52**	6.2	0.078	**200**	**0.37**	497
	IF	**0.52**	6.2	0.076	**200**	**0.37**	497

4.3 Local Effective Charges and Polarizabilities of 2H- and IF-MoS_2

The vibrational response of 2H- and IF-MoS_2 (Fig. 4.1) can be also used to extract information about structural strain in the nanoparticles and elucidate the consequences for bonding, polarizability, local, and non-local effective charge. In an ionic solid, we need to consider the so-called depolarization field, which originates from the influence of neighboring ions. The polarization, $P = \frac{N}{V}(Z^*x + \alpha E_{eff})$, has two parts. The first contribution is due to the relative displacements of ions. The second results from electron cloud distortion around the polarizable ionic centers due to the macroscopic electric field E. Here, Z^* is the local effective charge (or dynamic ionic charge), α is the polarizability in one direction of the unit cell, E_{eff} is the microscopic electric field ($E_{eff} = E + \frac{\eta}{\epsilon_0}P$), η is the depolarization factor, and P is the polarization. [27, 112] Using these relationships, we can evaluate local effective charges and polarizabilites for both materials as: [2]

$$Z_B^* = \frac{Z^*}{1 - \eta\frac{N\alpha}{V}} \tag{4.5a}$$

$$\varepsilon_1(\infty) = 1 + \frac{\frac{N\alpha}{V}}{1 - \eta\frac{N\alpha}{V}}. \tag{4.5b}$$

These equations provide a more comprehensive definition of local effective charge compared to earlier presentations by Uchida *et al.* [14] and Lucovsky *et al.* [12] Although the previous authors considered the depolarization field (and captured the effect of dipole-dipole interactions), they employed the macroscopic electric field E rather than the microscopic field E_{eff} to evaluate the polarization, resulting in an overestimation of the local effective charge.

Using Eqns. (5.2b) and (4.5b), we can calculate the local effective charge and polarizability for 2H-MoS_2. [182] We find $Z^* = 0.15$ and $\alpha = 100$ Å^3 in the intralayer direction. For IF-MoS_2, we employ the same equations and the effective dielectric data in Table 4.1 to extract the local effective charge and intralayer polarizability as $Z^* = 0.16\ e$ and $\alpha = 91$ Å^3, respectively. These results are summarized in Table 4.2. This analysis demonstrates that intralayer local effective charge is unaffected by strain and curvature in the nanomaterial. Interpreting the results in terms of chemical bonding, it shows that these chemically identical but morphologically different materials have the same ionicity. In other words, chemical bonding is the same.

4.4 Structural Strain in 2H- and IF-MoS_2

In light of this null result, how should we understand the significant decrease in the intralayer Born effective charge of the nanomaterial? The answer lies with the polarizability, a quantity that captures electron cloud distortion effects. Based upon our

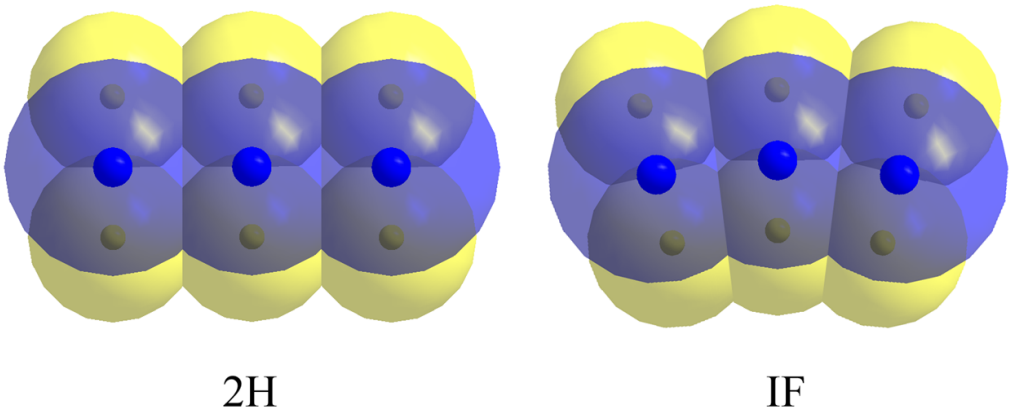

Figure 4.3: Schematic view of the electron clouds of 2H- and IF-MoS_2 in the intralayer direction, respectively. Here, we use spheres to indicate a generalized orbital. [1]

extracted values of α for 2H- and IF-MoS_2, we can see that intralayer Born effective charge decreases significantly in the nanomaterial due to a change in intralayer polarizability (Table 4.2). Figure 4.3 displays a schematic view of the effect of structural strain on the intralayer electron cloud of bulk and nanoscale MoS_2. It is this type of electron cloud distortion that reduces intralayer polarizability in IF-MoS_2. Since the total charge = local charge + non-local charge, electron cloud distortion can be considered to decrease non-local effective charge in the nanoparticles.

The absence of substantial charge and bonding differences in the interlayer direction of the nanomaterial is consistent with the weak van der Waals interactions between layers in transition metal dichalcogenides. In the interlayer direction, curvature simply has a limited effect on the Born effective charge in IF-MoS_2. Thus, we surmise that the interlayer polarizability remains relatively unchanged in the nanomaterial, and as a consequence, that local effective charge is the same for both materials in the interlayer direction (Table 4.2). Dielectric constant data (Table 4.1) is consistent with this conclusion. [183]

We can employ a Hooke's law analysis to extract the force constant k as:

$$\omega_{TO}^2 = [\omega_0^2 - \frac{\frac{N}{\epsilon_0}\frac{\eta(Z^*)^2}{\mu V}}{1 - \eta\frac{N\alpha}{V}}]. \tag{4.6}$$

Here, ω_0 is the spring-constant frequency ($\omega_0^2 = \frac{k}{\mu}$), and μ is the reduced mass. For both materials, we find $k = 338$ N/m for the E_{1u} mode and $k = 497$ N/m for the A_{2u} mode, again demonstrating that, while chemical bonding does not change, strain and curvature in the nanoparticles does affect ionic polarizability.

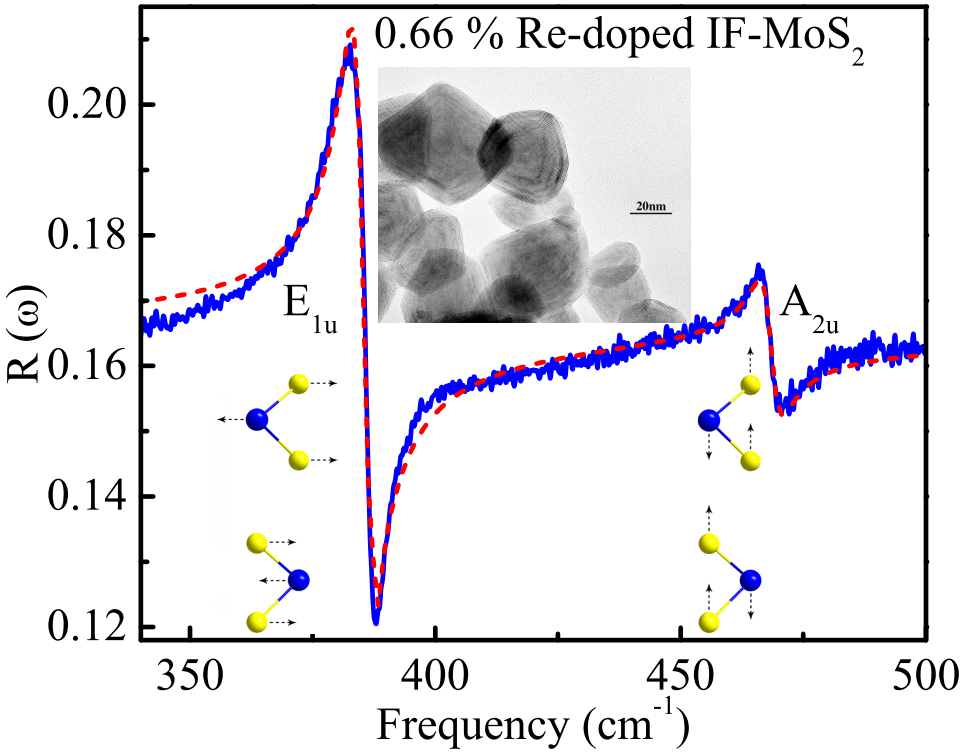

Figure 4.4: Close-up view of the 300 K reflectance spectra of Re-doped (0.66%) IF-MoS_2. Blue curve: experimental data for the Re-doped IF-MoS_2 sample. Red dashed line: theoretical fit as described in the text. Upper inset: high resolution transmission electron microscopy image of Re-doped (0.66%) nanoscale MoS_2, Lower inset: displacement patterns of infrared active E_{1u} and A_{2u} vibrational modes [138] in IF-MoS_2.

We point out that, in addition to quantifying bulk vs. nanoscale effects and assessing the size dependence of charge and bonding in nanoparticles, these techniques can be extended to include shape effects. MoS_2 nanotubes and nanobuds are the chemically identical "high aspect ratio" analogs in this case. [38, 45] At this time, sufficient quantities of material are not available to support an extended investigation.

Table 4.3: Observed and scaled parameters extracted from our oscillator fitting analysis of the measured reflectance spectra of Re doped and undoped IF-MoS_2.

Material	Mode	$\overline{S}_j$ $\cdot 10^{-3}$	$\overline{\varepsilon}_1(\infty)$	S_j $\cdot 10^{-3}$	$\varepsilon_1(\infty)$	$\omega_{TO,j}$ (cm^{-1})
2H-MoS_2	E_{1u}			200[a]	15.2[a]	384[a]
	A_{2u}			30[a]	6.2[a]	470[a]
IF-MoS_2	E_{1u}	36	5.6	77	8.3	384.6
	A_{2u}	6.7		29	6.2	467.9
Re-MoS_2 (0.12%)	E_{1u}	35.1	5.6	75	8.3	384.4
	A_{2u}	6.7		29	6.2	468.5
Re-MoS_2 (0.66%)	E_{1u}	34.7	5.6	74	8.3	384.5
	A_{2u}	6.7		29	6.2	468.2

[a] Single crystal data from Wieting's results. [13]

Finally, we also investigated the charge and bonding situation in Re-doped IF-MoS_2 samples. Based on the measured reflectance spectra of Re-IF-MoS_2, good quality fits were obtained using a total of two oscillators, as shown in Fig. 4.4. The fitting results are shown in Table 4.3 as observed parameters. After we apply the same density and distribution corrections discussed for the unsubstituted materials, [1] we

extract the intrinsic oscillator parameters of Re-doped IF-MoS_2. Note that, $S_{E_{1u}} =$ 0.075 and 0.074 for 0.12% and 0.66% Re-IF-MoS_2, respectively. The others are unchanged. We see that only intralayer oscillator strength $S_{E_{1u}}$ decreases gradually because of Re doping compared to $S_{E_{1u}} = 0.077$ for undoped IF-MoS_2. [1] Using these intrinsic optical constants, we can calculate the effective charges and polarizability according to the rigid ion model. [1,3,11] We find Born effective charge, $Z^*_{B,E_{1u}} = 0.69$ and 0.68 e for 0.12% and 0.66% Re-IF-MoS_2, respectively. The interlayer Born effective charges are unchanged within our sensitivity. We conclude that the light doping level is only a small perturbation on the vibrational properties in the intralayer direction. Rapoport *et al.* found Re-IF-MoS_2 showed better tribological behavior than IF-MoS_2 , and suggested that the negatively charged surfaces of Re doped nanoparticles remarkably affect their rheological properties and their tribological behavior. [149] From the charge and bonding point of view, the effective charges and chemical bond are unchanged in our sensitivity because of the light doping level. An electron-rich system of Re-IF-MoS_2 does, however, change the optical properties of nanoparticles compared to IF-MoS_2. These findings discussed elsewhere.

Chapter 5

Infrared Vibrational Properties of Bulk and Nanoscale MnO

5.1 Experimental Determination of Ionicity in Bulk and Nanoscale MnO

Figure 5.1(a) displays the infrared reflectance of single crystal, bulk powder, and nanoscale MnO at 300 K. The bulk powder data has been corrected for surface scattering, and the nanoparticle data has been corrected for both surface scattering and the reflectance of the capping ligand. There is one vibrational mode, in agreement with group theoretical predictions. As anticipated, [16–18] the spectrum is broad and shows strong anharmonic effects, similar to other simple salts like NaCl and KBr. [185,186] Our approach to the investigation of charge and bonding in bulk and nanoscale MnO thus consists of (i) a measurement of reflectance (Fig. 5.1(a)), (ii) subsequent calculation of optical conductivity via a Kramers-Kronig analysis (Fig. 5.1(b)), (iii) extraction of the oscillator strength or plasma frequency and application of appropriate corrections for density and capping ligand effects (as detailed in the

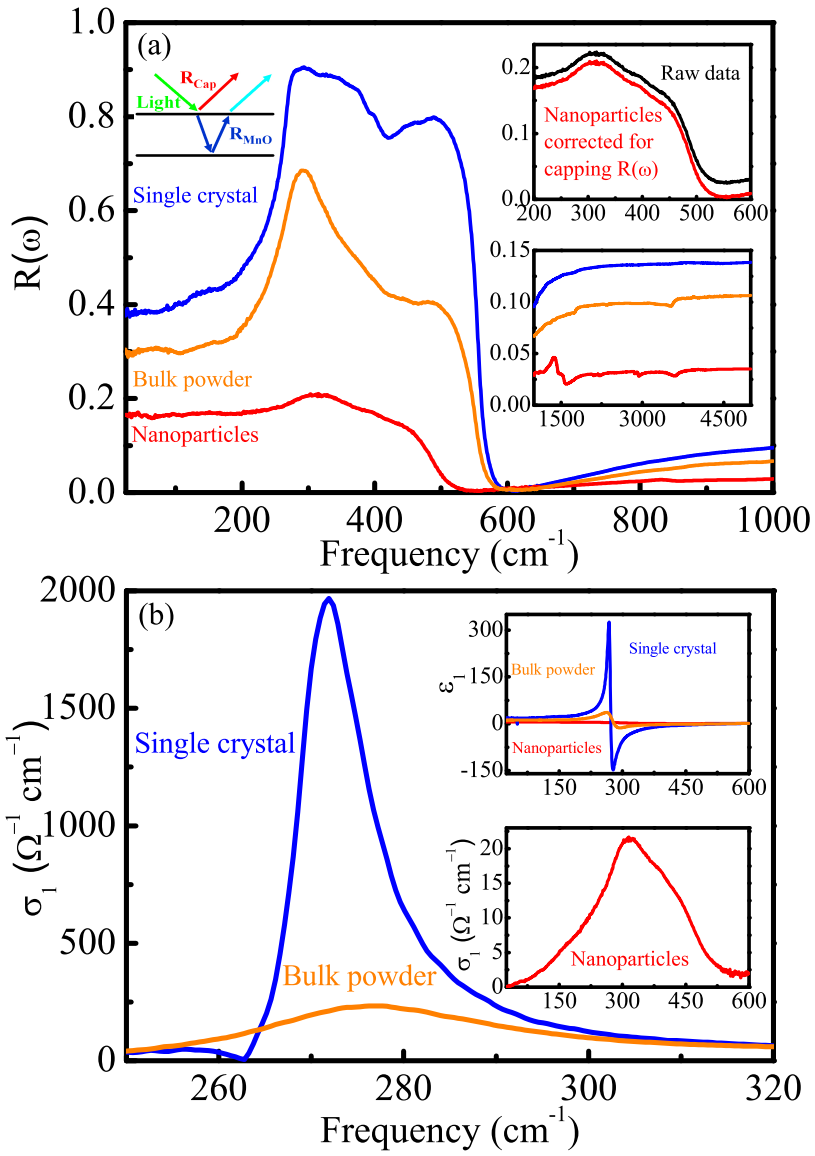

Figure 5.1: (a): 300 K reflectance spectra of single crystal, bulk powder , and nanoscale MnO corrected for surface scattering and capping ligand reflectance. Upper left inset: schematic diagram of the two-layer assumption. Upper right inset: effect of the two-layer correction on the reflectance of nanoscale MnO. Lower right inset: the middle infrared spectra of single crystal, powdered, and 8 nm MnO. (b): 300 K optical conductivity of single crystal and bulk powder MnO. Upper inset: $\varepsilon_1(\omega)$ of single crystal, bulk powder, and nanoscale MnO. Lower inset: 300 K conductivity of nanoscale MnO. The extremely broad peak in $\sigma_1(\omega)$ of the nanoparticles indicates a much shorter phonon lifetime compared to the bulk, which does not impact the value of Z_B^*. [3, 110]

Methods section) to yield the intrinsic optical constants, and (iv) an effective charge analysis. [1–3]

In this work, we employed a Kramers-Kronig analysis [110, 187] to calculate the optical constants of single crystal, bulk powder, and nanoscale MnO. The advantage of this procedure is that it directly relates reflectance and phase shift to the complex dielectric response of a material $\varepsilon(\omega) = \varepsilon_1(\omega) + i\varepsilon_2(\omega) = \varepsilon_1 + \frac{4\pi i}{\omega}\sigma_1(\omega)$, where $\sigma_1(\omega)$ is the optical conductivity. [110, 187] A partial sum rule analysis of the optical conductivity thus allowed us to extract effective plasma frequency, $\overline{\omega}_p$, and the value of the effective high frequency dielectric constant, $\overline{\varepsilon}_1(\infty)$, which can be obtained from appropriate limits of $\varepsilon_1(\omega)$. One more step is required to get the intrinsic optical constants. The intrinsic value of the effective plasma frequency ω_p is related to the $\overline{\omega}_p$ extracted from a Kramers-Kronig analysis as $\overline{\omega}_p^2 = (\omega_p)^2 v$. [1, 2] Likewise, the intrinsic value of the effective high frequency dielectric constant $\varepsilon_1(\infty)$ is related to the extracted value as $\overline{\varepsilon}_1(\infty) = 1 + [\varepsilon_1(\infty) - 1]v$. [1, 2] Here, v is the scaling factor. In our implementation, it refers to the combination of pellet density and amount of MnO in the sample. Thus, for the bulk powder, $v = 0.74$. For the nanoparticles, $v = (0.47)\cdot(0.75)$, a combination of density and surface coverage effects. Of course, $v = 1.0$ for the single crystal. The rational for this analysis is summarized in Table 2.4. We note that density corrections were used with some success in MoS2 system. [1] The intrinsic values of $(\omega_p)^2$ and $\varepsilon_1(\infty)$ are obtained by this procedure and shown in Table 5.1.

Table 5.1 summarizes the intrinsic values of the squared effective plasma frequency and high frequency dielectric constant for single crystal, bulk powder, and nanoscale MnO. The values obtained for both bulk materials agree well with each other and similar data reported by Plendl, Mochizuki, and Rudolf *et al.* [16–18]. Small size reduces $(\omega_p)^2$ from 12.26×10^5 to 7.74×10^5 cm^{-2}. $\varepsilon_1(\infty)$ is reduced

from 4.82 to 4.21. Based on these intrinsic optical constants, we can calculate the effective charge according to the rigid ion model. [1, 10, 11] The latter gives a precise relationship between effective plasma frequency and Born effective charge:

$$4\pi^2 c^2 \sum_j (\omega_{p,j})^2 = 4\pi^2 c^2 \varepsilon_1(\infty) \sum_j ((\omega_{LO,j})^2 - (\omega_{TO,j})^2) = \frac{Ne^2}{\epsilon_0 V} \sum_k \frac{(Z^*_{B,k})^2}{m_k}. \quad (5.1)$$

Here, Z^*_{Bk} is Born effective charge on the k-th ion, $\omega_{p,j}$ is the intrinsic value of the effective plasma frequency for the j-th oscillator, $\omega_{TO,j}$ and $\omega_{LO,j}$ are the intrinsic transverse and longitudinal optical phonon frequencies, respectively, $\varepsilon_1(\infty)$ is the intrinsic effective high frequency dielectric constant, N is the number of formula units in the unit cell, V is the volume of the MnO formula unit, m_k is the atomic mass of the k-th atom, ϵ_0 is the permittivity of free space, e is the electronic charge, and c is the speed of light. The sum rule, $\sum Z^*_{B,k} = 0$, guarantees that the charge neutrality condition is fulfilled. This rendering is well-suited to the analysis of both bulk and nanomaterials [1, 2] and is employed in this work to evaluate charge and bonding in MnO.

Table 5.1 displays the Born effective charge, Z^*_B, for the Mn center of single crystalline, bulk powder, and nanoscale MnO, calculated according to Eq. 5.1. Within our sensitivity, the Born effective charge of the single crystal and bulk powder are nearly identical ($Z^*_B = 2.60\ e$ vs. $2.53\ e$), as they should be, once density is taken into account. This correspondence demonstrates that the approach outlined here can be reliably extended to analyze powdered materials. [1, 2] The results are also in line with previous estimates of Z^*_B in bulk MnO. [19, 24]

This analysis also reveals striking finite size effects. Compared to the chemically identical but morphologically different bulk material, the Born effective charge of the nanoparticles is reduced significantly, by ∼20% (from 2.60 e to 2.06 e). Similar effects

Table 5.1: 300 K optical constants of single crystal, bulk powder, and nanoscale MnO as extracted from the measured reflectance spectrum by an Kramers-Kronig analysis along with the Born (Z_B^*) and local (Z^*) effective charge for the Mn center, and total polarizability (α), which is the sum of cationic and anionic polarizabilities. [3, 188]

Materials	$(\omega_p)^2$ (10^5 cm^{-2})	$\varepsilon_1(\infty)$	Z_B^* (e)	α (Å^3)	Z^* (e)	k (N/m)
Single crystal	12.26	4.82	2.60	36.9	1.14	185
Bulk powder	11.54	4.85	2.53	37.0	1.11	185
Nanoparticles	7.74	4.21	2.06	34.0	1.00	165
Difference			−20%	−8%	−12%	

were observed in the intra-layer direction of the model transition metal dichalcogenide MoS_2, where Z_B^* of the Mo center drops from 1.11 e in the bulk material to 0.69 e in the nested nanoparticles. [1] In order to understand this trend, it is useful to realize that Z_B^* contains both static and dynamic contributions. Decomposition is needed to quantify the impact of confinement on charge and bonding. Total polarizability (α) and local (Szigeti) effective charge (Z^*) are given as: [1, 2]

$$Z^* = Z_B^* \cdot (1 - \eta \frac{N\alpha}{V}) \tag{5.2a}$$

$$\alpha = \frac{V \cdot (\varepsilon_1(\infty) - 1)}{N \cdot (\eta\varepsilon_1(\infty) - \eta + 1)}. \tag{5.2b}$$

Here, η is the depolarization factor. [189] N and V are defined as before. In this rendering, α is the sum of cationic and anionic contributions. From the physical point of view, polarizability is proportional to electron cloud volume. Changes in α measure electron cloud distortion and are long range effects. Local effective charge is different. It is, by nature, a short-range interaction related to relative ionic displacement and quantifies chemical bonding. For a fully covalent material like diamond or silicon, $Z^* = 0$ e, whereas for a strongly ionic compound like NaCl, $Z^* = 0.8$ e for the Na site. [8] Previous estimates place the local (Szigeti) effective charge of bulk MnO at 1.08 e for the Mn center. [16] This framework along with the vibrational response of bulk and nanoscale MnO (Fig. 5.1) can be used to quantify finite size effects on total polarizability and local effective charge.

Table 5.1 displays the total polarizability and local effective charge for single crystal, bulk powder, and nanoscale MnO at room temperature, calculated according to Eqs. 5.2a and 5.2b. Our estimate of Z^* for the Mn center in bulk MnO (both single crystal and bulk powder) is in excellent agreement with Plendl's results. [16]. The findings for the nanoparticles are quite different. Our analysis reveals that total polarizability drops by $\sim$8% in the nanoparticles, whereas local effective charge decreases by $\sim$12%. That nanoscale size effects in MnO manifest themselves in both α and Z^* is fundamentally different than the situation in MoS_2, where the confinement that acts to reduce Born effective charge in the nested nanoparticles is fully contained in the total polarizability. [1] How should we interpret these changes in MnO? One immediate and very accessible finding is that the 8 nm nanoparticles are less ionic than the bulk material, as evidenced by the decrease in Z^* from 1.14 e to 1.00 e (Table 5.1). This is not an "expanded volume effect" within the nanoparticles because the lattice constants of bulk and nanoscale MnO are identical within our sensitivity. [119] Interpreted in terms of improved electron cloud overlap (which

favors stronger covalent interactions), the reduced total polarizability of the MnO nanoparticles reinforces this trend. [190] Taken together, the decrease in both α and Z^* in the 8 nm MnO nanoparticles reveals modified interactions that stabilize the large uncompensated surface and balance the associated strain.

It is interesting to consider exactly where this charge deficiency might reside in the 8 nm MnO nanoparticles. (Here, the phrase "charge deficiency" refers to the reduced chemical bond ionicity, not free-standing charge.) Infrared spectroscopy is a microscopic technique, but, similar to many other physical probes, the spatial resolution is wavelength-limited and, as such, provides a spatial (ensemble) average. Therefore, the aforementioned effective charges and total polarizability are average quantities (i.e., on average, the MnO nanoparticles are $\sim$12% less ionic than the extended solid). While our experiments do not reveal precisely how charge is distributed in a nanoparticle, several limiting cases can be considered. For instance, (i) charge can be preferentially localized in the outer layers, with pinning due to strain and the uncompensated surface; (ii) charge may be homogeneously distributed over the entire 8-nmnanoparticle; and (iii) charge can be inhomogeneously distributed over the particle with a length scale that describes relaxation of charge and strain, given by the dielectric and elastic characteristics of the material. Because of surface strain and capping ligand-uncompensated surface interactions, the lattice of the nanoparticle sample will respond less readily than that of the single crystal to outside stimuli. This suggests that the reduced ionicity or "charge deficiency" may preferentially localize in the surface layers. However, there is certainly no skin effect in a dielectric. A reasonable compromise is to allow the charge deficiency and associated lattice distortion to disappear gradually. Consideration of a simple dielectric sphere provides insight here and suggests a relevant length scale of a few unit cells, [191] analogous to polar surface reconstruction, which is well-known to lower ionicity. [192]

5.2 Magneto-Elastic Coupling in Bulk and Nanoscale MnO Through the 118 K Néel Transition

5.2.1 Evaluating Born and Local Effective Charges in the Low Temperature Phase

Figure 5.2 displays the variable temperature reflectance of single crystalline and nanoscale MnO. The clear mode splitting below 118 K in the single crystal (Fig. 5.2(a)) is easily interpreted as evidence for the rhombohedral distortion in the AFMII phase. [18, 102, 157, 193] The nanoparticles are different (Fig. 5.2(b)). Here, the reflectance changes gradually through T_N, without well-defined mode splitting. We employed a Kramers-Kronig analysis to calculate the optical properties of both materials from the measured reflectance. [110] A partial sum rule analysis of the optical conductivity (along with appropriate corrections for pellet density and the quantity of capping ligand) allowed us to extract intrinsic effective plasma frequencies as a function of temperature. [3,110] The square of this quantity, $(\omega_p)^2$, is shown in Figs. 5.3(a) and (b) for bulk and nanoscale MnO.

Based on the intrinsic effective plasma frequency, we can calculate the Born effective charge using Eq. 5.1. Relating ω_p to Z_B^* is the best way to analyze and compare both bulk and nanoscale materials. [1–3] We can separate the static and dynamic contributions to Z_B^* by calculating local (Szigeti) effective charge (Z^*) and total polarizability (α) using Eqs. 5.2a and 5.2b. From the physical point of view, local effective charge quantifies chemical bonding in terms of its ionicity or covalency, and total polarizability is proportional to electron cloud distortion. [8]

Armed with this charge and bonding model and our reflectance data (Fig. 5.2), we can investigate changes in Z_B^*, Z^*, and α through the Néel transition. Figures 5.3(a), (c), (e), and (g) show the temperature dependence of the important quantities for the

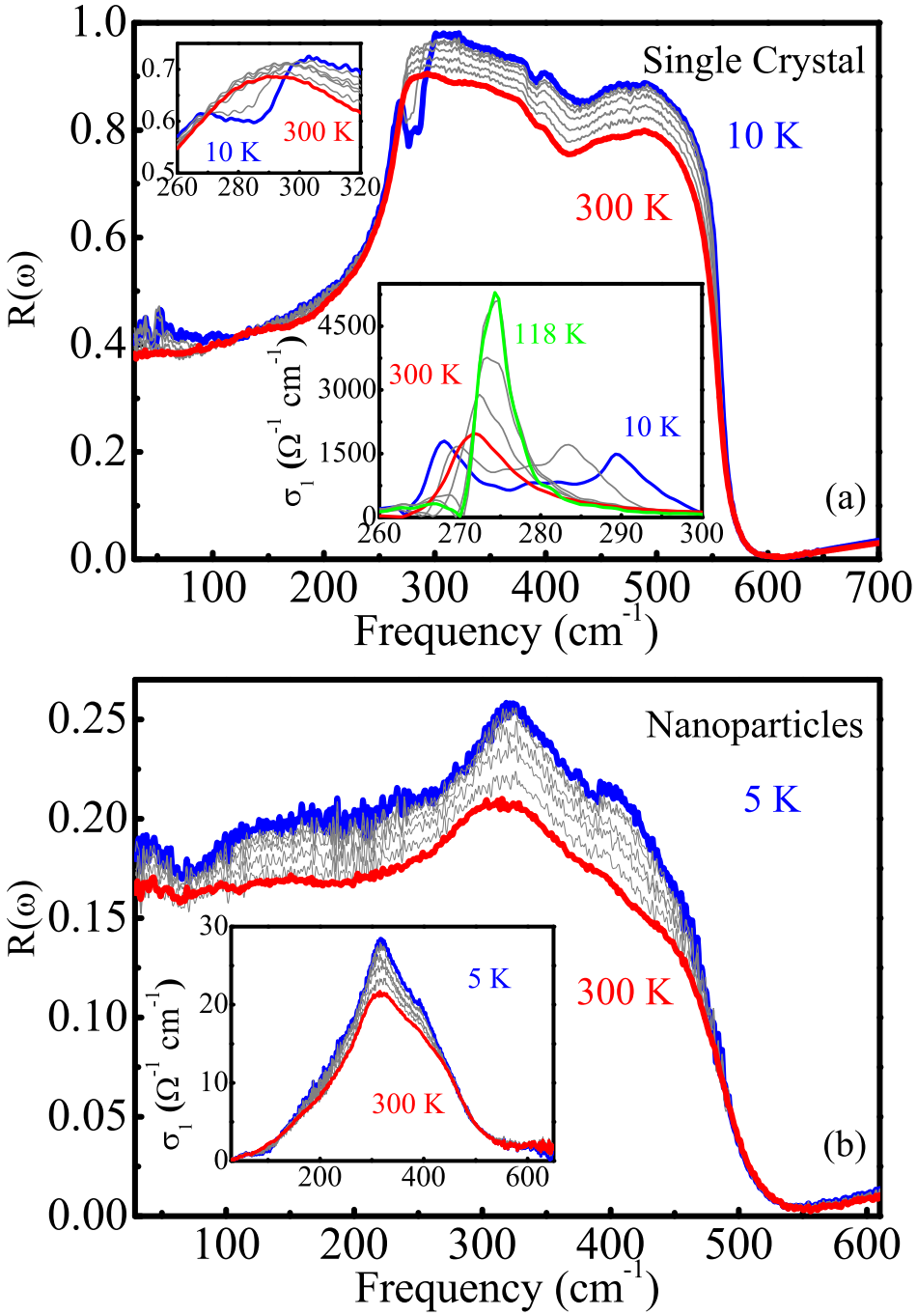

Figure 5.2: (a) Variable temperature reflectance spectra of single crystal MnO. Inset: optical conductivity of MnO single crystal at various temperatures. (b) Variable temperature reflectance spectra of nanoscale MnO. Upper inset: TEM image of 8 nm MnO particles. Lower inset: Optical conductivity of nanoscale MnO as a function of temperature. [4]

single crystal. We note that $(\omega_p)^2$ drops sharply at the transition temperature, [194] in agreement with the static dielectric data of Seehra *et al.* [102] but different than the trend in ω_p reported by Rudolf *et al.* [18] Z_B^* for the Mn center in the (100) plane (solid squares, Fig. 5.3(c)) shows an ∼10% decrease (from 3.3 to 2.9 e) at T_N. The local effective charge trend is quite similar. Analogous data for the 8 nm MnO nanoparticles are shown in Figs. 5.3(b), (d), (f), and (h). There is only a modest change in Born and local effective charges at T_N. Total polarizability (Figs. 5.3(g) and (h)) rises linearly with decreasing temperature in both materials, with no obvious change at T_N.

5.2.2 Low Temperature Phase Anisotropy in the Effective Charge

In a effort to obtain a more complete picture of charge and bonding in the low temperature phase, we sought to account for anisotropy. These effects are important only below T_N where symmetry breaking gives Z_B^*, Z^*, and α directional character. We begin by recalling that MnO is in the AFMII state below 118 K, with spins aligned in the (111) plane and the planes stacked antiferromagnetically in the [111] direction (Fig. 5.4). [74,105,106] A triply-degenerate vibrational mode will thus split into two types of features below T_N. [74,102] The doubly-degenerate component is in the (111) plane, whereas the singly-degenerate portion is in the [111] direction. This anisotropy effect is clearly evident in Seehra's dielectric data. [102] Our measurements were, however, carried out on the (100) face of the single crystal. They thus represent an average. We can estimate the anisotropy in the intrinsic effective plasma frequency by realizing that $(\omega_p)^2$ in the (100) plane has a straightforward relationship with its components below T_N: $(\omega_p)^2 = \frac{2}{3}(\omega_p)^2_{(111)} + \frac{1}{3}(\omega_p)^2_{[111]}$. [1, 2] Here, $(\omega_p)_{(111)}$ is the intrinsic effective plasma frequency in the (111) plane, and $(\omega_p)_{[111]}$ is the intrinsic

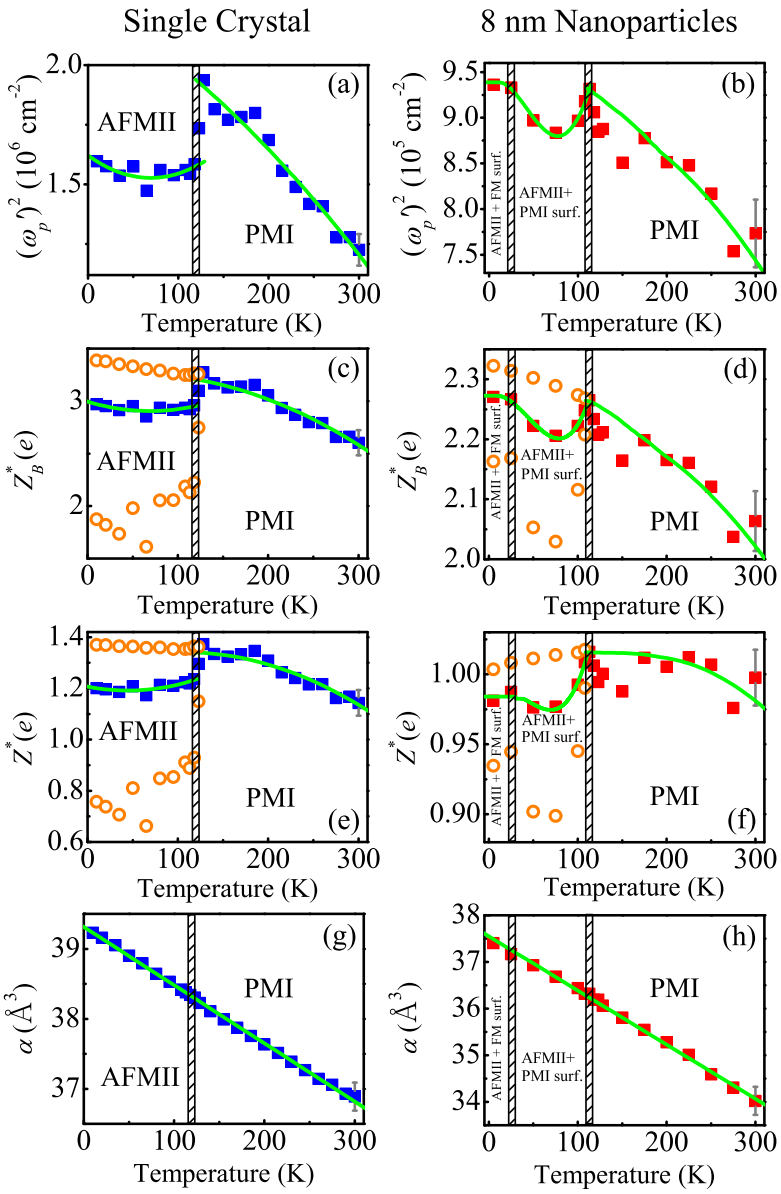

Figure 5.3: The square of the intrinsic plasma frequency ($(\omega_p)^2$), Born (Z_B^*) and local (Z^*) effective charges for the Mn center, and total polarizability (α) of single crystal and nanoscale MnO as a function of temperature. The solid squares show results based on observed values (single crystal: (100) plane; nanoparticles: isotropic). [188] The solid lines guide the eye. The open circles show calculated results that include an orientational correction (described in the text). The vertical dashed lines denote transition temperatures. The 118 K Néel transition has already been discussed extensively. Uncompensated surface spins may give rise to weak ferromagnetism below 30 K. [4, 31, 32, 35]

effective plasma frequency in the [111] direction. Below T_N, we can calculate $(\omega_p)^2_{(111)}$ from an extended least squares fit to the high temperature phase data. $(\omega_p)^2_{[111]}$ is then obtained as the difference. We can use these directionally-resolved values of $(\omega_p)^2_{(111)}$ and $(\omega_p)^2_{[111]}$ to calculate Born and local effective charges for the MnO single crystal below T_N (open circles, Figs. 5.3(c) and (e)). [195] Considering that total polarizability is insensitive to T_N and that the lattice distortion below 118 K is relatively modest, we assume that α does not have orientational dependence. This assumption is consistent with short range interactions dominating the transition.

The MnO nanoparticles are different. They display much weaker changes in Born and local effective charges with temperature, with only a small cusp (on the order of 3%) in the transition regime (solid squares, Figs. 5.3(d) and (f)). We can account for low temperature phase anisotropy by recalling the spherical shape (TEM image, inset of Fig. 5.2(b)). This indicates that anisotropy effects in the nanoparticles are orientationally averaged. The intrinsic effective plasma frequency below T_N can therefore be written in terms of its components as $(\omega_p)^2 = \frac{2}{3}(\omega_p)^2_{(111)} + \frac{1}{3}(\omega_p)^2_{[111]}$. Below T_N, we again calculate $(\omega_p)^2_{(111)}$ from an extended least squares fit to the high temperature phase data. $(\omega_p)^2_{[111]}$ is then obtained as the difference. Thus, we can calculate directionally-resolved Born and local effective charges for the nanoparticles below T_N (open circles, Figs. 5.3(d) and (f)). The low-temperature splitting of Z^*_B and Z^* is significantly less than that in the single crystal, revealing the reduced importance of the lattice distortion. This consistant with lack of splitting in measured data (Fig. 5.2(b)). Total polarizability is again insensitive to T_N, demonstrating that modified exchange interactions do not impact electron cloud volume at the transition.

5.2.3 The Estimate of the Spring Constant Frequency

We also employed a Hooke's law analysis to extract the elastic parameters as: [1, 2]

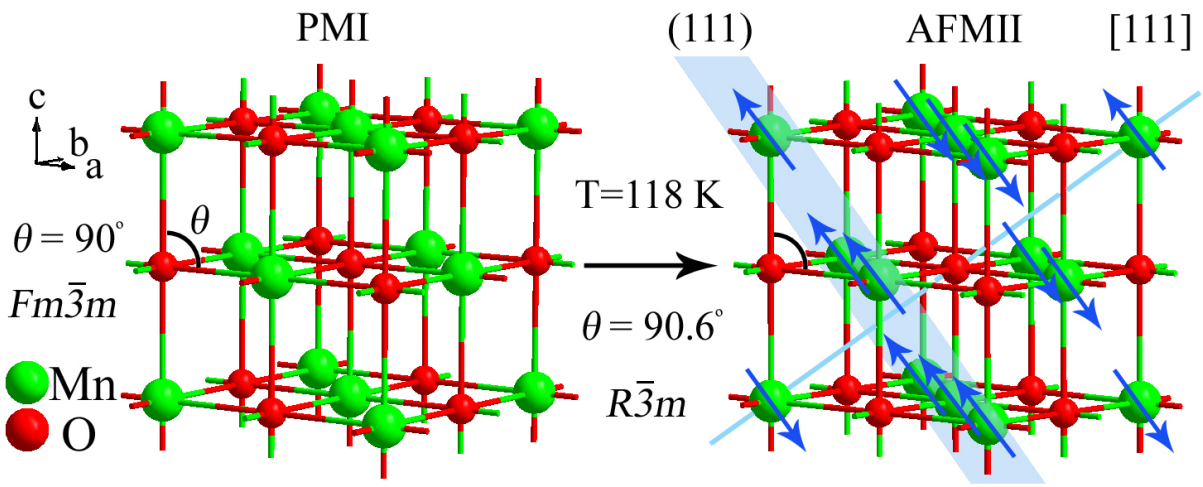

Figure 5.4: Left: 300 K cubic crystal structure. Right: Low temperature rhombohedral crystal structure with AFMII magnetic arrangement. Spins are aligned in the (111) plane, and the planes are stacked antiferromagnetically in the [111] direction. [4]

$$\omega_0^2 = \frac{k}{\mu} = (\omega_{TO})^2 + \frac{\frac{N}{\epsilon_0}\frac{\eta(Z^*)^2}{\mu V}}{1 - \eta\frac{N\alpha}{V}}. \tag{5.3}$$

Here, ω_0 is the spring constant frequency [196] (useful for our analysis of spin-phonon coupling, below), k is spring constant, and μ is the reduced mass. The second term in the above expression dominates due to the importance of ω_p (or oscillator strength) compared to ω_{TO}. [2,110] To evaluate Eq. 5.3, we need several parameters. We already have Z^* and α for both materials. [197] The ω_{TO}'s can in principle be extracted directly from the optical conductivity (insets, Figs. 5.2(a) and (b)). Let's examine this data. The frequency dependent conductivity of single crystalline MnO (lower inset, Fig. 5.2(a)) reveals two strong peaks below T_N that we assign as split TO phonons. In our 10 K data, the two TO phonons are observed at 268 and 289 cm^{-1}, similar to the results of Chung *et al.* (269 and 294 cm^{-1} at 4.3 K). [157] The smaller feature midway between the two larger peaks is not observed in inelastic neutron scattering experiments [157] and may be related to anharmonicity effects. We must also obtain ω_{TO}'s for the nanoparticles. The optical conductivity displays a peak from which we can extract one ω_{TO}. The value ($\omega_{TO} = 318$ cm^{-1}) is slightly larger than that obtained for the single crystal, a finding that is supported by direct transmittance (Fig. 5.5(b)). There is, however, little temperature dependence and no vibrational fine structure in the low temperature phase (Fig. 5.2(b)). According to our analysis, [198] phonon lifetime effects prevent the observation of TO mode splitting in the nanoparticles. Thus, the splitting in the spring constant discussed below emanates only from splitting in Z^*.

Using Eq. 5.3, we can extract the spring constants for both materials (Figs. 5.5(c) and (d)). In the MnO single crystal, $k = 185$ N/m at room temperature. The spring constant splits into two branches below T_N, with limiting low temperature values of 124 and 257 N/m. The nanoparticles are different. Here, k is overall lower

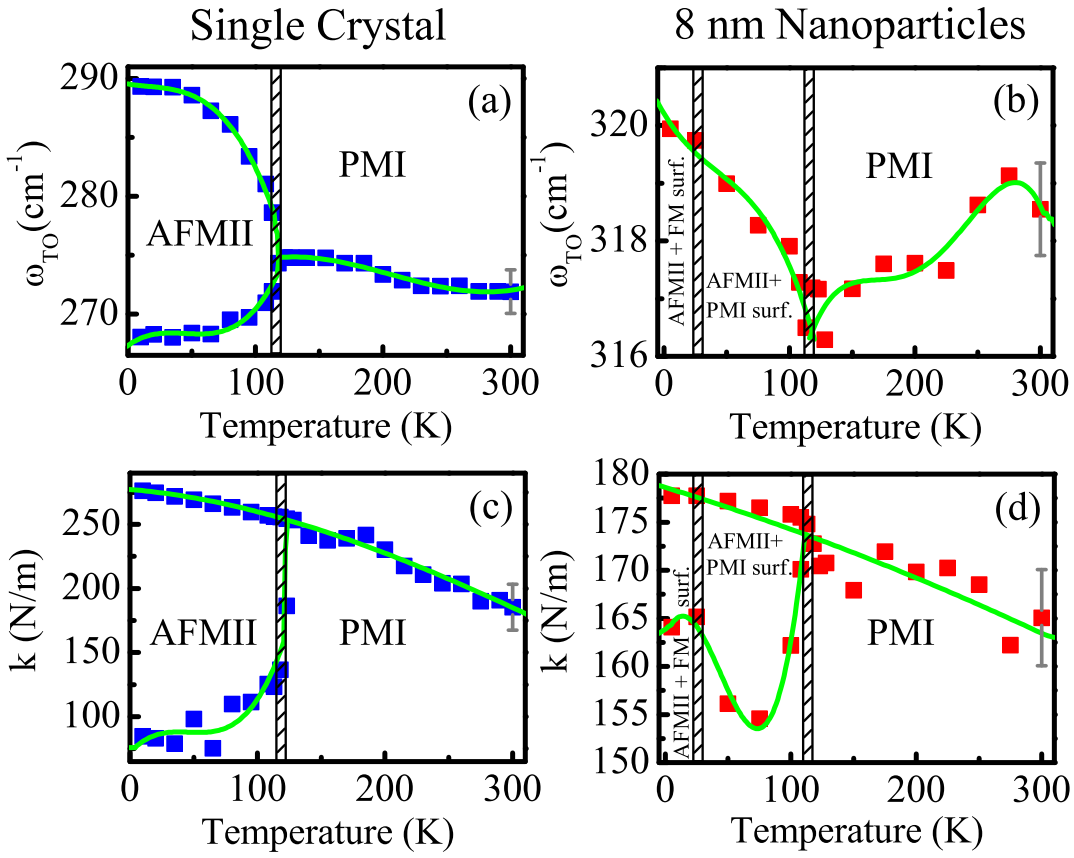

Figure 5.5: (a) Transverse optic phonon frequency ω_{TO} of the MnO single crystal as a function of temperature. (b) 300 K transmittance of bulk powder and nanoparticles. (c) and (d) Spring constant, k, of single crystal and nanoscale MnO as a function of temperature. This calculation of k includes an estimate of orientational effects. The solid lines guide the eye. The vertical hashed lines denote transition temperatures. [4]

because the nanoparticles are softer and less ionic than the single crystal. [3] The spring constant is 165 N/m at 300 K, with limiting low temperature values of 163 and 177 N/m. The weak splitting at T_N and modest temperature dependence of the lower frequency (spin-spin coupled) branch of k below 118 K is another consequence of the finite size effect.

5.2.4 Evaluating Magneto-Elastic Coupling

In order to quantify the spin-phonon coupling, we invoke the well known expression: [67, 89]

$$\omega^2 = \omega_0^2 + \lambda \langle S_i \cdot S_j \rangle. \tag{5.4}$$

Here, ω and ω_0 are the spring constant frequencies with and without spin-spin coupling, $\lambda = \frac{1}{\mu} \cdot \frac{\partial^2 J}{\partial u^2}$ is the macroscopic spin-phonon coupling (J is the magnetic exchange and u is displacement), and $\langle S_i \cdot S_j \rangle$ is the low temperature near neighbor spin-spin correlation function. The latter reduces to $3S^2$ in the low temperature AFMII phase for a single formula unit of bulk MnO with $S = \frac{5}{2}$. [74,105] Using Eq. 5.4 along with the data in Fig. 5.5(c) and the realization that $\omega_0^2 = \frac{k}{\mu}$, we find $\frac{\partial^2 J}{\partial u^2} = \lambda \cdot \mu \approx 5$ N/m for the MnO single crystal. This value agrees reasonably well with the theoretical estimate (10.7 N/m) of Luo *et al.* [74] Because the spin-spin correlation function for the nanoparticles is not known, we elected to employ the same literature value of $\langle S_i \cdot S_j \rangle$. We find $\frac{\partial^2 J}{\partial u^2} = \lambda \cdot \mu \approx 0.5$ N/m for the 8 nm MnO nanoparticles, an order of magnitude less than in the single crystal. This is clearly a lower bound on the coupling because it assumes that all $\Delta\omega$ effects are manifest in $\lambda \cdot \mu$. Direct measurements of $\langle S_i \cdot S_j \rangle$ for the nanoparticles would be very useful to decompose the frequency shift information into $\frac{\partial^2 J}{\partial u^2}$ effects, $\langle S_i \cdot S_j \rangle$, or a combination. [199] The lack of low temperature phase spectral splitting (Fig. 5.2(b)) dovetails with the finding of smaller coupling. Spectroscopists often employ a shorthand formula to describe spin-phonon

coupling: $\omega \approx \omega_0 + \lambda' \langle S_i \cdot S_j \rangle$. [68, 73] Combining this formula with our data yields $\lambda' \approx 7$ cm^{-1} for the single crystal. This value compares well with couplings for many frustrated oxides like $ZnCr_2O_4$, $DyMn_2O_5$, and $Ni_3V_2O_8$. [68, 70, 71, 75] Within this formalism, we find $\lambda' < 1$ cm^{-1} for the nanoparticles, indicative of weak coupling. This is consistent with (i) the much shorter phonon lifetime compared to the time scale of infrared vibrational spectra, (ii) the reduced antiferromagnetic proportion in these strained nanoparticles. [31–36, 118, 200] in the nanoparticles Similar trends were recently observed in Cr_2O_3 nanoparticles. [92]

Chapter 6

Spectroscopic Signature of the Superparamagnetic Transition and Surface Spin Disorder in $CoFe_2O_4$ Nanoparticles

6.1 Superparamagnetic Transition in $CoFe_2O_4$ Nanoparticles

Figure 6.1 shows coercivity, H_c, as a function of nanoparticle size for $CoFe_2O_4$. The 14.0 and 10.4 nm particles display magnetic hysteresis loops and non-zero coercivities, whereas hysteresis loops are not observed in the 7.1 and 5.0 nm materials (Fig. 2.14 and Table 2.5). There is clearly a size-driven crossover between the hysteretic and non-hysteretic ($H_c = 0$) regimes in the 7 - 10 nm size range. Above the magnetic crossover, the 14.0 and 10.4 nm $CoFe_2O_4$ nanoparticles are in the ferrimagnetic state. We can understand the behavior of these larger particles by considering the

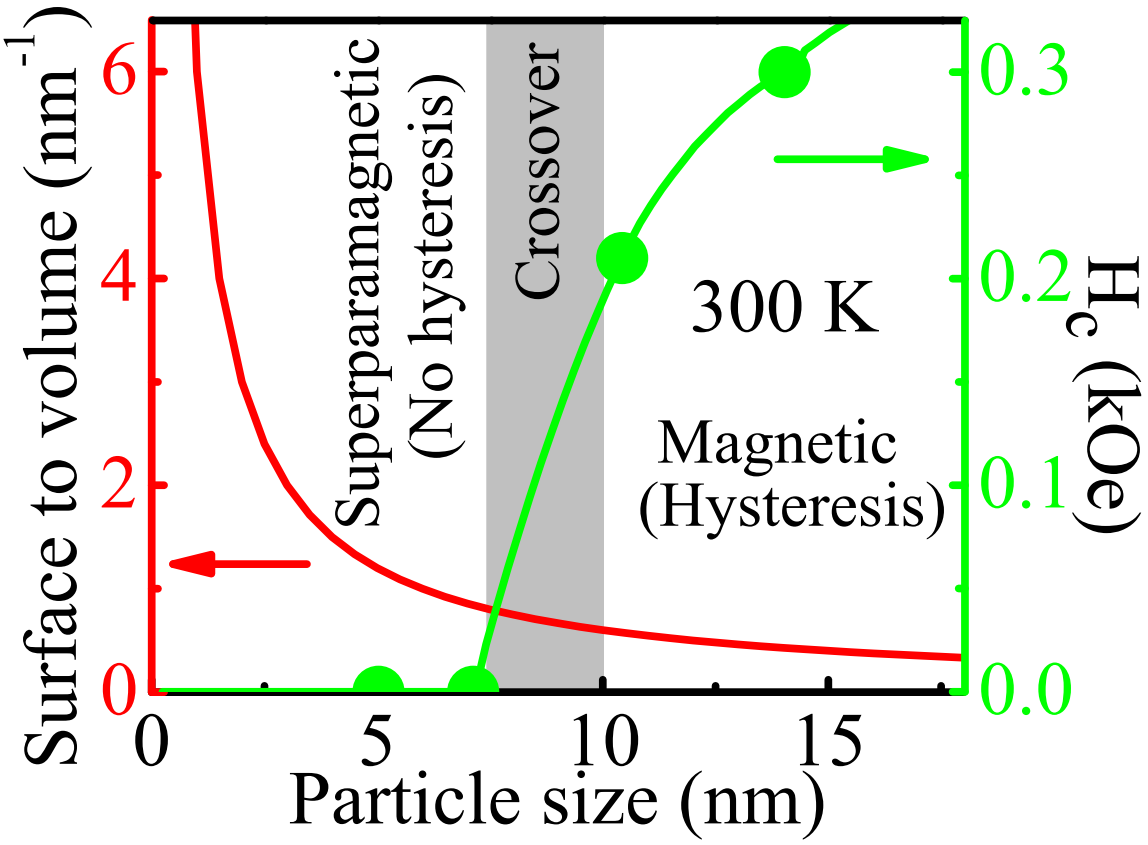

Figure 6.1: Surface-to-volume ratio and coercivity as a function of particle diameter. The magnetic crossover regime (from the hysteretic ferrimagnetic regime at large sizes to the superparamagnetic state at small particle sizes) is denoted by the vertical gray band. The green line connecting coercivity data points guides the eye. [5]

magnetocrystalline anisotropy energy, E_A, which goes as $KVsin^2\theta$. [164, 201, 202] Here, K is the magnetocrystalline anisotropy, V is the nanoparticle volume, and θ is the angle between the magnetization direction and the easy axis of the nanoparticle. A hysteresis loop is observed when magnetocrystalline anisotropy is larger than the thermal energy, [164, 202] which in this case, is 300 K. A reduced remanence can also be extracted. Below the magnetic crossover, the 7.1 and 5.0 nm particles are in the superparamagnetic state. [134] Here, spin acts as a giant moment, the energy landscape is characterized by doubly-degenerate minima separated by an energy barrier, and when temperature is larger than the barrier, the magnetization direction flips randomly. [97, 203]

Stoner-Wohlfarth theory provides a framework within which we can understand these effects. [163, 201] Here, the coercivity of a single-domain particle is expressed as $2K/\mu_0 M_s$, where K is the previously mentioned magnetocrystalline anisotropy, M_s is the saturation magnetization, and μ_0 is the permeability of free space. In the superparamagnetic state, magnetocrystalline anisotropy is overcome by thermal effects, a situation that renders K unimportant (and effectively zero). Figure 6.1 also displays the surface-to-volume ratio as a function of particle size. The $H_c > 0$ behavior of the 14.0 and 10.4 nm $CoFe_2O_4$ particles correlates with low surface-to-volume ratios, whereas the superparamagnetic ($H_c = 0$) state of the 7.1 and 5.0 nm particles correlates with larger surface-to-volume ratios. [161, 164, 204] In the following discussion, we combine these magnetic property trends with complementary vibrational spectroscopies to more deeply investigate the ferrimagnetic $\rightarrow$ superparamagnetic transition and signatures of surface spin disorder in magnetic nanoparticles.

6.2 Spin-Phonon Coupling in Bulk $CoFe_2O_4$ and Calculation of $\langle S_i \cdot S_j \rangle$

Figure 6.2(a) displays the infrared absorption of bulk and nanoscale $CoFe_2O_4$. The spectrum of the bulk material shows three vibrational modes at ∼577 (ν_1), 382 (ν_2), and 190 cm^{-1} (ν_3), in agreement with prior results. [104,205,206] In the nanoparticles, ν_3 is extremely weak, probably due to combined phonon lifetime effects, damping, and (for coupled systems like $CoFe_2O_4$) magnetic relaxation time effects. [4, 110, 164, 207, 208] We therefore focus on trends in ν_1 and ν_2 to reveal the spectroscopic signatures of the superparamagnetic transition and surface spin disorder. Figures 6.2(f) and (g) display the calculated displacement patterns for ν_1 and ν_2. [104, 209] For ν_1, the tetrahedral metal centers vibrate against the oxygen cage, and the octahedral metal centers vibrate against each other and the surrounding oxygen sites. For ν_2, the tetrahedral metal center is fixed and oxygen cage vibration is balanced by octahedral cation + cage motion. Here, the octahedral metal center vibrates against the other B site cation and the surrounding oxygen centers.

We can understand the peak shape in bulk $CoFe_2O_4$ by recalling that this system is ferrimagnetic at room temperature. [159] Figure 6.2(b) shows a representative two-oscillator fit to ν_1 and ν_2. The presence of magnetic ordering [159] motivates our assignment based upon strong spin-phonon coupling and provides a natural physical explanation for the observed doublet structure in this and other spinels. [4, 74, 104] The motion of ions in a solid is well-known to couple with charge. [1, 3, 11, 110] This type of interaction is the basis for traditional dynamics calculations that yield mode frequencies and displacement patterns of the sort discussed above. In some materials, the motions of ionic centers also couples with spins. [4,68,74] As mentioned

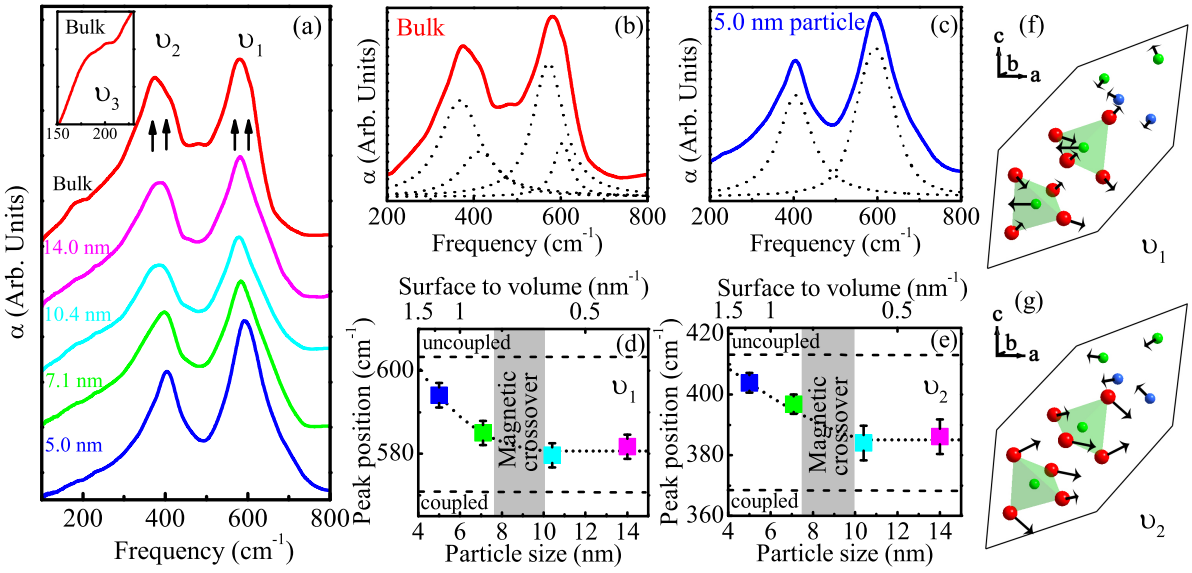

Figure 6.2: (a) 300 K absorption spectra of bulk powder and nanoscale $CoFe_2O_4$. The particle sizes are indicated, and the curves are vertically shifted for clarity. Inset: Close-up view of ν_3 in the bulk powder. (b) Example peak fit of the bulk $CoFe_2O_4$ spectrum using Voigt lineshapes. Two oscillators are required to fit each mode. (c) Example peak fit of the 5.0 nm nanoparticle spectrum using Voigt lineshapes. Only one oscillator is required to fit each mode. (d) and (e) Peak position of ν_1 and ν_2 as a function of particle size. The dashed lines indicate the limiting bulk values with and without spin-phonon coupling, and the dotted lines guide the eye. [4, 74] The gray shaded area indicates the transition regime (from ferrimagnetic at large particle sizes to superparamagnetic at small sizes.) (f) and (g) Schematic view of calculated displacement patterns of ν_1 and ν_2 vibrational modes in $CoFe_2O_4$ in the rhombohedral primitive cell. [104, 160, 210] Here, the shaded green polyhedra denote tetrahedral sites, and top four ions correspond to octahedral positions. [5]

in Chapter 3, the well-known mechanism couples spin to the lattice as [67,68,73,74]

$$\omega^2 = \omega_0^2 + \lambda\langle S_i \cdot S_j \rangle, \tag{6.1}$$

were, we employ a single J Hamiltonian.

Let's apply these ideas to bulk $CoFe_2O_4$. The presence of both coupled and uncoupled components is evidenced by the doublet character of ν_1 and ν_2 (Fig. 6.2(b)). Even ν_3 displays weak splitting (inset Fig. 6.2(a)). [213] A symmetry analysis reveals the origin of the coupled and uncoupled branches and the resultant mode splitting. The displacement patterns of ν_1 and ν_2 (Figs. 6.2(f) and (g)) both show that the tetrahedral A sites have either (i) the same or (ii) zero directional motion. As a consequence, no coupling emanates from the A sublattice in the AB_2O_4 spinel structure. In other words, this branch has no spin-spin correlations. In contrast, ions of the B sublattice (formed by the octahedral metal sites) vibrate against each other. This symmetry is consistent with spin-phonon coupling, and the branch is softened by spin-spin interactions. The inter-sublattice motion also involves out-of-phase vibration and likewise contributes to coupling. The horizontal dashed lines in Figs. 6.2(d) and (e) denote the uncoupled and coupled components of the phonon at higher and lower frequency, respectively. The size of the splitting ($\Delta\omega_{\nu_1} = -32$ cm^{-1} and $\Delta\omega_{\nu_2} = -46$ cm^{-1}) is a measure of the perturbation and is related to the coupling constant for each mode.

Equation 6.1 provides a framework within which we can estimate the spin-phonon coupling constants of ν_1 and ν_2 for bulk $CoFe_2O_4$. We already have the frequency shift from our measured data, [214] but we still need to obtain the spin-spin correlation function. [215] Here, we employ an approximate method that was originally developed for Fe_3O_4. [211,216] It assumes an Ising Hamiltonian, nearest-neighbor interactions, and the two-sublattice ferrimagnetic model. [211,216] Under these assumptions, we

can write $\langle S_i \cdot S_j \rangle = \sum S_{Bi} \cdot S_{Bj} - \sum S_{Ai} \cdot S_{Bj}$ for a single formula unit. Here, S_{Ai} denotes the spin at the A sublattice site, and S_{Bi} denotes the spin at the B sublattice site. In the case of a fully inverted spinel with formula AB_2O_4, Fe^{3+} ions occupy the A sublattice (tetrahedral) sites and half of the B sublattice (octahedral) sites, Co^{2+} ions occupy the remaining B sublattice sites. $S = \frac{5}{2}$ for Fe^{3+} and $S = \frac{3}{2}$ for Co^{2+} in agreement with the electronic configurations of these ions. As mentioned above, no coupling emanates from the A sublattice sites in the AB_2O_4 spinel structure. Then the calculation of $\langle S_i \cdot S_j \rangle$ only runs over the B sublattice and the inter-sublattice. The spin-spin correlation function $\langle S_i \cdot S_j \rangle = \sum S_{Bi} \cdot S_{Bj} - \sum S_{Ai} \cdot S_{Bj}$ for a single formula unit. Here, S_{Ai} denotes the spin at the A sublattice site, and S_{Bi} denotes the spin at the B sublattice site, and the minus sign indicates antiferromagnetic alignment between inter-sublattice. As shown in Fig. 3.8 (b), there are 6 nearest neighbors for B sublattice ions (Fe^{3+} and Co^{2+}), $\sum S_{Bi} \cdot S_{Bj} = \frac{1}{2}((2 \cdot \frac{3}{2} \cdot \frac{3}{2} + 4 \cdot \frac{5}{2} \cdot \frac{3}{2}) + (2 \cdot \frac{5}{2} \cdot \frac{5}{2} + 4 \cdot \frac{5}{2} \cdot \frac{3}{2})) = \frac{47}{2}$; there are 12 nearest neighbors for inter-sublattice ions, $\sum S_{Ai} \cdot S_{Bj} = \frac{1}{2}(6 \cdot \frac{5}{2} \cdot \frac{5}{2} + 6 \cdot \frac{5}{2} \cdot \frac{3}{2}) = 30$. Here, the factor of $\frac{1}{2}$ avoids double-counting issues. Thus $\langle S_i \cdot S_j \rangle = \frac{47}{2} - 30 = -\frac{13}{2}$ for a fully inverted spinel. Combining this value of the spin-spin correlation function with the experimentally measured frequency shifts, we find $J'' = \lambda \cdot \mu \approx 1.1$ N/m for the fully inverted spinel.

Most spinels, however, exhibit an inversion fraction between 0 and 1. Ferreira *et al.* determined the cation distribution of bulk $CoFe_2O_4$ from powder x-ray diffraction and Mössbauer data and found that the degree of inversion is $\delta = 0.75 \pm 0.01$. The corresponding chemical formula is thus $(Co^{2+}_{0.25}Fe^{3+}_{0.75})(Co^{2+}_{0.75}Fe^{3+}_{1.25})O_4$. [217, 218] Note that oxidation state does not change with occupancy. [132] Based on this stoichiometry, we can recalculate $\langle S_i \cdot S_j \rangle$. First, for a normal (non-inverted) spinel, $\sum S_{Bi} \cdot S_{Bj} = \frac{1}{2}(6 \cdot \frac{5}{2} \cdot \frac{5}{2} \cdot 2) = \frac{75}{2}$ for the B sublattice; $\sum S_{Ai} \cdot S_{Bj} = \frac{1}{2}(12 \cdot \frac{5}{2} \cdot \frac{3}{2}) = \frac{45}{2}$. Using the above fully inverse results, we can estimate $\langle S_i \cdot S_j \rangle$ for bulk $CoFe_2O_4$ as

$0.75 \cdot (\frac{47}{2} - 30) + 0.25 \cdot (\frac{75}{2} - \frac{45}{2}) = -\frac{9}{8}$. Combining this value of $\langle S_i \cdot S_j \rangle$ with the experimentally measured frequency shifts, [214] we can roughly estimate the coupling constant of both modes as $J'' = \lambda \cdot \mu \approx 6.3$ N/m. In this calculation, we employed $\langle S_i \cdot S_j \rangle$ for the partially inverted spinel because it most closely resembles the situation in bulk $CoFe_2O_4$. The error bars are large (probably ± 1 or 2 N/m), mainly due to uncertainties in $\langle S_i \cdot S_j \rangle$. On the other hand, the extracted coupling constant of the partially inverse spinel ($J'' = \lambda \cdot \mu \approx 6.3$ N/m) is similar to the values found in other oxides like MnO and $ZnCr_2O_4$. [4, 68, 75, 219]

6.3 Spin-Phonon Coupling in $CoFe_2O_4$ Nanoparticles

We also employed standard peak-fitting techniques to reveal size-dependent trends in the position of ν_1 and ν_2. [220] The line shapes in the various nanoparticle samples are much more symmetric than that of the bulk due to the short phonon lifetime and fast magnetic relaxation time. [4, 110, 164, 207, 208, 221, 222] As a result, only one oscillator is needed to fit each mode (Fig. 6.2(c)). Figures 6.2(d) and (e) summarize the behavior of ν_1 and ν_2 as a function of nanoparticle size. The resonance frequencies increase with decreasing size through the magnetic crossover regime. This trend parallels the diverging surface-to-volume ratio (Fig. 6.1) and suggests a correlation with the transition to the superparamagnetic state and the development of surface spin disorder. [204] This connection is discussed below. As anticipated, the data points are positioned between the low and high frequency limits defined by coupled and uncoupled branches of each phonon in the bulk.

Spin-phonon coupling in the $CoFe_2O_4$ nanoparticles is different than in the bulk. This is because robust magnetic order exists primarily in the core, whereas the shell

has a more random spin arrangement. [204] Magnetoelastic coupling is therefore different in the two regions. Interestingly, infrared spectroscopy is sensitive to this change. Although there is no splitting of ν_1 and ν_2 (Fig 6.2(a)), these features still carry information on the coupling in an average way that causes peak positions to shift with decreasing particle size. Of course, it is not really particle size that matters here but the relative proportion of core and shell. The core-shell model (where we assume that the particle consists of a core of aligned spins surrounded by a magnetically disordered shell) [204] accounts for these effects. We consider each region in turn and then bring them together.

In the core of a single-domain nanoparticle like $CoFe_2O_4$, [134] spins align ferrimagnetically according to their various exchange interactions, [204, 223] a process that mirrors the development of magnetic order in the bulk. Phonons that reside primarily in the core are sensitive to this magnetic structure, and they engage in spin-phonon coupling just like the bulk. Core-phonon modes thus possess both coupled and uncoupled branches, as previously discussed, although confinement effects reduce the phonon life time [4, 110, 208, 221] to yield only an averaged spectral response. This occurs because the phonon lifetime ($10^{-14} - 10^{-13}$ sec) is shorter than spectroscopic time scale ($10^{-12} - 10^{-13}$ sec), [222] so the spectrum will measure multiple phonon vibrations in the same time period which eliminates the possibility of distinguishing between coupled and uncoupled branches. [4, 110, 208, 221]

The surface of a magnetic nanoparticle is different. Here, large surface strains, broken bonds, and broken exchange interactions between magnetic centers cause surface spins to lose their order. [204, 223] Under these conditions, the spin-spin correlation function $\langle S_i \cdot S_j \rangle$ will be close to zero. Since $\omega^2 = \omega_0^2 + \lambda \langle S_i \cdot S_j \rangle$, the vibrational contribution of the nanoparticle shell will thus be a peak at the unperturbed phonon frequency, ω_0, regardless of the value of λ. In other words,

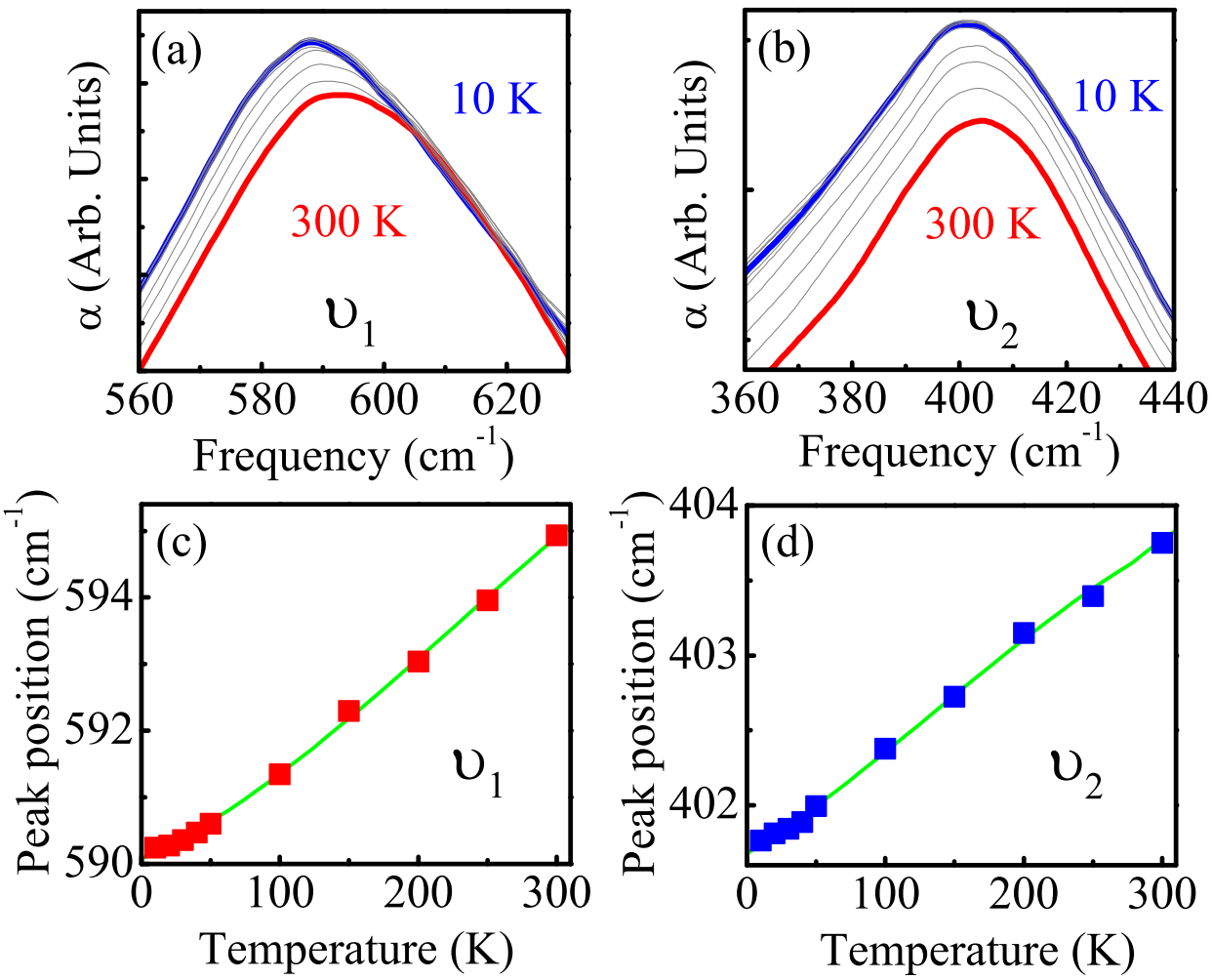

Figure 6.3: (a) and (b) Variable temperature infrared absorption spectra of ν_1 and ν_2 from the 5 nm particles. (c) and (d) Peak position of ν_1 and ν_2 as a function of temperature. [5]

there can be no coupling without spin order.

Variable temperature infrared spectroscopy provides an additional test for the presence of surface spin disorder at high temperature and the possibility of a low temperature surface spin glass state. [204, 223] Figures 6.3(a) and (b) shows a close-up view of the variable temperature infrared absorption spectra of the 5 nm particles focusing on ν_1 and ν_2 behavior. We employed standard peak-fitting techniques to reveal size-dependent trends in the position of ν_1 and ν_2 as shown in Figs. 6.3(c) and (d). [220] Our experiments show a gradual red-shift of the peak positions with

decreasing temperature (on the order of 5 cm^{-1} for ν_1 and 2 cm^{-1} for ν_1). This red-shift is a temperature-dependent property of the material. Importantly, there is no abrupt change in behavior at the blocking temperature (245 K). In the above text, we discussed how phonon frequency is determined by $\omega^2 = \omega_0^2 + \lambda\langle S_i \cdot S_j \rangle$. Eliminating the temperature dependence, this result indicates the surface spin correlation function $\langle S_i \cdot S_j \rangle$ is still close to zero at low temperature. In other words, the surface spins are still disordered, which is consistent with low temperature magnetization behavior determined by a random freezing of surface spins. [224]

Let's bring the behavior of the core and shell together. We already argued that the spectrum of the nanoparticles catches only the weighted average value of the coupled and uncoupled branches of each mode due to the short phonon lifetime and fast magnetic relaxation time. [4, 110, 164, 207, 208, 221] This averaged response can be expressed as $\omega_{ave} = x\omega_{shell} + (1-x)\omega_{core}$. Here, ω_{ave} is the weighted average frequency, x is the volume fraction of the shell, $(1-x)$ is the volume fraction of the core, and ω_{core} and ω_{shell} are the core and shell phonon frequencies, respectively. Moreover, ω_{core} is always less than ω_{shell} because the core includes the coupled branch contribution whereas the shell does not. If we assume that ω_{core} and ω_{shell} do not change with size over the range of our investigation, larger values of x will shift the observed peak at ω_{ave} to higher frequency. This is in agreement with the data in Figs. 6.2(d) and (e), and it provides a natural explanation for the similarity between these trends and the surface-to-volume ratio in Fig. 6.1. As shown in Figs. 6.2(d) and (e), the peak position of the 7.1 nm particles is elevated compared to that of the larger particles, and ω_{ave} of the 5.0 nm particles is approaching the bare phonon frequency of the bulk. Moreover, both the 5 and 7 nm particles are in the superparamagnetic state under these conditions. The spectral sensitivity to the superparamagnetic transition in these ferrimagnetic spinel nanoparticles is thus due to magnetoelastic coupling

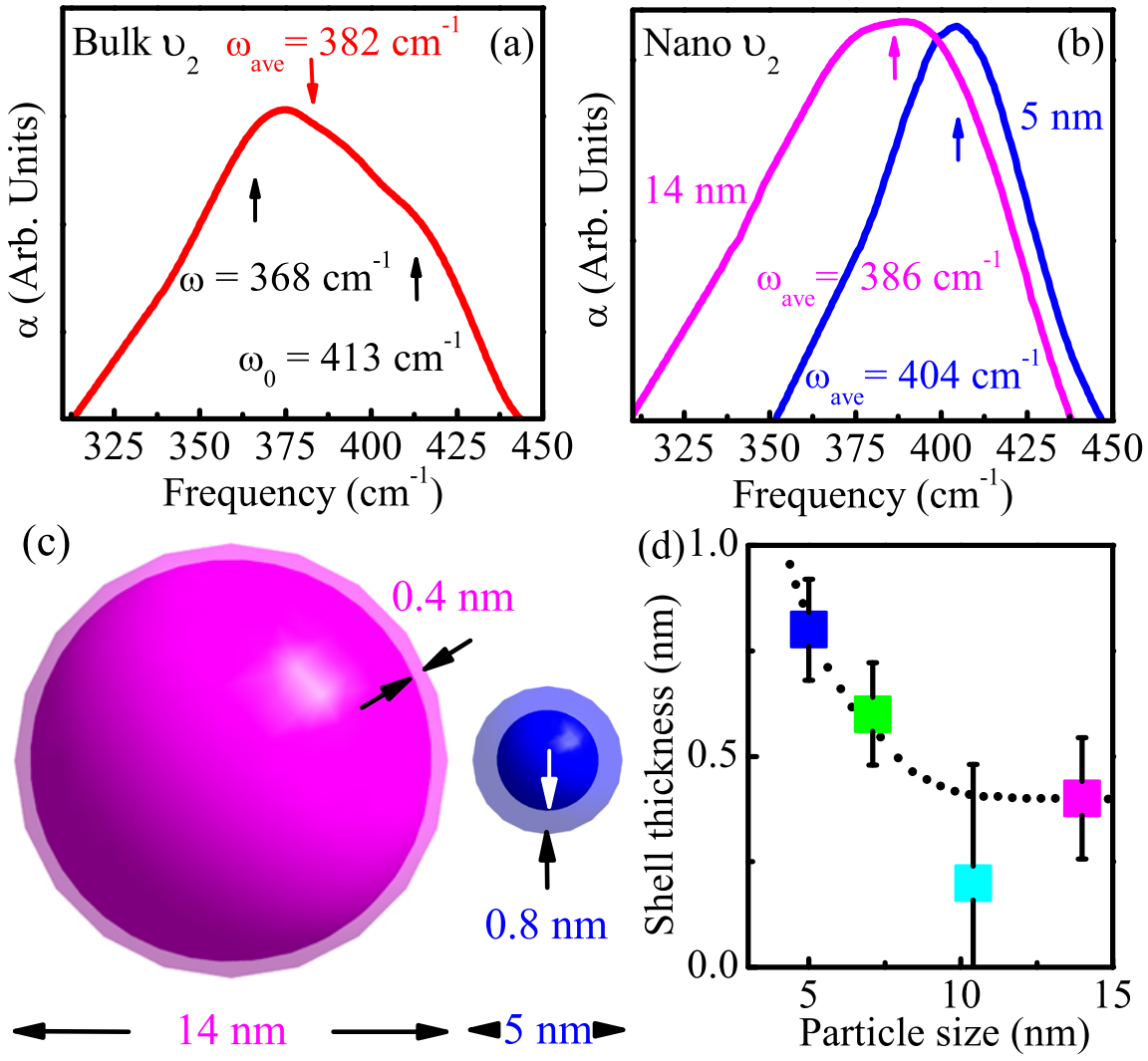

Figure 6.4: (a) Close-up view of the ν_2 vibrational mode of bulk $CoFe_2O_4$ where ω and ω_0 are clearly resolved due to magnetoelastic coupling. The weighted average position of the coupled and uncoupled branches, ω_{ave}, is also indicated. (b) Close-up view of ν_2 for the 14 and 5 nm particles where the spectral peak represents the weighted average of the coupled and uncoupled branches. In other words, ω and ω_0 are smeared together due to lifetime effects, and only ω_{ave} is observed. (c) Schematic view of our findings from the core-shell model for the 14 and 5 nm particles, respectively. The extracted shell thicknesses of 0.4 and 0.8 nm are comparable with the 0.8391 nm unit cell size [159] for bulk $CoFe_2O_4$. (d) Shell thickness as a function of particle size determined by a spin-phonon coupling analysis. The dotted line guides the eye. [5]

(with a boundary at $\sim 0.5(\omega_0 + \omega)$ of bulk values estimated from Figs. 6.2(d) and (e)). Moreover, the core-shell model captures the physics of this situation extremely well.

6.4 Using Vibrational Spectroscopy to Estimate Shell Thickness

We can also employ our spectral data to estimate the relative size of the core and shell. Here's how. First, we calculate the weighted average phonon frequencies of ν_1 and ν_2 for the bulk material. This is done using peak-fitted mode positions and the normalized areas of the coupled and uncoupled components. Using ν_2 as an example, the weighted average frequency can be written as $\omega_{ave} = y\omega + (1-y)\omega_0$. The factors of y (0.69) and $(1-y)$ (0.31) are the normalized areas of the coupled ($\omega = 368$ cm^{-1}) and uncoupled ($\omega_0 = 413$ cm^{-1}) branches of ν_2 in the bulk (Fig. 6.4(a)). We find ω_{ave} $= 382$ cm^{-1}. This number rigorously describes the bulk and reasonably approximates the nanoparticle core. We further fix the core phonon frequency in our set of 14, 10, 7, and 5 nm particles to be that of the bulk. In other words, we assume that this value ($\omega_{ave} = 382$ cm^{-1}) does not depend on size. Lastly, we also allow the shell phonon to be represented by the uncoupled phonon in the bulk, an assumption that is justified because $\langle S_i \cdot S_j \rangle \approx 0$. Using the weighted average phonon frequency of the 5 nm particles from the measured spectrum ($\omega_{ave} = 404$ cm^{-1}, Fig. 6.4(b)) and our expression for the overall average response $\omega_{ave} = x\omega_{shell} + (1-x)\omega_{core}$, we can back calculate the volume fraction of the shell. We find $x = 0.71$ for the 5 nm particles. An analysis of ν_1 yields a similar value ($x = 0.63$). Using the average of these two quantities ($x = 0.67$), we can estimate the shell thickness as $x = (\frac{4}{3}\pi R^3 - \frac{4}{3}\pi r^3)/\frac{4}{3}\pi R^3$. Here, R is the nanoparticle radius, and r is the radius of the core. We find $r = 1.7$

nm for the 5 nm particles. The shell thickness is therefore 2.5 - 1.7 = 0.8 nm. A similar analysis of the 14 nm particles yields an 0.4 nm shell thickness. Table 6.1 summarizes our work to estimate shell thicknesses for different sized nanoparticles based on a spin-phonon coupling analysis. The extracted shell thicknesses of 0.4 and 0.8 nm for the 14 and 5 nm particles are comparable with the 0.8391 nm unit cell size for bulk $CoFe_2O_4$. [159] We therefore conclude that the surface distortion takes place within the outermost unit cell, a finding that is consistent with other length scale estimates of spin disorder. [204, 224–226] The deviation of the 10.4 nm particles is probably related to their broader size distribution and lesser overall quality.

Table 6.1: Summary of the shell thicknesses for different sized nanoparticles based on the detailed spin-phonon coupling analysis. We retain only one significant figure in the shell thickness numbers due to the size of the error bars. [5, 227]

Particles size (nm)	Mode	Peak position (cm^{-1})	Volume fraction of shell (x)	Shell thickness (nm)
5.0	ν_1 ν_2	594 404	0.63 0.71	0.76±0.12 (∼0.8)
7.1	ν_1 ν_2	585 397	0.30 0.48	0.55±0.12 (∼0.6)
10.4	ν_1 ν_2	580 384	0.11 0.065	0.15±0.28 (∼0.2)
14.0	ν_1 ν_2	582 386	0.19 0.13	0.40±0.14 (∼0.4)

Figure 6.4(c) displays a schematic view of the 14 and 5 nm $CoFe_2O_4$ particles

within the core-shell picture. Shell thickness is clearly not a constant. Instead, it increases from 0.4 to 0.8 nm over the range of our investigation. We can see this result more clearly in Fig. 6.4(d). While the 1.2 nm shell thickness in the 4 nm particles investigated by Lin *et al.* [223] is not strictly comparable with our data because the particles were prepared by mechanical agitation rather than the synthetic techniques employed here, [100, 125] the trend is strikingly preserved. In any case, the inverse relationship between shell thickness and particle size emanates from the large surface strains that introduce broken bonds (and interrupted exchange interactions between magnetic centers) in the small nanoparticles. We conclude that the large proportion of surface spin disorder in the small $CoFe_2O_4$ particles is responsible for the crossover to the superparamagnetic state.

Chapter 7

Conclusion

In this work, I investigated the infrared vibrational properties of nanoscale MoS_2, MnO, and $CoFe_2O_4$ and compared the results with the spectrum of their parent compounds in order to understand finite length scale effects. Work focused on the charge and bonding analysis which investigates charge, bonding, ionicity, and polarizability in nanoscale materials, and spin-phonon coupling which reveal the interplay between charge, structure, and spin in nanoscale systems.

Infrared vibrational spectroscopy provides a unique microscopic probe of charge, bonding, and spin interactions present in a nanomaterial. For MoS_2, we find that the intralayer Born effective charge decreases strongly in IF-MoS_2 compared to the 2H-counterpart whereas it remains unchanged in the interlayer direction. Comparison with local effective charge and polarizability demonstrates that this decrease is due to structural strain and the consequent modification of the intralayer polarizability that reduces non-local effective charge in the nanoscale material. These findings are important because they strengthen the connection between structural strain, phonon confinement, and charge, which may play a role in the unique solid state lubrication behavior in the nanomaterial.

For MnO, we employ the charge and bonding analysis and the magneto-elastic

coupling analysis to evaluate finite length scale effects in 8 nm MnO particles. The charge and bonding analysis reveals a dramatic decrease in the Born effective charge of the nanoparticles compared with the single crystal, a finding that, when separated into local charge and polarizability contributions, shows that the nanoparticles are less ionic than bulk MnO. Magnetoelastic interactions through the Néel temperature are substantial in the bulk material (with a coupling constant of $\sim$5 N/m), whereas they are much smaller in the nanoparticles. In fact, the displacive contribution is nearly blocked. These findings are important for understanding finite length scale effects in this simple binary oxide and the more complicated functional oxides that emanate from this parent compound.

For $CoFe_2O_4$, we measured the infrared vibrational properties of several different $CoFe_2O_4$ nanoparticles and compared the results to trends in the coercivity and to the spectrum of the bulk material. A detailed analysis of the magnetoelastic coupling allows us to extract a spin-phonon coupling constant of $\sim$6.3 N/m for the bulk. Moreover, we show that these same processes are sensitive to the size-dependent crossover in magnetic properties (in which the nanoparticles become superparamagnetic between 7 and 10 nm). In other words, magnetoelastic coupling in the confined system makes the mode position sensitive to the superparamagnetic transition. Combining this mode information with a spin-phonon coupling analysis reveals the applicability of the core-shell model with a core of aligned spins surrounded by a magnetically disordered shell. We use this model to evaluate the shell thickness and find that it is on the order of 1 unit cell. It increases from 0.4 nm in our 14 nm particles to 0.8 nm in the 5 nm particles. These findings are unique in that they verify the core-shell model from the spectroscopic point of view.

This dissertation opens up an interesting new direction for spectroscopic studies of charge, bonding, and spin-phonon coupling in nanomaterials. Our analysis re-

veals that the properties of nanoscale materials are quite different from those of the corresponding bulk materials. From the analysis of effective charges, polarizability and spin phonon coupling constant, we can understand the ionicity, covalence, and spin pattern in nanoscale materials. These findings are important for understanding finite length scale effects in these model nanoscale materials and the more complicated functional nanoscale materials that emanate from similar parent compounds. These ideas may also be interesting consequences for on-going work to functionalize and design nanoscale devices.

Bibliography

Bibliography

[1] Q. -C. Sun, X. S. Xu, L. I. Vergara, R. Rosentsveig, and J. L. Musfeldt. Phys. Rev. B **79**, 205405 (2009).

[2] X. S. Xu, Q.-C. Sun, S. Rosentsveig, and J.L. Musfeldt, Phys. Rev. B **80**, 014303 (2009).

[3] Q. -C. Sun, X. S. Xu, S. N. Baker, A. D. Christianson, and J. L. Musfeldt, Chem. Mater. **23**, 2956 (2011).

[4] Q. -C. Sun, S. N. Baker, A. D. Christianson, and J. L. Musfeldt, Phys. Rev. B **84**, 014301 (2011).

[5] Q. -C. Sun, C. S. Birkel, J. Cao, W. Tremel, and J. L. Musfeldt, ACS Nano **6**, 4876 (2012).

[6] T. L. Brown, H. E. LeMay, Jr., B. E. Bursten, C. J. Murphy, P. Woodward, *Chemistry: The Central Science* (Prentice Hall, New York, 2008).

[7] C. Kittel, *Introduction to solid state physics* (Wiley, New York, 2004).

[8] N. W. Ashcroft and N. D. Mermin, *Solid State Physics* (Thomson Learning, New York, 1976).

[9] M. Stefanov, A. N. Enyashin, T. Heine, and G. Seifert, J. Phys. Chem. C. **112**, 17764 (2008).

[10] Resta, R.; Posternak, M.; Baldereschi, A. Towards a Quantum Theory of Polarization in Ferroelectrics: The Case of $KNbO_3$. *Phys. Rev. Lett.* **1993**, *70*, 1010-1013.

[11] Homes, C. C.; Vogt, T.; Shapiro, S. M.; Wakimoto, S.; Ramirez, A. P. Optical Response of High-Dielectric-Constant Perovskite-Related Oxide. *Science* **2001**, *293*, 673-676.

[12] Lucovsky, G.; Martin, R. M.; Burstein, E. Localized Effective Charges in Diatomic Crystals. *Phys. Rev. B* **1971**, *4*, 13671374.

[13] T. J. Wieting and J. L. Verble, Phys. Rev. B **3**, 4286 (1971).

[14] S. I. Uchida and S. Tanaka, J. Phys. Soc. Jpn. **45**, 153 (1978).

[15] G. Lucovsky, R. M. White, J. A. Benda, and J. F. Revelli, Phys. Rev. B **7**, 3859 (1973).

[16] J. N. Plendl, L. C. Mansur, S. S. Mitra, and I. F. Chang, Sol. St. Commun. **7**, 109 (1969).

[17] S. Mochizuki, J. Phys.: Cond. Mat. **1**, 10351 (1989).

[18] T. Rudolf, Ch. Kant, F. Mayr, and A. Loidl, Phys. Rev. B **77**, 024421 (2008).

[19] S. Y. Savrasov and G. Kotliar, Phys. Rev. Lett. **90**, 056401 (2003).

[20] A. Roy, R. Prasad, S. Auluck, and A. Garg, Journal of Physics-Condensed Matter 22, 165902 (2010).

[21] H. Wang, B. Wang, Q. Li, Z. Zhu, R. Wang, and C. H. Woo, Phys. Rev. B 75, 245209 (2007).

[22] N. Choudhury, R. E. Cohen, and E. J. Walter, Computational Materials Science 37, 152 (2006).

[23] S. Massidda, M. Posternak, A. Baldereschi, and R. Resta, Phys. Rev. Lett. **82**, 430 (1999).

[24] U. D. Wdowik and D. Legut, J. Phys.: Cond. Mat. **21**, 275402 (2009).

[25] A. R. Lansdown, *Molybdenum Disulphide Lubrication*, (Elsevier Science, New York, 1999).

[26] E. Dagotto, *Nanoscale Phase Separation and Colossal Magneto-resistance: the Physics of Manganites and Related Compounds* (Springer, Berlin, 2003).

[27] M. Born and K. Huang, *Dynamical Theory of Crystal Lattices* (Oxford University Press, London, 1954).

[28] B. C. Haywood and M. F. Collins, J. Phys. C.: Sol. St. Phys. **4**, 1299 (1971).

[29] R. Tenne, L. Margulis, M. Genut, and G. Hodes, Nature **360**, 444 (1992).

[30] L. Margulis, G. Salitra, R. Tenne, and M. Talianker, Nature **365**, 113 (1993).

[31] G.H. Lee, S. H. Huh, J. W. Jeong, B. J. Choi, S. H. Kim, and H.-C. Ri, J. Am. Chem. Soc. **124**, 12094 (2002).

[32] W. S. Seo, H. H. Jo, K. Lee, B. Kim, S. J. Oh, and J. T. Park, Angew. Chem. Int. Ed. **43**, 1115 (2004).

[33] M. Ghosh, K. Biswas, A. Sundaresana, and C. N. R. Rao, J. Mater. Chem. **16**, 106 (2006).

[34] M. A. Morales, R. Skomski, S. Fritz, G. Shelburne, J. E. Shield, M. Yin, S. O'Brien, and D. L. Leslie-Pelecky, Phys. Rev. B **75**, 134423 (2007).

[35] T. D. Schladt, T. Graf, and W. Tremel, Chem. Mater. **21**, 3183 (2009).

[36] T. Ould-Ely, D. Prieto-Centurion, A. Kumar, W. Guo, W. V. Knowles, S. Asokan, M. S. Wong, I. Rusakova, A. Luttge, and K. H. Whitmire, Chem. Mater., **18**, 1821 (2006).

[37] A. Zak, Y. Feldman, V. Alperovich, R. Rosentsveig, and R. Tenne, J. Am. Chem. Soc. **122**, 11108 (2000).

[38] Y. Feldman, E. Wasserman, D. J. Srolovitz, and R. Tenne, Science **267**, 222 (1995).

[39] M. Remskar, A. Mrzel, Z. Skraba, A. Jesih, M. Ceh, J. Demšar, P. Stadelmann, F. lévy, and D. Mihailovic, Science **292**, 479(2001).

[40] R. Rosentsveig, A. Margolin, Y. Feldman, R. Popovitz-Biro, and R. Tenne, Chem. Mater. **14**, 471 (2002).

[41] R. Tenne, Nature Nanotechnology **1**, 103 (2006).

[42] L. Rapoport, Y. Bilik, Y. Feldman, M. Homyonfer, S. R. Cohen, and R. Tenne, Nature **387**, 791 (1997).

[43] G. Seifert, H. Terrones, M. Terrones, G. Jungnickel, and T. Frauenheim, Phys. Rev. Lett. **85**, 146 (2000).

[44] A. Albu-Yaron, T. Arad, R. Popovitz-Biro, M. Bar-Sadan, Y. Prior, M. Jansen, and R. Tenne, Angew. Chem. Int. Ed. **44**, 4169 (2005).

[45] M. Remkar, A. Mrzel, M. Virek, and A. Jesih, Adv. Mater. **19**, 4276 (2007).

[46] J. W. Long and D. R. Rolison, Acc. Chem. Res. **40**, 854 (2007).

[47] B. Poudel, Q. Hao, Y. Ma, Y. C. Lan, A. Minnich, B. Yu, X. Yan, D. Z. Wang, A. Muto, D. Vashaee, X. Y. Chen, J. M. Liu, M. S. Dresselhaus, G. Chen, and Z. F. Ren, Science **320**, 634 (2008).

[48] S. Y. Quek, M. M. Biener, J. Biener, J. Bhattacharjee, C. M. Friend, U. V. Waghmare, and E. Kaxiras, J. Chem. Phys. **127**, 104704 (2007).

[49] X. G. Peng, L. Manna, W. D. Yang, J. Wickham, E. Scher, A. Kadavanich, and A. P. Alivisatos, Nature **404**, 59 (2000).

[50] V. F. Puntes, K. M. Krishnan, and A. P. Alivisatos, Science **291**, 2115 (2001).

[51] S. Brown, J. L. Musfeldt, I. Mihut, J. B. Betts, A. Migliori, A. Zak, and R. Tenne, Nano Lett. **7**, 2365 (2007).

[52] C. C. Li, K. L. Shuford, Q. H. Park, W. P. Cai, Y. Li, E. J. Lee, and S. O. Cho, Angew. Chem. Int. Ed. **46**, 3264 (2007).

[53] M. Okubo, E. Hosono, J. Kim, M. Enomoto, N. Kojima, T. Kudo, H. S. Zhou, and I. Honma, J. Am. Chem. Soc. **129**, 7444 (2007).

[54] I. Rusakova, T. Ould-Ely, C. Hofmann, D. Prieto-Centurion, C. S. Levin, N. J. Halas, A. Luttge, and K. H. Whitmire, Chem. Mater. **19**, 1369 (2007).

[55] C. Y. Lee and X. Gonze, Phys. Rev. Lett. **72**, 1686 (1994).

[56] T. Kimura and Y. Tokura, Annu. Rev. Mater. Sci. **30**, 451 (2000).

[57] Y. Tokura and S. Seki, Adv. Mater. **22**, 1554 (2010).

[58] O. Tchernyshyov, R. Mossner, and S. L. Sondhi, Phys. Rev. B **66**, 064403 (2002).

[59] M. Fiebig, J. Phys. D: Appl. Phys. **38**, R123 (2005).

[60] J. Kunes, A. V. Lukoyanov, V. I. Anisimov, R. T. Scalettar and W. E. Pickett, Nat. Mater. **7**, 198 (2008).

[61] K. B. Chetry, M. Pathak, P. LeClair and A. Gupta, J. Appl. Phys. **105**, 083925 (2009).

[62] N. Ray and U. V. Waghmare, Phys. Rev. B **77**, 134112 (2008).

[63] S. Petit, F. Moussa, M. Hennion, S. Pailhes, L. Pinsard-Gaudart and A. Ivanov, Phys. Rev. Lett. **99**, 266604 (2007).

[64] B. Lake, D. A. Tennant, C. D. Frost and S. E. Nagler, Nat. Mater. **4**, 329 (2005).

[65] J. L. Musfeldt, L. I. Vergara, T.V. Brinzari, C. Lee, L. C. Tung, J. Kang, Y. J. Wang, J. A. Schlueter, J. L. Manson, and M.-H. Whangbo, Phys. Rev. Lett. **103**, 157401 (2009).

[66] J. S. Gardner, M. J. P. Gingras and J. E. Greedan, Rev. Mod. Phys. **82**, 53 (2010).

[67] J. H. Lee, L. Fang, E. Vlahos, X. L. Ke, Y. W. Jung, L. F. Kourkoutis, J. W. Kim, P. J. Ryan, T. Heeg, M. Roeckerath, V. Goian, M. Bernhagen, R. Uecker, P. C. Hammel, K. M. Rabe, S. Kamba, J. Schubert, J. W. Freeland, D. A. Muller, C. J. Fennie, P. Schiffer, V. Gopalan, E. Johnston-Halperin, and D. G. Schlom, Nature **466**, 954 (2010).

[68] C. J. Fennie and K. M. Rabe, Phys. Rev. Lett. **96**, 205505 (2006).

[69] J. L. Musfeldt, Z. Liu, S. Li, J. Kang, C. Lee, P. Jena, J. L. Manson, J. A. Schlueter, G. L. Carr, M. H. Whangbo, Inorg. Chem. **50**, 6347 (2011).

[70] L. I. Vergara, J. Cao, N. Rogado, Y. Q. Wang, R. P. Chaudhury, R. J. Cava, B. Lorenz, and J. L. Musfeldt, Phys. Rev. B **80**, 052303 (2009).

[71] J. Cao, L. I. Vergara, J. L. Musfeldt, A. P. Litvinchuk, Y. J. Wang, S. Park, and S.-W. Cheong, Phys. Rev. B **78**, 064307 (2008).

[72] M. Kim, X. M. Chen, Y. I. Joe, E. Fradkin, P. Abbamonte, and S. L. Cooper, Phys. Rev. Lett. **104**, 136402 (2010).

[73] D. J. Lockwood and M. G. Cottam, J. Appl. Phys. **64**, 5876 (1988).

[74] W. Luo, P. Zhang, and M. L. Cohen, Sol. St. Commun. **142**, 504 (2007).

[75] A. B. Sushkov, O. Tchernyshyov, W. Ratcliff II, S.W. Cheong, and H. D. Drew, Phys. Rev. Lett. **94**, 137202 (2005).

[76] A. Earnshaw and N. Greenwood, *Chemistry of the Elements, Second Edition* (Elsevier, New York, 2005).

[77] Y. Tokura, *Colossal Magnetoresistive Oxides*, (Gordon and Breach Science Publishers, New York, 2000).

[78] C. C. Homes, S. V. Dordevic, G. D. Gu, Q. Li, T. Valla, and J. M. Tranquada, Phys. Rev. Lett. **96**, 257002 (2006).

[79] J. Cao, L. I. Vergara, J. L. Musfeldt, A. P. Litvinchuk, Y. J. Wang, S. Park, and S. W. Cheong, Phys. Rev. Lett. **100**, 177205 (2008).

[80] J. L. Musfeldt, K. Kamaras, and D. B. Tanner, Phys. Rev. B **45**, 10197 (1992).

[81] T. Yamamoto, M. Uruichi, K. Yamamoto, K. Yakushi, A. Kawamoto, and H. Taniguchi, J. Phys. Chem. B **109**, 15226 (2005).

[82] M. Kim, H. Barath, S. L. Cooper, P. Abbamonte, E. Fradkin, M. Ruebhausen, C. L. Zhang, and S. W. Cheong, Phys. Rev. B **77**, 134411 (2008).

[83] X. S. Xu, J. de Groot, Q. C. Sun, B. C. Sales, D. Mandrus, M. Angst, A. P. Litvinchuk, and J. L. Musfeldt, Phys. Rev. B **82**, 014304 (2010).

[84] M. Hase, I. Terasaki, and K. Uchinokura, Phys. Rev. Lett. **70**, 3651 (1993).

[85] L. V. Gasparov, D. B. Tanner, D. B. Romero, H. Berger, G. Margaritondo, and L. Forro, Phys. Rev. B **62**, 7939 (2000).

[86] R. V. Aguilar, A. B. Sushkov, Y. J. Choi, S. W. Cheong, and H. D. Drew, Phys. Rev. B **77**, 092412 (2008).

[87] S. Lee, A. Pirogov, M. Kang, K.-H. Jang, M. Yonemura, T. Kamiyama, S. W. Cheong, F. Gozzo, N. Shin, H. Kimura, Y. Noda, and J. G. Park, Nature **451**, 805 (2008).

[88] R. Schleck, R. L. Moreira, H. Sakata, and R. Lobo, Phys. Rev. B **82**, 144309 (2010).

[89] C. J. Fennie and K. M. Rabe, Phys. Rev. Lett. **97**, 267602 (2006).

[90] S. K. Nayak and P. Jena, Phys. Rev. Lett. **81**, 2970 (1998).

[91] A. Jaiswal, R. Das, T. Maity, K. Vivekanand, S. Adyanthaya and P. Poddar, J Phys. Chem. C **114**, 12432 (2010).

[92] C. -H. Hung, P. -H. Shih, F. -Y. Wu, W. -H. Li, S. Y. Wu, T. S. Chan, H. -S. Sheu, J Nanosci. Nanotech. **10**, 4596 (2010).

[93] C. H. Wang, S. N. Baker, M. D. Lumsden, S. E. Nagler, W. T. Heller, G. A. Baker, P. Deen, L. Cranswick, Y. Su, and A. D. Christianson, Phys. Rev. B. **83**, 214418 (2011).

[94] F. Krumeich, H.-J. Muhr, M. Niederberger, F. Bieri, B. Schnyder, and R. Nesper, J. Am. Chem. Soc. **121**, 8324 (1999).

[95] H. -J. Muhr, F. Krumeich, U. P. Schönholzer, F. Bieri, M. Niederberger, L. J. Gauckler, and R. Nesper, Adv. Mater. **12**, 231 (2000)

[96] X. Y. Zhang, C. W. Lai, X. Zhao, D. Y. Wang, and J. Y. Dai, Appl. Phys. Lett. **87**, 143102 (2005).

[97] R. Skomski, J. Phys.: Condens. Matter **15**, 841 (2003).

[98] J. X. Ma, D. Mazumdar, G. Kim, H. Sato, N. Z. Bao, and A. Gupta, J. Appl. Phys. **108**, 063917 (2010).

[99] M. I. Shukoor, F. Natalio, N. Metz, N. Glube, M. N. Tahir, H. A. Therese, V. Ksenofontov, P. Theato, P. Langguth, J.-P. Boissel, H. C. Schroeder, W. E. G. Mueller, and W. Tremel, Angew. Chem. Int. Ed. **47**, 4748 (2008).

[100] S. H. Sun, H. Zeng, D. B. Robinson, S. Raoux, P. M. Rice, S. X. Wang, and G. X. Li, J. Am. Chem. Soc. **126**, 273 (2004).

[101] C. N. R. Rao and C.N.R. Rao, *Transition Metal Oxides* (Wiley-VCH, New York, 1995).

[102] M. S. Seehra, R. E. Helmick, and G. Srinivasan, J. Phys. C: Solid State Phys, **19**, 1627 (1986).

[103] J. Teillet, F. Bouree, and R. Krishnan, J. Magn. Magn. Mater. **123**, 93 (1993).

[104] R. D. Waldron, Phys. Rev. **99**, 1727 (1955).

[105] J. E. Pask, D. J. Singh, I. I. Mazin, C. S. Hellberg, and J. Kortus, Phys. Rev. B **64**, 024403 (2001).

[106] B. Morosin, Phys. Rev. B **1**, 236 (1970).

[107] R.-Q. Song, A.-W. Xu, and S.-H. Yu, J. Am. Chem. Soc. **129**, 4152 (2007).

[108] B. Nakhjavan, M. N. Tahir, M. Panthoefer, H. Gao, T. D. Schladt, T. Gasi, V. Ksenofontov, R. Branscheid, S. Weber, U. Kolb, L. M. Schreiber, and W. Tremel, J. Mater. Chem. **21**, 6909 (2011).

[109] O. Masala and R. Seshadri, J. Am. Chem. Soc. **127**, 9354 (2005).

[110] F. Wooten, *Optical Properties of Solids* (Academic Press, New York, 1972).

[111] M. Fox, *Optical Properties of Solids* (Oxford University Press, New York, 2010).

[112] K. Huang and R. Q. Han, *Solid State Physics* (in Chinese) (Higher Education Press, China, 1988).

[113] K. W. Lee and W. E. Pickett, Phys. Rev. B **68**, 085308 (2003).

[114] X. Gonze and C. Lee, Phys. Rev. B **55**, 10355 (1997).

[115] Pellets were prepared with very modest pressure, so we do not anticipate that density will approach that of a single crystal as it would if high pressures were employed.

[116] N. R. Jana, Y. Chen, and X. Peng, Chem. Mater. **16**, 3931 (2004).

[117] Y. F. Chen, E. Johnson, X. G. Peng, J. Am. Chem. Soc. **129**, 10937 (2007).

[118] I. Djerdj, D. Aron, Z. Jagliic, and M. Niederberger, J. Phys. Chem. C, **111**, 3614 (2007).

[119] X-ray diffraction experiments yield 4.439 and 4.445 Å for the nanoparticles and bulk, where as neutron diffraction experiments yield 4.44581 and 4.44632 Å. We consider these systems to be isostructural within our sensitivity.

[120] Note that the theoretical calculated density of MnO single crystal is 5.366 g/cm^3, and the actual densities of bulk powder and nanoparticle pellets are ∼3.95 g/cm^3 and 2.54 g/cm^3, respectively. Pellet densities are therefore ∼74% and ∼47% of the single crystal density, respectively, a difference that we correct for in our analysis.

[121] C. C. Homes, M. Reedyk, D. A. Cradles, and T. Timusk, Appl. Opt. **32**, 2976 (1993).

[122] The presence of myristic acid can be verified by the typical spectral signatures near 1300 cm^{-1} (lower right inset, Fig. 5.1(a)), characteristic of organic stretching modes. Thus, the measured nanoparticle reflectance spectrum contains information on both the MnO particles and the capping ligands.

[123] J. M. Machefert, M. Le Calvar, and M. Lenglet, Surf. Inter. Anal. **17**, 137 (1991).

[124] Here, we account for the small portion of the incident light that is reflected by the organic capping layer, the larger part of the incident light that will pass through the capping ligand and be reflected by the MnO, and

the multiple internal reflections and transmissions that subsequently take place.

[125] S. H. Sun and H. Zeng, J. Am. Chem. Soc. **124**, 8204 (2002).

[126] S. H. Sun, Adv. Mater. **18**, 393 (2006).

[127] H. Zeng, J. Li, Z. L. Wang, J. P. Liu, and S. H. Sun, Nano Lett. **4**, 187 (2004).

[128] A. G. Roca, J. F. Marco, M. del Puerto Morales, and C. J. Serna, J. Phys. Chem. C **111**, 18577 (2007).

[129] C. Cannas, et al., Chem. Mater. **22**, 3353 (2010).

[130] K. Maaz, A. Mumtaz, S. K. Hasanain, and A. Ceylan, J. Magn. Magn. Mater. **308**, 289 (2007).

[131] S. Laureti, G. Varvaro, A. M. Testa, D. Fiorani, E. Agostinelli, G. Piccaluga, A. Musinu, A. Ardu, and D. Peddis, Nanotechnology **21**, 315701 (2010).

[132] A. J. Rondinone, A. C. S. Samia, and Z. J. Zhang, J. Phys. Chem. B **103**, 6876 (1999).

[133] J. Garcia-Otero, M. Porto, J. Rivas, and A. Bunde, J. Appl. Phys. **85**, 2287 (1999).

[134] C. N. Chinnasamy, B. Jeyadevan, K. Shinoda, K. Tohji, D. J. Djayaprawira, M. Takahashi, R. J. Joseyphus, and A. Narayanasamy, Appl. Phys. Lett. **83**, 2862 (2003).

[135] C. J. Serna, M. Ocana, J. E. Iglesias, J. Phys. C: Sol. St. Phys. **20**, 473 1987.

[136] $CoFe_2O_4$ bulk powder (99.31%) may still contain small amounts of iron oxide. According to the absorption of Fe_2O_3, [135] there is a strong absorption band at $\sim$330 cm^{-1}, but our spectrum is flat at this range. That means any impurity concentration is very small and the effect of Fe_2O_3 can be ignored in our analysis. Our result is also very similar to Waldron's. [104]

[137] B. Schonfeld, J. J. Huang, and S. C. Moss, Acta Cryst. B **39**, 404 (1983).

[138] J. L. Verble and T. J. Wieting, Phys. Rev. Lett. **25**, 362 (1970).

[139] K. K. Kam and B. A. Parkinson, Journal of Physical Chemistry 86, 463 (1982).

[140] Z. Yin, H. Li, H. Li, L. Jiang, Y. Shi, Y. Sun, G. Lu, Q. Zhang, X. Chen, and H. Zhang, Acs Nano 6, 74 (2012).

[141] H. D. Abruna, G. A. Hope, and A. J. Bard, J. Electrochem. Soc. 129, 2224 (1982).

[142] R. D. Luttrell, S. Brown, J. Cao, J. L. Musfeldt, R. Rosentsveig, and R. Tenne, Phys. Rev. B **73**, 035410 (2006).

[143] Y. Feldman, G. L. Frey, M. Homyonfer, V. Lyakhovitskaya, L. Margulis, H. Cohen, G. Hodes, J. L. Hutchison, and R. Tenne, J. Am. Chem. Soc. **118**, 5362 (1996).

[144] G. L. Frey, S. Elani, M. Homyonfer, Y. Feldman, and R. Tenne, Phys. Rev. B **57**, 6666 (1998).

[145] The recent TEM and X-ray work showed nanoscale metal disulfide (MS_2) are mixed systems, [146] with 2H, 3R, and even 1T polytype inclusions

and domains. But Raman and Infrared spectroscopies indicated there dominated 2H phase in nanoparticles. This is because vibrational spectroscopies are local probe techniques (like TEM in a sense), but they measure an ensemble of particles. Moreover, these spectroscopies are sensitive to the microscopic (local) bonding environment rather than long-range interactions (x-ray). In the nanoscale MS_2, the local bonding environment is very similar in 2H and 3R, even 1T. The diversified results is because of difference length scale for each technique.

[146] A. N. Enyashin, L. Yadgarov, L. Houben, I. Popov, M. Weidenbach, R. Tenne, M. Bar-Sadan and G. Seifert, J. Phys. Chem. C **115**, 24586 (2011).

[147] G. L. Frey, R. Tenne, M. J. Matthews, M. S. Dresselhaus, and G. Dresselhaus, Phys. Rev. B **60**, 2883 (1999).

[148] K. S. Nagapriya, O. Goldbart, I. Kaplan-Ashiri, G. Seifert, R. Tenne, and E. Joselevich, Phys. Rev. Lett. **101**, 195501 (2008).

[149] L. Rapoport, A. Moshkovich, V. Perfilyev, A. Laikhtman, I. Lapsker, L. Yadgarov, R. Rosentsveig, and R. Tenne, Tribol. Lett. **45**, 257 (2012).

[150] R. Rosentsveig, A. Gorodnev, N. Feuerstein, H. Friedman, A. Zak, N. Fleischer, J. Tannous, F. Dassenoy, and R. Tenne, Tribol. Lett. **36**, 175 (2009).

[151] R. Tenne and G. Seifert, Annu. Rev. Mater. Res. **39**, 387 (2009).

[152] O. Tevet, P. Von-Huth, R. Popovitz-Biro, R. Rosentsveig, H. D. Wagner, and R. Tenne, Proceed. Natl. Acad. Sci. USA **108**, 19901 (2011).

[153] L. Yadgarov, R. Rosentsveig, G. Leitus, A. Albu-Yaron, A. Moshkovich, V. Perfilyev, R. Vasic, A. I. Frenkel, A. N. Enyashin, G. Seifert, L. Rapoport, R. Tenne, Angew. Chem. Int. Ed. **51**, 1148 (2012).

[154] R. W. G. Wyckoff, *Crystal structures*, Second edition (Interscience, New York, Vol. 1, 1963).

[155] C. G. Shull, W. A. Strauser, and E. O. Wollan, Phys. Rev. **83**, 333 (1951).

[156] Charges on the O centers are obviously equal and opposite.

[157] E. M. L. Chung, D. McK. Paul, G. Balakrishnan, M. R. Lees, A. Ivanov, and M. Yethiraj, Phys. Rev. B **68**, 140406(R) (2003).

[158] G. F. Dionne, *Magnetic Oxides* (Springer, New York, 2009).

[159] S. J. Kim, S. W. Lee, S. Y. An, and C. S. Kim, J. Magn. Magn. Mater. **215**, 210 (2000).

[160] J. Himmrich and H. D. Lutz, Sol. St. Commun. **79**, 447 (1991).

[161] N. Z. Bao, L. M. Shen, Y. H. A. Wang, J. X. Ma, D. Mazumdar, and A. Gupta, J. Am. Chem. Soc. **131**, 12900 (2009).

[162] C. N. Chinnasamy, M. Senoue, B. Jeyadevan, O. Perales-Perez, K. Shinoda, and K. Tohji, J. Colloid Interface Sci. **263**, 80 (2003).

[163] Q. Chen and Z. J. Zhang, Appl. Phys. Lett. **73**, 3156 (1998).

[164] C. Liu, B. S. Zou, A. J. Rondinone, and J. Zhang, J. Am. Chem. Soc. **122**, 6263 (2000).

[165] B. Szigeti, Proc. R. Soc. Lond., Ser. A, Math. Phys. Eng. Sci. **204**, 51 (1950).

[166] F. Gervais, Sol. St. Commun. **18**, 191 (1976).

[167] M. D. Fontana, G. Metrat, J. L. Servoin, and F. Gervais, J. Phys. C.: Sol. St. Phys. **17**, 483 (1984).

[168] W. Zhong, R.D. King-Smith, and D. Vanderbilt, Phys. Rev. Lett. **72**, 3618 (1994).

[169] R. Tenne and C. N. R. Rao, Phil. Trans. R. Soc. Lond., Ser A, Math. Phys. Eng. Sci. **362**, 2099 (2004).

[170] A.I. Hochbaum, R. Chen, R. Diaz Delgado, W. Liang, E.C. Garnett, M. Najarian, A. Majumdar, and P. D. Yang, Nature **451**, 163 (2008).

[171] A.I. Boukai, Y. Bunimovich, J. Tahir-Kheli, J.-K. Yu, Q.A. Goddard III, and J.R. Heath, Nature **451**, 168 (2008).

[172] For a ferrimagnet, we usually consider a two-sublattice model with spin operators S_{Ai} at the sublattice A site (tetrahedral) and spin operators S_{Bi} at the sublattice B site (octahedral). The Hamiltonian of the system is $H_S = J_{A-A} \sum_{\langle ij \rangle_A} S_{Ai} \cdot S_{Aj} + J_{B-B} \sum_{\langle ij \rangle_B} S_{Bi} \cdot S_{Bj} + J_{A-B} \sum_{\langle ij \rangle} S_{Ai} \cdot S_{Bj}$, [211] where the sum are over all sites of a three-dimensional cubic lattice. $\langle ij \rangle$ denotes the sum over the nearest neighbors, $\langle ij \rangle_A$ denotes the sum over the sites of A sublattice, and $\langle ij \rangle_B$ denotes the sum over the sties of B sublattice. The first two terms describe the ferromagnetic Heisenberg intra-sublattice exchange, with exchange $J_{A-A} > 0$ and $J_{B-B} > 0$. The third term describes the inter-sublattice exchange which is antiferromagnetic ($J_{A-B} < 0$). [211]

[173] H. Martinho, N. O. Moreno, J. A. Sanjuro, C. Rettori, A. J. Garca-Adeva, D. L. Huber, S. B. Oseroff , W. Ratcliff, II, S.-W. Cheong, P. G. Pagliuso, J. L. Sarrao, G. B. Martins, Phys. Rev. B **64**, 024408 (2001).

[174] O. Gunaydin-Sen, C. Lee, L. C. Tung, P. Chen, M. M. Turnbull, C. P. Landee, Y. J. Wang, M. H. Whangbo, and J. L. Musfeldt, Phys. Rev. B **81**, 104307 (2010).

[175] L. I. Vergara, J. Cao1, L.-C. Tung, N. Rogado, F. Yen, Y. Q. Wang, R. J. Cava, B. Lorenz, Y.-J. Wang, and J. L. Musfeldt, Physical Review B **81**, 012403 (2010).

[176] J. Choi, J. L. Musfeldt, Y. J. Wang, G. Dhalenne, and A. Revcolevschi, Sol. St. Commun. **125**, 271 (2003).

[177] R. Zallen, M. L. Slade, and A. T. Ward, Phys. Rev. B **3**, 4257 (1971).

[178] LO-TO splitting is a specific feature of a polar material and represents a measure of coupling with the electric field screened by the electrons.

[179] This indicates a slight surface orientation of the platelets in the pressed pellet samples, as anticipated.

[180] An independent x-ray measurement verified this estimate of orientation.

[181] This assumption is not strictly true. TEM images show that the nanoparticles can have a few "corners", although for practical purposes, neglect of corners and the hierarchy of length scales in these MoS_2 nanoparticles is a reasonable assumption.

[182] The depolarization factor for anisotropic materials was given by Landau. [184]

[183] Based on our assumption that the interlayer polarizability of IF is the same as 2H, $\varepsilon_{A_{2u}}(\infty) = 6.2$ for IF-. Then using Eqn. (4.4c) and fitting

result $\bar{\varepsilon}(\infty) = 5.6$ of IF-, we got $\varepsilon_{E_{1u}}(\infty) = 8.3$, which were shown in Table 5.1.

[184] L. D. Landau, E. M. Lifshitz, and L. P. Pitaevskii, *Electrodynamics of Continuous Media*, 2nd ed (Butterworth-Heinemann, New York, 1984).

[185] R A Cowley, Rep. Prog. Phys. **31**, 123 (1968).

[186] J. E. Eldridge and P. R. Staal, Phys. Rev. B **16**, 4608 (1977).

[187] We employed a constant low frequency extrapolation, as appropriate for a semiconductor. our high frequency extrapolation was done as ω^{-2}.

[188] The error bars of $(\omega_p')^2$, $\varepsilon_1'(\infty)$ are $\pm 6.6 \cdot 10^4$, ± 0.05 for single crystal, and $\pm 3.7 \cdot 10^4$, ± 0.06 for nanoparticles. The error bars of Z_B^*, α, and Z^* are ± 0.07, ± 0.2, ± 0.03 for single crystal, and ± 0.05, ± 0.3, ± 0.015 for nanoparticles.

[189] The depolarization factor $\eta = \frac{1}{3}$ for a cubic system.

[190] B. Masenelli, D. Nicolas, and P. Melinon, Small **4**, 1233 (2008).

[191] The surface-to-volume ratios are 2.4×10^4 and 7.5×10^8 m^{-1} for bulk powder and nanoparticles, respectively.

[192] C. Noguera, J. Phys.: Condens. Matt. **12**, R367 (2000).

[193] There are also several small features centered near 50 cm^{-1} in the reflectance spectrum of single crystalline MnO below T_N, which indicates the coupling between spins and crystal superlattices of MnO.

[194] The relationship between the static dielectric constant $\varepsilon_1(0)$ and the intrinsic effective plasma frequency $\omega_p{}'$ is $(\omega_p')^2 = (\omega_{TO}')^2 \cdot [\varepsilon_1(0) - \varepsilon_1(\infty)]$.

[195] The smaller value of the low temperature local effective charge in the lower branch indicates a reduced ionic interaction in the [111] direction.

[196] In the Lorentz model, the ω_{TO} is only the edge of the Lorentz oscillator, not ω_0.

[197] Below T_N, we took the values of open circles (Figs. 5.3(e) and (f)) for Z^*.

[198] We can estimate the phonon lifetime from the full width at half maximum (Γ) in $\sigma_1(\omega)$ as $\tau = \frac{\hbar}{\Gamma}$. For the nanoparticles, we find $\tau = 2.3 \times 10^{-14}$ sec. This compares with $\tau = 5.9 \times 10^{-13}$ sec for the single crystal. Since a 300 cm^{-1} mode is equivalent to a spectroscopic time scale of $\sim 1 \times 10^{-13}$ sec, infrared spectroscopy is able to resolve the splitting in the single crystal sample, but it captures only an average response for the nanoparticles. This is why the TO phonon does not appear to split for nanoscale MnO.

[199] We anticipate that core-shell effect may influence these values. [204]

[200] The latter is important because the antiferromagnetic portion is the part that engages in spin-phonon coupling. Reduced crystalline anisotropy may also play a role by facilitating spin reorientation in the nanoparticles compared to the bulk.

[201] E. C. Stoner and E. P. Wohlfarth, Phil. Trans. R. Soc. A **240**, 599 (1948).

[202] This expression could also make use of averaged values as in S. H. Sun, C. B. Murray, D. Weller, L. Folks, and A. Moser, Science **287**, 1989 (2000).

[203] S. P. Gubin, *Magnetic Nanoparticles* (Wiley-VCH, Weinheim, 2009).

[204] R. H. Kodama, A. E. Berkowitz, E. J. McNiff and S. Foner, Phys. Rev. Lett. **77**, 394 (1996).

[205] A. Mitsuishi, H. Yoshinaga, and S. Fujita, J. Phys. Soc. Jpn. **13**, 1236 (1958).

[206] No ν_4 absorption band [160] is observed, in line with Waldron's dynamics calculations [104] and the experimental work of Mitsuishi *et al.* [205]

[207] L. D. Tung, V. Kolesnichenko, D. Caruntu, N. H. Chou, C. J. O'Connor, and L. Spinu, J. Appl. Phys. **93**, 7486 (2003).

[208] X. G. Fu, H. Z. An, and W. M. Du, Mater. Lett. **59**, 1484 (2005).

[209] These calculations are based on the rhombohedral primitive unit cell [210] and are identical to results based on the standard unit cell. [160]

[210] There are four Fe cations, two Ni cations, and eight O anions in the primitive unit cell.

[211] N. Karchev, J. Phys.: Condens. Matter **20**, 325219 (2008).

[212] For MnO, the doubly-degenerate branch is in-plane and has no spin-spin correlations, whereas the singly-degenerate component is in the [111] direction and is softened by spin-spin interactions.

[213] Similar effects are observed in other magnetic oxides. [4, 75]

[214] For ν_1, $\omega = 2\pi{\cdot}571$ cm^{-1} $= 1.08 \times 10^{14}$ Hz, and $\omega_0 = 2\pi{\cdot}604$ cm^{-1} $= 1.14 \times 10^{14}$ Hz; For ν_2, $\omega = 2\pi{\cdot}368$ cm^{-1} $= 6.93 \times 10^{13}$ Hz, and $\omega_0 = 2\pi{\cdot}413$ cm^{-1} $= 7.78 \times 10^{13}$ Hz. Then $\omega^2 - \omega_0^2 \approx -1.3 \times 10^{27}$ Hz^2.

[215] $\langle S_i \cdot S_j \rangle$ from inelastic neutron scattering is unfortunately not available, and a full accounting of the interactions in $CoFe_2O_4$ is rather daunting.

[216] J. Mazo-Zuluaga, J. Restrepo, F. Munoz, and J. Mejia-Lopez, J. Appl. Phys. **105**, 123907 (2009).

[217] T. A. S. Ferreira, J. C. Waerenborgh, M. Mendonca, M. R. Nunes, and F. M. Costa, Solid St. Sci. **5**, 383 (2003).

[218] The transition metals do not change their oxidation states as they occupy different sites. [132].

[219] A simultaneous lattice distortion plays an important role in entangling the spin and lattice channels in these materials. MnO undergoes a cubic-to-rhombohedral structural transition at the 118 K Néel temperature (T_N), [4] and $ZnCr_2O_4$ displays a cubic-to-tetragonal structural transition at T_N. [68]

[220] J. Cao, J. Choi, J. L. Musfeldt, S. Lutta, and M. S. Whittingham, Chem. Mater. **16**, 731 (2004).

[221] Usually, we can estimate the phonon lifetime according to the full width at half maximum (Γ) in the dielectric response $\varepsilon_2(\omega)$ as $\tau = \frac{\hbar}{\Gamma}$. [110] However, absorption is not directly related to dielectric constant $\varepsilon_2(\omega)$, so we can not estimate lifetime only according to the absorption $\alpha(\omega)$. But as we know, the nanoparticles usually have much shorter phonon lifetime than the parent compound. [4, 208] As the phonon lifetime is shorter than the spectroscopic time scale of far-infrared ($< 10^{-11}$ s), [222] the spectra only measure the average value for nanoparticles. Phonon lifetime effects thus prevent the observation of phonon splitting in the nanoparticles. In addition, we also need consider the relaxation time (t) in the nanoparticles, $t = t_0 \cdot exp(\frac{KV}{k_B T})$. [164, 207] where t_0 is of the order of $10^{-9} - 10^{-13}$ s, k_B is Boltzmann's constant, T is the temperature, K is the anisotropy constant of the particle, and V is the volume of the particle. As 5 and 7 nm particles are in superparamagnetic state, K can be considered as zero. [163] The

relaxation time will be of the order of t_0, which is probably shorter than the spectroscopic time scale of far-infrared ($< 10^{-11}$ s). [222] The magnetization vector probably changes quickly between different states, but the spins are still bundled in the core of nanoparticles. [204] Spectroscopy experiments reveal average values of the two types of (split) phonons for both mode ν_1 and ν_2, which are different than the bulk.

[222] T. Ito, T. Hamaguchi, H. Nagino, T. Yamaguchi, H. Kido, I. S. Zavarine, T. Richmond, J. Washington, and C. P. Kubiak, J. Am. Chem. Soc. **121**, 4625 (1999).

[223] D. Lin, A. C. Nunes, C. F. Majkrzak, and A. E. Berkowitz, J. Magn. Magn. Mater. **145**, 343 (1995).

[224] D. Peddis, C. Cannas, G. Piccaluga, E. Agostinelli, and D. Fiorani, Nanotechnology **21**, 125705 (2010). .

[225] P. Didukh, J. M. Greneche, A. Slawska-Waniewska, P. C. Fannin, and U. Casas, J. Magn. Magn. Mater. **242**, 613 (2002).

[226] D. Peddis, et al., J. Phys.: Condens. Matter **23**, 426004 (2011).

[227] Error bars are determined by the uncertainties in (i) the peak position and (ii) particle sizes. The larger error bar of the 10 nm particles is related to the broader size distribution.

Vita

Qi Sun was born in Huadian City, Jilin Province, China. He attended Dalian University of Technology in Dalian, where he received B.S. degrees majoring in Polymer Chemical Engineering in June 1999. Then he joined Changchun Institute of Applied Chemistry Chinese Academy of Science in Changhcun, where he received M.S. degrees majoring in Chemistry and Physics of Polymers in June 2005. In August 2007, he enrolled as a graduate student at the Chemistry Department of the University of Tennessee, Knoxville. He joined Dr. Janice Musfeldt's group to begin research in the field of spectroscopic investigations of nanoscale materials. Qi Sun received a Doctor of Philosophy Degree in Chemistry from the University of Tennessee in December 2012.